Intracellular Delivery with Laser-Irradiated Materials

HARVARD UNIVERSITY

Graduate School of Arts and Sciences

DISSERTATION ACCEPTANCE CERTIFICATE

The undersigned, appointed by the

Harvard John A. Paulson School of Engineering and Applied Sciences
have examined a dissertation entitled:

"Intracellular Delivery with Laser-Irradiated Materials"

presented by: Weilu Shen

Signature _____
Typed name: Professor E. Mazur

Signature _____
Typed name: Professor E. Hu

Signature _____
Typed name: Professor S. Mitragotri

Signature _____
Typed name: Professor D. Nelson

March 31, 2022

INTRACELLULAR DELIVERY WITH LASER-IRRADIATED MATERIALS

A dissertation presented

by

WEILU SHEN

to

The John A. Paulson School of Engineering and Applied Sciences

In partial fulfillment of the requirements for the degree of Doctor of Philosophy in the subject of

Applied Physics

Harvard University

Cambridge, Massachusetts

March 2022

Dissertation Advisor: Dr. Eric Mazur Weilu Shen

Intracellular Delivery with Laser-Irradiated Materials

ABSTRACT

Diseases and disorders arise when cells begin to malfunction. To advance basic research in diseases and develop therapeutics, it is vital to understand and fix mechanisms at the cellular level. In the emerging field of nanomedicine, it is important to deliver biologically interesting cargo and molecules directly into relevant cells. Without cargo delivery, therapeutics cannot happen. Alongside medical applications, targeted delivery of cargo, such as probes, and nanodevices for imaging and labeling, is crucial for studying fundamental cell biology. Current established methods each come with respective strengths and weaknesses that fit different application needs. A challenge is the direct delivery into cellular cytoplasm with these key features: viability of the cells, throughput of the cells for therapeutic applications, and efficiency of the tool.

In this thesis, different laser-activated materials for intracellular delivery of large biomolecules in the kDa-range are explored, such as thermoplasmonic gold nanopyramid substrates and particle-embedded PDMS microcuvette chambers. Macromolecules such as siRNA are successfully delivered, and concurrent delivery of multiple cargoes is achieved for human aortic valve interstitial cells *in vitro*. All platforms are excited by 11-ns laser pulses of 1064 nm wavelength to create transient pores in cells that allow materials in the environment to diffuse into the cytoplasm before the phospholipid bilayer membrane seals. Fluorescence imaging and flow cytometry are used to quantify the delivery efficiency and viability in a reproducible manner. Image analysis is used to characterize cell membrane sealing. Scanning electron microscopy,

optical profilometry and hydrophone measurements are used to characterize effects generated by laser-irradiated materials in aqueous medium. The light-activated platforms discussed in this thesis can deliver important material directly into cells, furthering the field of nanomedicine in a cost-effective manner. There has been a lot of development in medicine and biomaterials, but we need to continue exploring methods and tools to get novel molecules into cells so they can reach their full potential for their targeted applications.

Table of Contents

Acknowledgements

"Make everyday a masterpiece." – Coach Everett Crosscup

I've had the incredible pleasure of working with so many amazing collaborators at other institutions and people at Harvard: Marinna Madrid, Daryl Vulis, Marinus Huber, Nabiha Saklayen, Valeria Nuzzo, Stefan Kalies, Alexander Heisterkamp, Alexander Raun, Christine Zgrabik, Nicolas Vogel, Jasmine Sinanan-Singh, Hunter Bigge, Bailey Moers, Youssef Abou El Neaj, William Conway, Choah Kim, Peter Stark, Nicole Black, Anqi Chen, David Weitz, Elena Aikawa, Ikenna Okafor, Taekjip Ha, and many others. I have also benefitted greatly from the staff at CNS, including Arthur McClelland, Sandra Nakasone, and Jason Tresback, and the staff at Bauer Core: Zachary Niziolek, Claire Hartmann, and Jeffery Nelson. I've learned so much from my colleagues in the Mazur Group, and it's been so much fun to work with everyone. SEAS has such wonderful staff and admins who have helped me from day one, like Virginia Casas, Kathryn Hollar, and John Girash.

SEAS is also where I met my fiancé, Alexander Raymond who has been a supportive partner throughout grad school and is also someone I can discuss science with. I feel so lucky to have conversations about research with someone I also share a life with.

My parents, Guangping Wei and Mengyan Shen, and my brother Walter Shen, have also been with me at every step of the way. They've given me every opportunity to succeed without any pressure, and always keep me grounded. It's been a blessing to have my family just a bus ride away, and they always encourage me to chase my dreams.

I have made life-long friends during graduate school and been part of so many great communities at Harvard, such as Dudley House and Adams House. I want to deeply thank former Dudley faculty deans Jim and Doreen Hogle, former Adams faculty deans Sean and Judy Palfrey,

current Adams faculty deans Salmaan Keshavjee and Mercedes Becerra, and current Adams resident dean Charles Lockwood. Professors Chris Rycroft and Rachelle Gaudet have served as my wonderful mentors for Harvard Graduate Women in Science and Engineering (HGWISE). Professor Peter Persans, my undergraduate advisor at Rensselaer Polytechnic Institute, also provided invaluable guidance. Although these professors were not part of my research, their devotion to my well-being and professional development has been paramount to my experience.

I want to also express gratitude to my committee members. I am so grateful for their guidance and wisdom. Professors Samir Mitragotri and David Nelson have always made time for me when I had questions about research direction and professional development advice. The constant encouragement I have received from Professor Evelyn Hu has been so valuable, and words cannot describe how much her support has meant to me. I am so lucky to have these caring professors watch over me during grad school. I hope that someday, I can have the same impact on a group of scholars as they all have.

Finally, I want to thank my advisor, Professor Eric Mazur. I was a high school intern in his lab in the summer of 2011 and his lab is where I fell in love with science. The opportunity he gave a kid like me is the reason why I am doing the work I am most passionate about. I had incredible mentors in the lab, like Paul Peng, SeungYeon Sally Kang, Meng-ju Renee Sher, Yu-Ting Lin, Kelly Miller, and many others, who not only guided me in research but also gave me the confidence to pursue science as a career. Eric has also cultivated an incredible research group and has provided to us all a research family that I am honored to be part of. He is generous with his time and attention, is constantly supportive and gives me the space to explore, and always has the big picture in mind. I've learned so many things from Eric outside of the lab too, and he is a model of open-mindedness and kindness. He is the best advisor I could ever have asked for.

I would like to acknowledge financial support: The research described in this thesis was supported by National Science Foundation under contracts PHY-1219334, PHY-1205465, and PHY-1806434. This work was performed in part at the Harvard University Center for Nanoscale Systems (CNS), a member of the National Nanotechnology Coordinated Infrastructure Network (NNCI), which is supported by the National Science Foundation under NSF award numbers ECCS-1541959 and ECCS-2025158. The Harvard MRSEC (DMR-1420570) was also used. I was also funded by the Smith Family Graduate Science and Engineering Fellowship at Harvard University, and the American Dissertation Fellowship from American Association of University Women.

I would like to acknowledge Henrietta Lacks, an African American woman whose cervical cancer cells were taken without her knowledge or consent in 1951. Her cells are the oldest and most commonly used immortalized human cell line. The work done in this thesis uses HeLa cells. I am grateful to Henrietta Lacks, now deceased, and her family members for their contributions to biology and medicine. [1]

For my amazing parents, Mengyan Shen and Guangping Wei.

Chapter 1

Introduction

1.1 Dissertation Scope

Light amplification by stimulated emission of radiation, or laser, is a term that was coined by Charles Townes in 1951.[2] A pulsed-laser, in the case of the nanosecond pulsed laser-irradiation for cargo delivery discussed in this thesis, is in reference to lasers that do not operate as continuous wave, but the optical power appears in pulses in a specific duration of time at a specific repetition rate. There is a wide application of lasers from material processing to precise measurements, but one of the most impactful application of lasers and optics is in the fields of biology and medicine.[3,4] Laser have been introduced into clinical use in many ways, allowing for more precise and less invasive procedures in surgery. Lasers have also been used in a wide range of imaging techniques such as endoscopic laser surgery, high-resolution microscopy, and subcellular nanosurgery.[5] While there are a wide range of laser-tissue and laser-cell interactions that are of incredible importance, in this thesis we use a near-infrared laser wavelength that do not interfere with biological processes.[6] We employ laser-matter interactions in aqueous environments to produce transient pores in cell membranes for the purposes of intracellular cargo delivery. Universal delivery of diverse cargo is a key step in the development of therapeutics and furthering our understanding of cell biology, and lasers play a pivotal role in developing methods for disrupting the cell membrane for cargo delivery.

1.2 Dissertation Organization

The focus of this thesis is on the application of a broad range of materials for intracellular cargo delivery that is initiated by nanosecond pulsed-laser irradiation. We perturb the cell

membrane to create pores that are large enough that cargo can diffuse into the cytoplasm but small enough that the cell is able to heal the pore and survive the disruption. Many laser-irradiated nanoparticle applications in biomedicine have the motivation of targeted cell ablation, such as for tumor debulking, but in the case of cargo delivery there is a fine balance of controlling the cells to be vulnerable for a short period of time during delivery treatment.

The following second chapter of this thesis covers some fundamental concepts in the diverse field of intracellular cargo delivery. Established methods for delivery, such as electroporation and optoporation, are discussed. Laser-material interaction in the context of thermoplasmonic effects of pulsed laser-irradiated gold nanoparticles are also covered due to its relevance to the first material that introduced in the following chapter.

The third chapter of this thesis introduces three different kinds of thermoplasmonic nanostructures: gold continuous film nanopyramid array substrates, titanium nitride pyramid array substrates, and titanium nanocavity (also known as inverse opal) array substrates. All three require fabrication of thin-film metal deposition but the titanium nanocavity substrates do not require cleanroom techniques to be made and employs colloidal self-assemblies to create the array.

The fourth chapter of this thesis shows proof-of-concept cargo-delivery with off-the-shelf polyvinyl substrates. The substrate does not require any kind of fabrication, have no specific nanostructure patterning that drive cargo delivery, and do not require thin-film metal. laser-polyvinyl interactions are probed by measuring pressure waves that are generated in water upon laser-irradiation and the quantitative analysis is applied to understanding the correlation of magnitude of impulse a cell experiences to cargo delivery rates and cell survival viability rates.

The fifth and penultimate chapter covers work that uses the proof-of-concept experiments in the prior chapter to develop an optimized polymer material that is low-cost to fabricate and can

be applied to both adherent and suspension cells. A common polymer, polydimethylsiloxane, is embedded with carbon black particles that interacts with the nanosecond pulsed laser to drive cargo delivery. Spatially and temporally selective multiple-cargo delivery is demonstrated with model fluorescent particles and open the door to *in vitro* experiments that may be of interest to developmental cell biologists. The particle embedded PDMS is also incorporated in soft lithography fabrication techniques to produce microcuvette chambers to deliver siRNA to suspension cells.

Finally, the last chapter will cover the conclusion of this thesis and discuss future outlooks and experiments that can further the field of intracellular cargo delivery and better understand laser-matter interactions for biomedical applications.

Chapter 2

Fundamental Concepts

2.1 Motivation and Scope

Biology and nanomedicine are on the verge of a major disruption by the recent discovery and synthesis of new drugs, new genetic materials, and new biomedical cargoes.[7–13] A major barrier to advancing these molecular cargoes, however, is intracellular delivery of these payloads into the cellular cytoplasm. [14] Current delivery techniques hold significant drawbacks: viral-mediated gene transfers, while efficient, are cell-specific, integrate irreversibly into a host's genome, and can instigate the host's immune response [15]. Non-viral vectors such as chemical and physical methods are safer; however, the cellular and nuclear barriers for efficient DNA delivery remain a challenge [16,17]. Lipid-based DNA-complexing agents can be tailored to overcome these barriers, but currently result in moderate efficiencies with the need for series of reagents for cell line-specific protocols [18,19]. Electroporation allows direct entry of the gene into the cell. However, there the limitation of *in vivo* electroporation methods is the accessibility of the electrodes to the internal organs and potential tissue damage [15,20]. Optoporation employs the use of femtosecond lasers to porate cells for efficient and non-toxic delivery, but the process is slow as each cell must be laser-targeted and porated individually.

In this thesis, the work developed and studied an *in vitro* platform for cargo delivery using metallic thermoplasmonic nanostructures on a substrate that offers high delivery efficiency, viability, and throughput for a range of cell types and cargo sizes [21–24] are covered. Work using polymer materials in both substrate and microcuvette form are also covered. However, a significant need in bio- and nano-medicine is the lack of *in vivo* transfection materials that are simple and easy to integrate into complex systems in a clinical environment. The work done for cell membrane

disruption for intracellular delivery, from applications to understanding the physical effects and cellular reactions, have been extensive and this section only covers a brief range of techniques, their advantages and disadvantages, that may be helpful for understanding the context of the following chapters and new experimental results.

2.2 Cargo Delivery

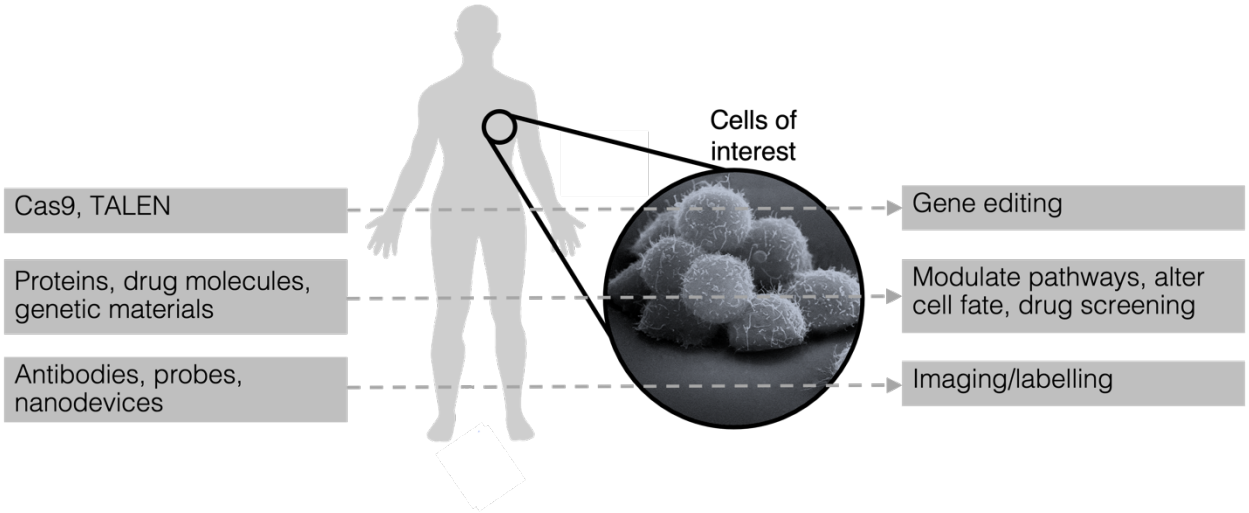

Figure 2.1: Motivation schematic. Diseases and disorders arise when cells begin to malfunction in some way. In order to advance basic research and develop therapeutics, it is vital to understand and manipulate mechanisms at the cellular level. To change the characteristics of cells, we must be able to manipulate biological functions with the delivery of molecules such as proteins, antibodies, and genetic materials. However, the challenge in the biomedical field is the direct delivery of such payloads into the cell.

The ability to delivery large biomolecules and nanoparticle cargoes requires the fine balance between creating a pore or multiple pores that are large enough to allow the cargo to enter the cytoplasm but also small enough to reseal and survive. Proteins can be delivered into the

cytosol to manipulate the expressed traits of cells. Genetic materials such as small interfering RNA (siRNA) can be delivered to manipulate gene expression. With the development of CRISPR-cas9, gene-editing can be used for gene-therapy treatments. Some smaller cargoes such as siRNA are around 10 nm, but the sizes of cargoes of interest for intracellular delivery can go up. For example, antibodies and GFP are twice as big, and mRNA can be 100 nm. When naked plasmid DNA are considered, they can be hundreds of nm large and microparticles and beans can be in the micron-range. Cargoes of interest are also variable in shape, architecture, and chemical properties that can affect electrostatic charge. Some cargoes are also sensitive to their environment. For example, RNA can be very sensitive to ribonuclease (RNase), which is a type of nuclease that degrades RNA into smaller components. Each kind of cargo has respective challenges in entering the cytoplasm and sensitive cell lines such as stem cells and other patient primary cells can also be incredibly difficult to perturb while maintaining viability. Specifically, hematopoietic cells and neurons have been difficult to transfect. Immunotherapy applications and studies also require the targeted delivery to cell types such as T cells, but they are also difficult to transfect.[25,26]

Some cargoes have specific locations they must be to work. While therapeutics such as mRNA or siRNA can function in the cytosol, DNA therapeutics must reach the nucleus and requires the crossing of the nuclear membrane which is double lipid layered. Some cells are also very difficult to deliver to, specifically primary cells directly taken from a patient. While robust cell lines, such as HeLa cells, are often easier to handle and not as precious due to their abundance in a lab, primary cell treatments need high viability. The plasma membrane is also a complex and dynamic phospholipid bilayer and is comprised of a diverse range of proteins such as transporters, receptors, and enzymes. This complexity that causes the cell membrane to have localized lipid asymmetry must also be considered when developing delivery methods, particularly with chemical

methods.[27] It is thus important to explore methods to deliver difficult to deliver cargo to specific regions of sensitive cell lines.

2.3 Established Methods for Delivery

There is a diverse range of delivery approaches for a wide range of cargoes. In this section, some popular methods that are commonly used and have established methodology are discussed.

Electroporation allows direct entry of the gene into the cell and is a popular method in many wet-bench biology labs. [28] There are still new discoveries being made about the physical and biochemical effects electroporation pose on the cell membrane, often through molecular dynamics modelling, and the effects must be better understood for furthering clinical applications. [29,30] However, there the limitation of *in vivo* electroporation methods is the accessibility of the electrodes to the internal organs and potential tissue damage. Also, small holes created by electroporation can persist for long durations and drain the cell of resources, sometimes posting cytotoxicity.[31] However, the addition of buffers for promoting cell membrane integrity after delivery can improve viability rates in electroporation.[32]

Viral-mediated gene transfers, while efficient, are cell-specific, integrate irreversibly into a host's genome, and can instigate the host's immune response. The cargo-type is also limited to genetic materials only and there is limited space in the viral envelope. There is also risk of insertional genotoxicity and the technique can be labor-intensive.

Lipofection is a non-viral technique that is still carrier mediated. The lipid capsule carriers are endocytosed into the cell with cargo, such as nucleic acid, breaking out into the cytoplasm. The cationic lipids and polymers can pack and condense cargo that are otherwise large, such as plasmids, down to the order of tens of nanometers to deliver larger molecules more easily.[33] The cationic positively charged particles can also improve interactions with the negatively charged cell

surface, which is typically negative 35 to 80 mV. There are studies that show that the positive charge of these lipids can also promote binding to specific cell membrane receptors. [34] The liquids can also act as protection to prevent degradation of nucleic acids in the cytoplasm. However, there may be some disadvantages due to complications in delayed capsule unpacking and toxicity. [35,36] Lipid-based DNA-complexing agents can be tailored to overcome these barriers but can result in moderate efficiencies with the need for a series of reagents for cell line-specific protocols.

Cell membrane disruption for cargo delivery can also be induced by sonoporation when cells are exposed to acoustic pressure waves. [37,38] The waves are often in the ultrasound frequency range and high-intensity focused ultrasound can be used for tissue drug delivery as well, such as for transdermal applications.[39] Oscillating cavitation bubbles and pressure differences in the medium drive membrane disruption. [40–42] The phenomena of sonoluminescence can also drive temperature changes to perturb the cell membrane through fluid shear forces.[26] However, sonoporation may be more appropriate for larger scale tissue bulk delivery for therapeutic applications rather than for cellular *in vitro* applications due to low efficiency and viability. [43,44] Laser-ablation can also produce acoustic cavitation and shock waves in liquid, which has been applied to cargo delivery by inducing mechanical stresses in the cell membrane. Shock waves through laser excitation is comparable to the shock waves produced by shock tubes in order to deliver cargo to cells. [45,46]

Cell squeezing microfluidic and lab-on-chip platforms for cell membrane perturbation can provide controlled delivery by forcing cell deformation by squeezing cells through thin microchannels for a short period of time. [47–49] The membrane becomes deformed and temporarily disrupted, allowing for the diffusion of cargo. The dimensions of the channels vary but are generally in the range of 4 to 8 μm, which is about half the diameter of a cell. [50] The method is

high throughput but requires design changes for different cell types. Electroporation has also been applied to cell squeezing platforms. [51] However, there are some off-target effects due to cell squeezing such as damaging the cytoskeleton, nucleus, and can also cause DNA damage due to nuclear ruptures. [52] Cell survival can also be affected by the squeezing effects. In chapter 5 of this thesis, microcuvette chambers are used to force the cells to be in contact with laser-activated materials for cargo delivery and the cells are thus slightly squeezed, but the chamber dimension is 10 μm for cells of 12 μm diameter – a much smaller height-to-cell ratio than the aspect ratio used in cell squeezing.

It should also be mentioned that the method of microinjection has an extensive history in ground-breaking studies in biology and *in vitro* fertilization, but similarly has lower throughput and cannot be used for large-scale experiments and applications. [53] Nanostraws and nanowires have also been used to deliver to cells but can prevent stable cell growth and cause cells to have disrupted proliferation features. [54,55]

2.4 Laser-induced delivery

Optoporation employs the use of a tightly focused femtosecond laser beam to porate cells for efficient and non-toxic delivery, but the process is slow as each cell must be laser-targeted and porated individually. [56–58] Optimized tipless gold pyramids that harness near-field enhancement for large-scale optoptoporation has been developed but require extensive nanofabrication techniques and require an expensive femotosecond laser platform. [21,24] Plasmonic and thermoplasmonic nanoparticles have been used extensively for intracellular delivery. [59] Highly wavelength-absorbing particles, such as carbon black, have also been used in suspension with cells. [60] Plasmonic structures have also been used extensively in tagging and detection due to their ability to generate highly localized electric fields through plasma oscillations.[61,62] However, unlike

the gold pyramid substrate platform that will be discussed in the next chapter in this thesis, these particles can remain and aggregate inside cells after delivery and there is still extensive research into the potential long-term cytotoxicity of the presence of these gold nanoparticles – especially if the particles fragment inside the cytoplasm after laser irradiation. [63–65] Nanosecond-laser irradiated surfaces that incorporate gold and induce cargo flow into cells have also been investigated in the past, but the platform can require expensive nanofabrication that lowers the barrier of entry for applications. [66]

2.5 Conclusion

The field of intracellular delivery utilizes a range of interdisciplinary methods for getting interesting molecules past the cell membrane and into the cytoplasm. An extensive amount of research has been conducted in understanding the physical, chemical, and viral techniques and their effects on the complicated structures of the cell membrane. The development of new microfluidic methods and nanotechnology provides the controlled intracellular cytoplasmic cargo delivery field new grounds to play on for high throughput systems that can be applicable to more diverse and more sensitive cell lines. As nanomedicine continues to push the boundary for new drug discovery, cargo delivery methods must keep pace to accelerate the impact of clinical applications and to better understand fundamental cell biology.

In this thesis, many of the concepts of the existing cargo delivery methods are applied. For example, with the gold thermoplasmonic pyramids, much of the understanding of nanosecond pulsed laser irradiation of gold nanoparticles and cavitation bubbles are applied to create particulate-free continuous-film gold nanostructures for spatially localized cargo delivery to adherent cells. Cell membrane pore dynamics from femtosecond optoporation have been applied to understand the permeability of the gold pyramid-induced membrane disruption. Much of the

understanding of pressure waves generated by laser-ablation of carbon black is applied to cargo delivery with black polyvinyl substrates and carbon black-embedded PDMS substrates.

Chapter 3

Thermoplasmonic Metal Structures

This chapter has been adapted from the following publications:

Saklayen, N.; Huber, M.; Madrid, M.; Nuzzo, V.; Vulis, D. I.; Shen, W.; Nelson, J.; McClelland, A. A.; Heisterkamp, A.; Mazur, E. Intracellular Delivery Using Nanosecond-Laser Excitation of Large-Area Plasmonic Substrate. *ACS Nano* **2017**, *11* (4), 3671–3680. https://doi.org/10.1021/acsnano.6b08162. [22]

Saklayen, N.; Kalies, S.; Madrid, M.; Nuzzo, V.; Huber, M.; Shen, W.; Sinanan-Singh, J.; Heinemann, D.; Heisterkamp, A.; Mazur, E. Analysis of Poration-Induced Changes in Cells from Laser-Activated Plasmonic Substrates. *Biomed. Opt. Express* **2017**, *8* (10), 437–444. https://doi.org/10.1364/BOE.8.004756. [23]

Madrid, M.; Saklayen, N.; Shen, W.; Huber, M.; Vogel, N.; Mazur, E. Laser-Activated Self-Assembled Thermoplasmonic Nanocavity Substrates for Intracellular Delivery. *ACS Appl. Bio Mater.* **2018**, *1* (6), 1793–1799. https://doi.org/10.1021/acsabm.8b00447. [67]

Raun, A.; Saklayen, N.; Zgrabik, C.; Shen, W.; Madrid, M.; Huber, M.; Hu, E.; Mazur, E. A Comparison of Inverted and Upright Laser-Activated Titanium Nitride Micropyramids for Intracellular Delivery. *Sci. Rep.* **2018**, *8* (1),15595.https://doi.org/10.1038/s41598-018-33885-y. [68]

3.1 Introduction

Efficiently delivering functional cargo to millions of cells on the time scale of minutes will revolutionize gene therapy, drug discovery, and high-throughput screening. Recent studies of intracellular delivery with thermoplasmonic structured surfaces show promising results but in most cases require time- or cost-intensive fabrication or lead to unreproducible surfaces.[66,69]

This chapter also presents two types of laser-based cargo delivery platforms which utilize thermoplasmonic effects: (1) micropyramid arrayed substrates created with a cost-effective method of large-area photolithography and template-stripping, a plasmonically optimized device which efficiently delivers cargoes ranging in size from 0.6 to 2000 kDa to cells with high viability (of up to 98%). The technique is also high throughput, treating 50,000 cells per minute by raster-scanning the laser as shown in Figure 1. Thermoplasmonic nanostructures have the potential to become excellent tools for biomedical applications. Laser-activated thermoplasmonic gold nanoparticles form heat-mediated bubbles to make transient pores in cells for intracellular delivery.[62,63,70,71] Despite being effective intracellular delivery agents, the long-term cytotoxicity of gold nanoparticles still remains under debate.[63–65] Recent studies of intracellular delivery with thermoplasmonic structured surfaces are encouraging as they do not utilize gold nanoparticles in solution but in some cases require time- or cost-intensive fabrication; in some instances, each substrate is fabricated using lithography methods, making it difficult to scale up to applications that require many large-area samples.[72] Lithography can provide controlled small-resolution fabrication with consistent sample fabrication. Some substrate-based studies with gold nanoparticle layers are more easily fabricated but can be nonreproducible in nature and leave metal fragments behind after the experiment. There were minimal residual fragments after laser-irradiation of gold pyramids, unlike other plasmonic delivery methods using gold nanoparticles. The pore sealing dynamics of gold pyramids irradiated by a picosecond laser is also covered in this chapter. Additionally, silicon pyramid structures without the gold can also be used to make titanium nitride surfaces that also exhibit thermoplasmonic effects for cell poration.

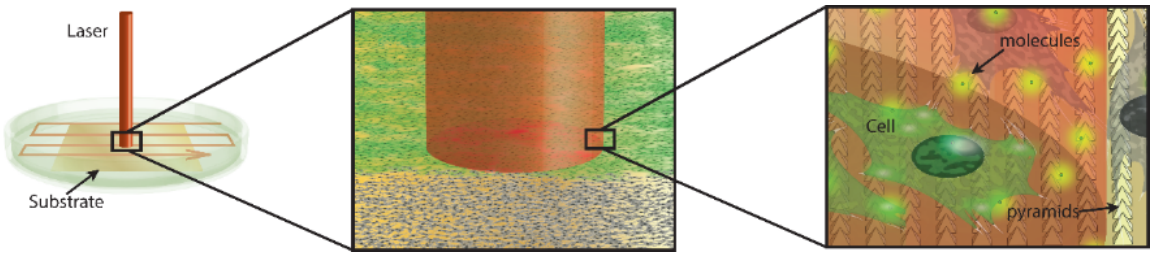

Figure 3.2: *Nanosecond laser-excitation of large-area plasmonic substrates for intracellular delivery technique. A nanosecond laser is scanned across the sample for high-throughput delivery to a million cells cultured on the substrate. The laser spot illuminates thousands of simultaneously. Laser illumination causes thermoplasmonic nano-heating at the apex of each pyramid. The heating forms bubbles that create temporary pores in cells at close contact. The pores enable fluorescent cargo in the surrounding solution to diffuse directly into the cytosol.*

(2) Dense arrays of colloidal self-assembled nanocavities were thermally coated with 50 nm of titanium to create large macroscopic areas that can efficiently convert near-infrared laser light into heat. The substrate array geometry facilitates successful optoporation and cargo delivery. An alternative to nanofabrication is the design of nanostructures from the bottom-up through self-assembly processes to direct suitable building blocks into ordered arrangements of periodic surface structures over macroscopic areas. Colloidal self-assembly employs spherical colloidal particles which can be conveniently synthesized at nanoscale dimensions using scalable synthesis protocols as building blocks to create well-ordered arrangements in two and three dimensions. [73,74] These colloidal crystals can serve as templates to create nanoporous materials: A second material, typically sol–gel derived silica, is deposited within the interstitial sites of the polymer colloidal crystal to create a porous layer after removal of the templating colloidal particles. [75,76] Note that, while the term nanopores in some communities is exclusively used for pore dimensions much below 100 nm, porous materials prepared by colloidal templating are also typically referred to as

nanopores, even though the dimensions are typically in the range of 100–1000 nm. Alternatively, a directed metal deposition step can produce defined metal nanostructure arrays by exploiting the shadowing effect of the colloidal particles on the surface. Colloidal self-assembly therefore provides a platform to create defined, functional nanostructure arrays in a simple, fast, and scalable fashion. [77–79] This colloidal substrate does not require cleanroom fabrication facilities that the gold nanopyramids do and is able to deliver the membrane-impermeable calcein green dye molecules into the cellular cytoplasm at an efficiency of 78% and at a throughput rate of 30,000 cells per minute by raster scanning as shown in Figure 3.2. 87% of the cells survive treatment.

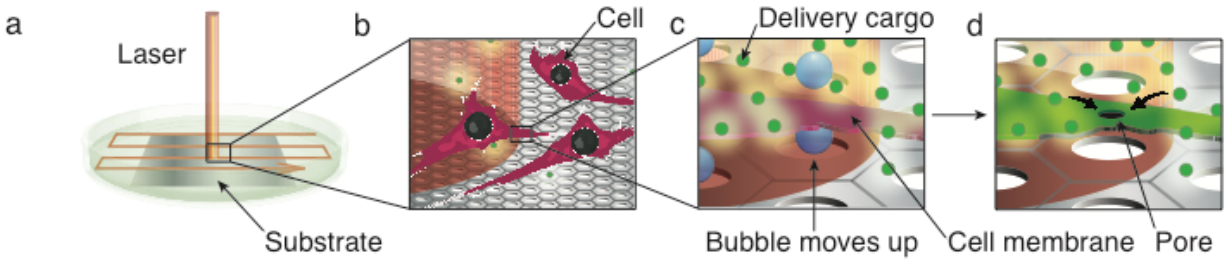

Figure 3.3: *Intracellular delivery using a self-assembled laser-activated thermoplasmonic nanocavity substrate. (a) A self-assembled thermoplasmonic nanocavity substrate is placed at the bottom of a petri dish. HeLa CCL-2 cells are cultured onto the substrate and the laser beam is scanned across the sample. (b) The laser beam spot illuminates specific regions of the self-assembled thermoplasmonic substrate, enabling spatially selective intracellular delivery to the cells cultured in those regions. (c) The laser light energy is absorbed by the metallic nanostructures, resulting in localized heating and the formation of bubbles in the surrounding cell medium. (d) The bubbles form transient pores in the cell membrane, permitting membrane-impermeable target molecules in the surrounding cell medium to diffuse into the cell through the pores. After the pores heal, the target molecules are enclosed in the cell, concluding the light-activated intracellular delivery.*

The substrate platforms (gold pyramids, titanium nitride pyramids, and titanium nanocavities) are all excited by 11-ns laser pulses of 1064 nm wavelength to create transient pores in cells with a set-up as shown in Figure 3.3. Adherent cell lines such as HeLa are grown on the substrates, and pores only form on the cells in the localized regions excited with nanosecond laser pulses—thus, allowing treatment selectivity within a population. The medium surrounding the cell contains the delivery cargo in solution, and cargoes diffuse into the cell before the transient pores are sealed. We use fluorescence imaging and flow cytometry to quantify the delivery efficiency and viability in a reproducible manner. Our light-activated substrate platforms can deliver important material directly into cells, furthering the field of nanomedicine in a cost-effective manner. The approach we present offers additional desirable features: spatial selectivity, reproducibility, minimal residual fragments, and cost- effective fabrication. This research supports the development of safer genetic and viral disease therapies as well as research tools for fundamental biological research that rely on effectively delivering molecules to millions of living cells.

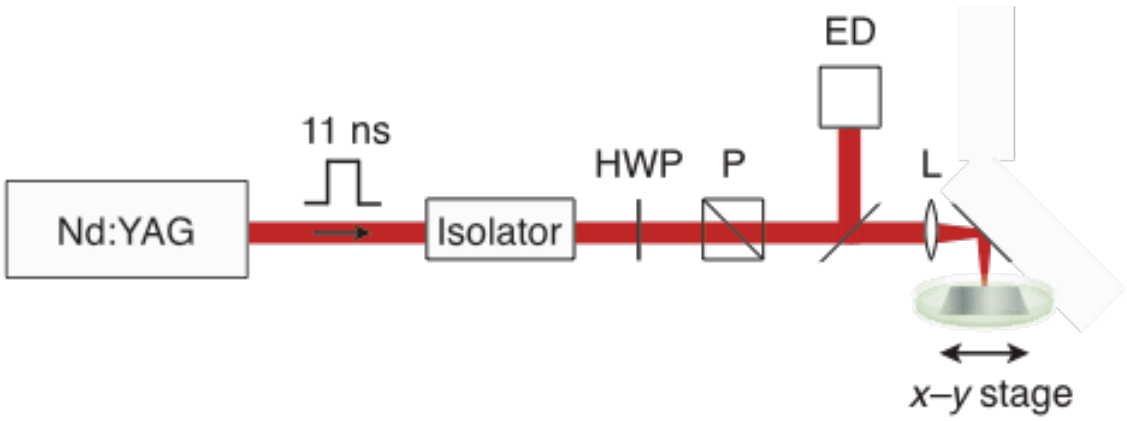

Figure 3.4: *Nanosecond-pulsed laser setup. The setup uses a 1064-nm wavelength 11-ns pulsed Nd:YAG (neodymium-doped yttrium aluminium garnet) laser with a repetition rate of 50 Hz. The laser beam has a top hat profile and passes through an isolator to prevent back reflections. A half-*

wave plate and polarizing beam splitter is used to control the energy output. A pellicle beam splitter directs a fraction of the laser energy to an energy detector to measure the energy output during experiments. A lens loosely focuses the beam spot to a diameter of approximately 1.1 mm at the sample. The sample sits on an x-y translational stage that enables scanning of the laser beam across the substrate.

3.2 Micropyramids

3.2.1 Fabrication of pyramids

Template stripping is a high-throughput and reproducible approach to producing plasmonic structures in the form of metallic films that are ultrasmooth and precisely patterned over large areas. This fabrication method is highly advantageous as lithography needs to be performed once to fabricate templates in silicon that can be repeatedly used to generate template-stripped metallic substrates in a few steps. [80–83]

To prepare the silicon wafers, they are first sonicated in acetone for 5 minutes and methanol for 5 minutes and rinsed in isopropyl alcohol. Then the wafer is oxygen plasma treated at 100 W at 20 mT for 1 minute. Then, as step 1 of the schematic in Figure 3.4 shows, a 15 nm layer of chromium is thermally deposited to act as a hard mask for lithography and then baked at 200 °C for 3 minutes to evaporate any residual solvent. SPR 700-1 photoresist was spin coated onto the wafer at 3000 rpm for 45 seconds and soft baked at 115 °C for 1 minute. Then, the wafer is exposed in an autostepper to form a square grid array and then post-exposure baked at 115 °C for 1 minute. The wafer is developed in CD-26 developer for 1 minute and then rinsed with DI water for 20 seconds, repeating until the photoresist no longer released residue in the developer to produce the form in step 3 of Figure 3.5. The wafer was descummed in a plasma stripper for 15 seconds and

then the exposed chromium layer was removed with chromium etch to expose the silicon underneath, as seen in step 4. The wafer is washed in deionized water and dried with nitrogen air before washed in acetone and oxygen plasma treated to remove the photoresist. In order to achieve the inverse silicon wafer as shown in step 5, potassium hydroxide (KOH) etch was performed to etch the <100> plane at a 54.7° angle relative to the <111> plane. The anisotropic etching is possible because the activation energy of the silicon atoms (FCC crystal structure) in the <100> plane is lower than those in the <111> plane. [84] First, 4.5% hydrogen fluoride is used to remove silicon oxide from the wafer and a KOH etch of 2:1 water to 45% KOH was heated at 80 °C and the wafer is submerged for 3 minutes to form the inverse structures. Again, a chromium etch is performed to remove the last part of the hard chromium mask to expose the complete silicon inverse pyramid structures as illustrated in step 6.

To create template-stripped gold pyramids, electron-beam evaporation is used to deposit a 50 nm layer of gold as shown in step 7. Then, the gold is back-filled with UV-curable glue (Norland Adhesive 61) and covered with a No. 1.5 coverslip before being cured under a UV lamp overnight to form step 8. As step 9 shows, a razor blade is used to “strip” the gold-glue-glass structure off the silicon template to form the final structure in step 10. Figure 3.6 shows the spectrophotometer measurement of the gold pyramids.

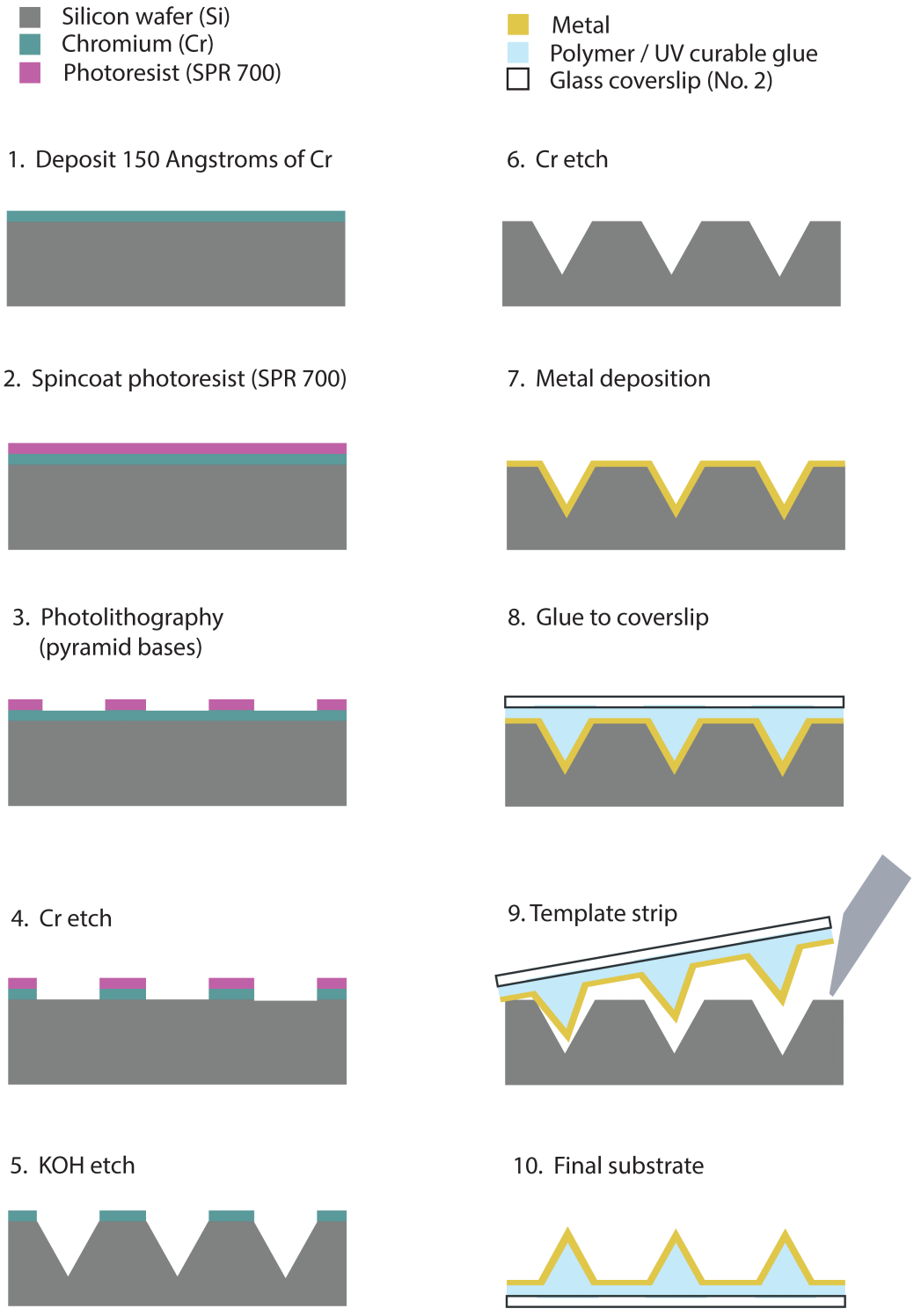

Figure 3.5: *Fabrication steps for template-stripped thermoplasmonic substrates. Steps 1 to 6 describe the silicon wafer master template fabrication and steps 7 to 10 describe the template stripping process to produce the thin continuous film gold pyramids. The master templates can be*

reused hundreds of times for template stripping. This intracellular delivery technique is easily scalable as photolithography can be extended to make larger samples, and the scanning speed and/ or beam spot size can be increased with additional optical components.

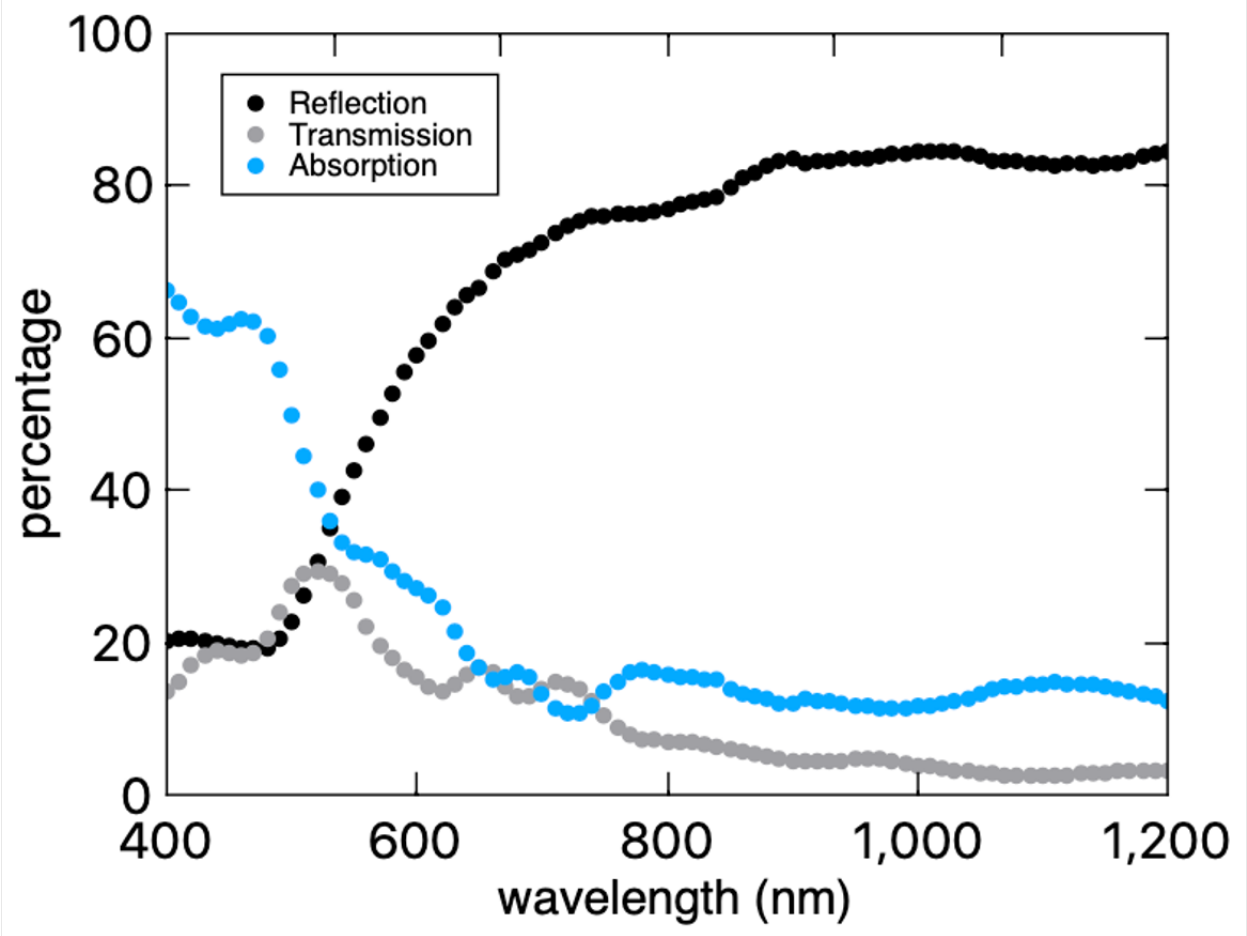

Figure 3.6: *Absorption, reflection and transmission spectra of plasmonic substrates illuminated from above. The thin-film 50 nm gold pyramids measured have uniform base lengths of 2.4 µm, 1.4 µm in height, and 1.2 µm in array spacings.*

Titanium nitride (TiN) can also be deposited on the gold covered pyramids or directly onto the silicon master template to create inverse pyramids. Titanium nitride is a promising plasmonic

material due to its high hardness and thermal stability compared to the gold pyramids which are made of a weak metal mechanically with a lower scratch resistant (2.5 out of 10 on the Mohs hardness scale) which may be difficult to integrate for long-term clinical applications. TiN, on the other hand, is an extremely robust material that is often used in industrial applications for strong protective coatings and has a Mohs hardness scale rating of 9 with a melting temperature of 2947 °C, more than twice as high as gold's melting temperature of 1064 °C. [85–87] TiN has non-stoichiometric composition and also has unique plasmonic characteristics due to its tunable electronic properties that can be done by changing different fabrication parameters: substrate type, temperature during deposition, and whether the deposition is done using reactive or non-reactive sputtering. TiN is a biocompatible material that can generate localized hotspots similarly to the gold pyramids. [88–90]

Two different structures of TiN thin film are made, as shown in Figure 3.6. The 50 nm of TiN is sputtered onto both the inverted silicon pyramids and upright gold pyramids by using DCV magenetro sputtering. The TiN target plasma is ignited at a pressure of 25 mT. After the ignition, the target power is ramped up to the maximum value of 50% of the total power, which corresponds to 150 W and 393 V. This ramp up is done at a pressure of 4 mT. After ramping up, an 8-W, 90-V bias is applied to the substrate. Immediately after, the shutter over the TiN target is opened, allowing the sputtering process to begin. Because this process takes place at room temperature, the 90-V substrate bias is necessary in order to ensure a metallic TiN layer is sputtered. [91] Figure 3.7 shows the spectrophotometer measurement of the titanium nitride inverse pyramids and upright pyramids.

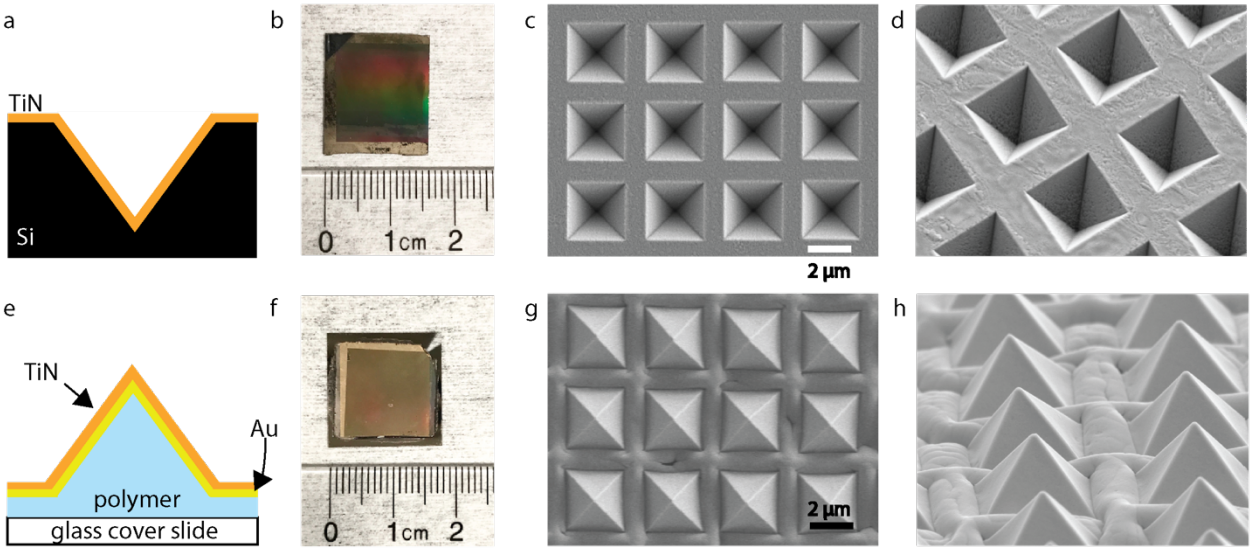

Figure 3.7: *Inverted and upright TiN micropyramids. (a) A schematic of the cross section of the inverted pyramid design. (b) The inverted pyramid substrate next to a ruler. (c) Top-down view of the inverted pyramids with SEM. (d) Tilted SEM of the inverted pyramids, showing consistent fabrication dimensions for each structure. (e) A schematic of the cross section of the upright pyramid design. (f) The upright pyramid substrate next to a ruler. (g) Top-down view of the upright pyramid design taken via SEM. (h) Tilted view of the inverted pyramid design taken via SEM. This shows a consistent rising of the film in between each pyramid.*

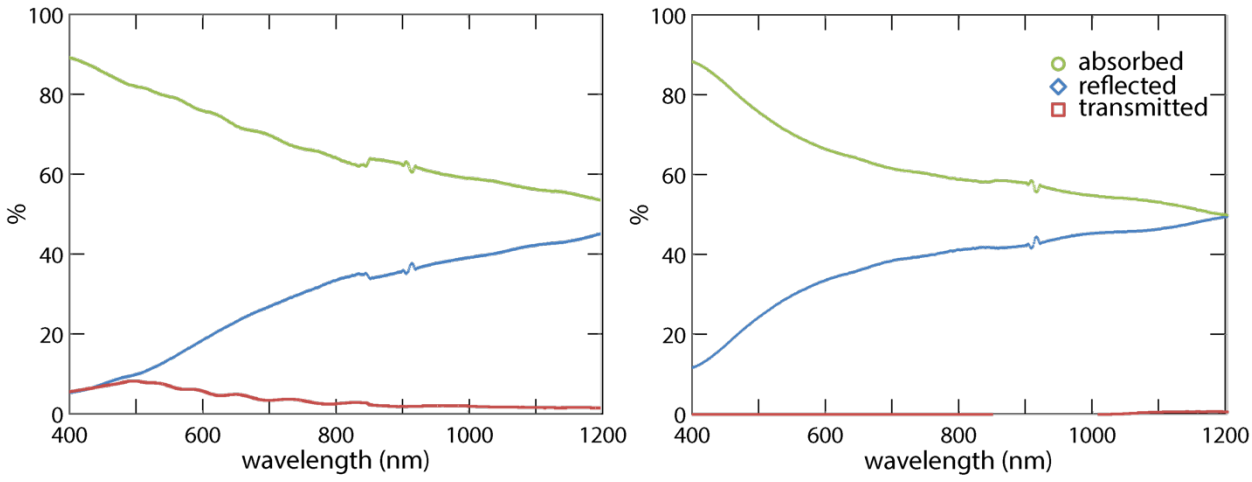

Figure 3.8: *The spectrophotometry results for each pyramid design, showing the percent of light*

absorbed, reflected, and transmitted as a function of wavelength. (left) Results for the inverted pyramids. (right) Results for the upright pyramids.

3.2.2 Cargo delivery

HeLa CCL-2 cells are cultured in DMEM containing 10% (FBS) and 1% penicillin streptomycin and are incubated at 37 °C and 5% CO2. Cells are passaged every other day and used for experiments at 80% confluence between passage numbers 15 and 30. Cells are washed with 8 mL of PBS and incubated for 3 min with trypsin (5 mL) before being neutralized with cell media (13 mL). Pipetting is used to wash the bottom of flask five times with the cell mixture before the mixture is transferred to a 15 mL tube and centrifuged for 5 min at 125g. The supernatant is removed gently with vacuum pipette, and cells are resuspended in 8 mL of fresh media and pipetted 30 times (up and down counted as 1 time). We use a Countessa cell counter to measure cell density and viability. Healthy cells have 90–99% viability. Eight template-stripped substrates are taped lightly to the bottom of a 100 mm Petri dish with double-sided Kapton tape. Five million cells are suspended in 15 mL of fresh cell medium and added to the Petri dish for overnight incubation. Figure 3.8 shows how the cells are grown onto the gold pyramids. Both imaging methods indicate that each cell adheres to approximately 40–50 pyramids, which enables the excitation of specific regions of the cell by targeting local hotspots.

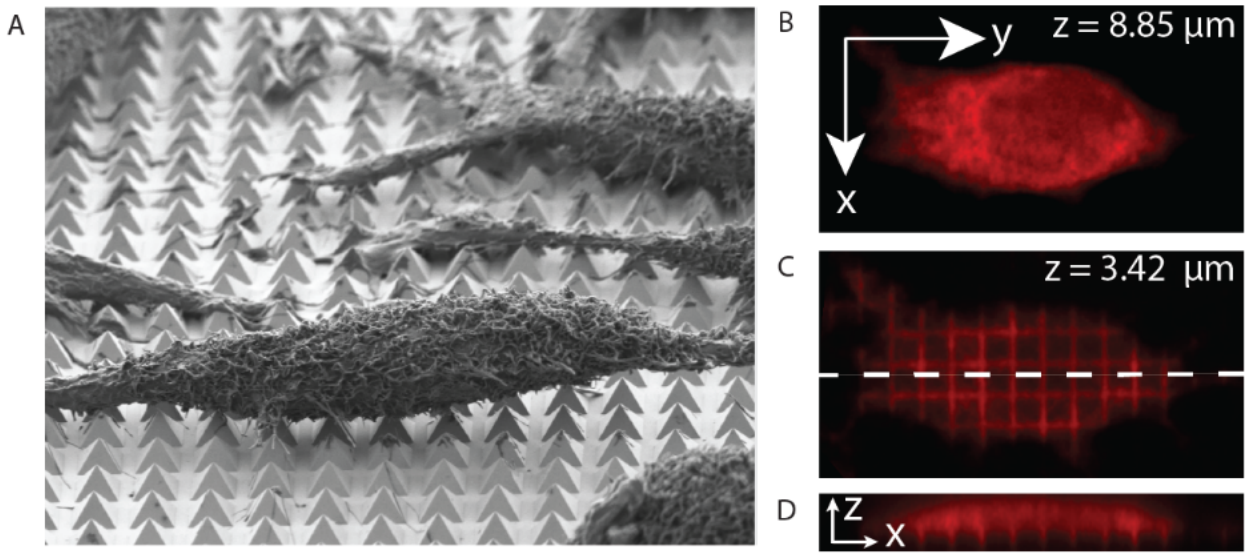

Figure 3.9: *Cell morphology on gold pyramid substrate. (A) SEM of chemically fixed HeLa CCL-2 cells on a thermoplasmonic substrate. (B) Confocal laser-scanning microscopy slice of cell with calcein red-orange AM fluorescence at z = 8.85 µm, as measured from the bottom of the cell. The cell is 40 µm in length. (C) Grid pattern from pyramids. (D) 27 z-slices stacked (with spacings of 0.57 µm) to show a cross section of the same cell taken along the dotted line in (C).*

Substrates with cells on the surface are transferred to a 35 mm Petri dish, and 2 mL of prewarmed PBS (37 °C) solution containing the molecules to be introduced into the cells (Calcein green at 500 µM or FITC–dextran at 25 mg/mL) is added. The laser setup is shown in Figure 3. A Gaussian beam of 1.2 mm in diameter is exposed onto the sample, which sits on an x–y translational stage. The Petri dish contains the dye to be delivered in PBS solution.

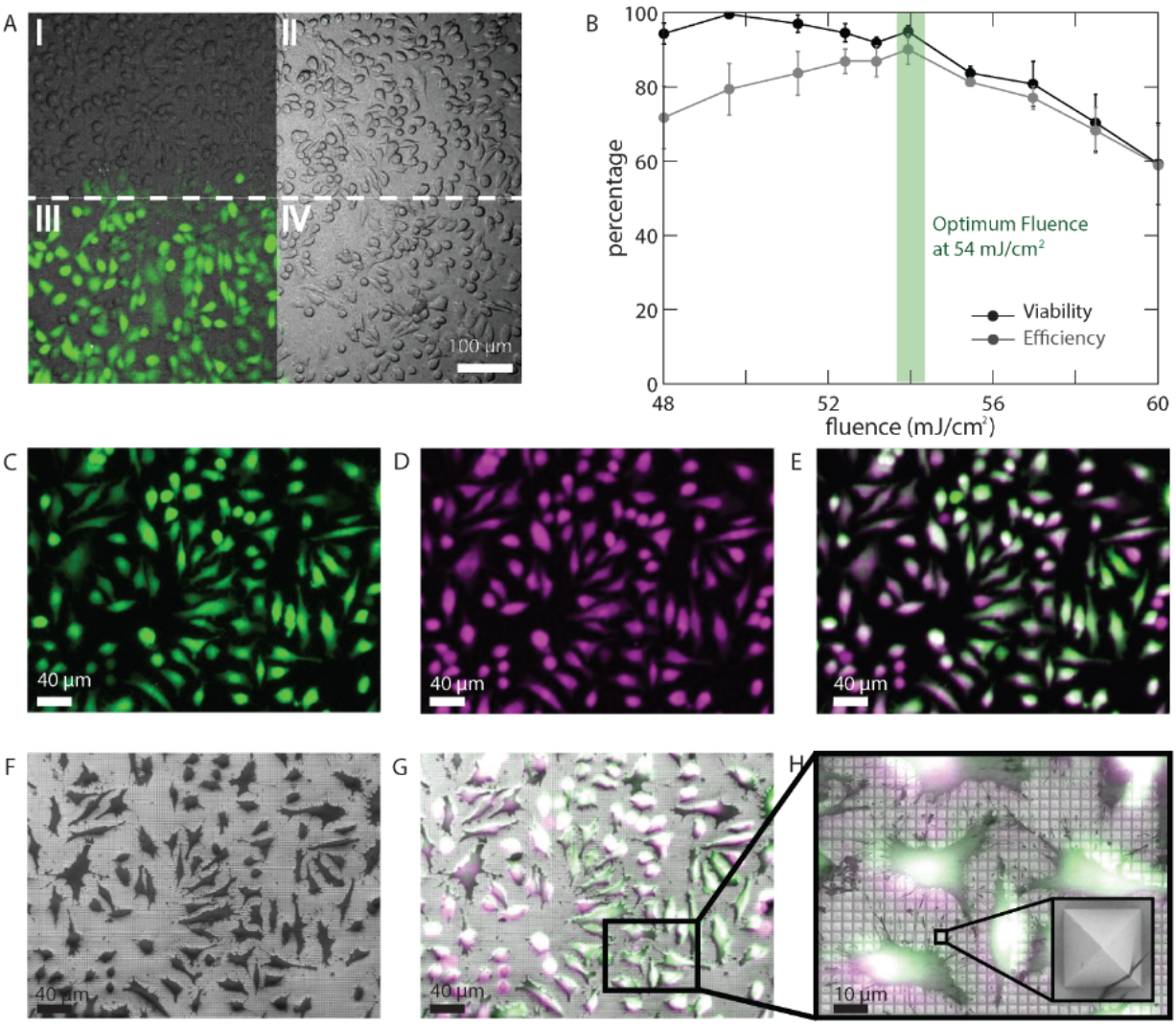

Figure 3.10: *Characterizing the efficiency and viability of delivery to cells, and confirming no visible substrate damage. (A) Overlay of a bright-field and fluorescent image. Areas I and III have pyramids. Areas II and IV are flat gold. A laser is scanned below the dotted line. Area III is the only region with green molecules delivered to cells. (B) Delivery efficiency and viability as a function of laser fluence. Data represent mean ± standard error from n = 3 independent experiments. (C) Calcein green delivery. (D) Calcein red-orange AM viabilty. (E) Overlay of images (C) and (D). (F) SEM image after chemical fixing. (G) Overlay of images (E) and (F). (H)*

Zoom in. Inset of an individual pyramid (2.4 μm base length) confirms no visible damage on pyramid. Filopodia of a cell at the bottom right corner of the pyramid.

Experiments demonstrate that laser- scanning a thermoplasmonic substrate covered in HeLa cells leads to intracellular delivery of cargo that is dissolved in the surrounding solution in a spatially selective manner. In Figure 3.9a, we overlay a bright-field image with a fluorescent image with excitation and emission wavelengths of 495/515 nm, respectively. Areas I and III contain gold-coated pyramids, whereas areas II and IV are flat gold. Areas III and IV were laser-scanned, while areas I and II were not. Only area III, the area containing gold-coated pyramids that is irradiated by the laser, demonstrates the successful delivery of cell-impermeable Calcein green molecules. This observation confirms that gold- coated pyramids in combination with laser irradiation leads to the delivery of molecules into cells. Figure 3.9a demonstrates that the technique offers spatially selective delivery and works only when cells are cultured on pyramids and laser-scanned. Note that the pyramidal surface on the left reflects less light than the flat gold on the right, making the surface appear darker.

We determined the efficiency of Calcein green delivery to HeLa cells (Figure 9c) and used a second dye, Calcein red- orange AM, to check the postexperimental viability of the cells 4 h after the experiment (Figure 3.9d) in a small region of the substrate. The overlay of the efficiency and viability in Figure 3.9e demonstrates that cells with Calcein green delivered to the cytoplasm survive the experiment. To determine how many cells had Calcein green delivered to the cytoplasm (efficiency) and how many of those cells were alive in the Calcein red- orange AM channel (viability) we used automated cell counting on fluorescent images. Fluorescence microscopy was done on an upright microscope to image Calcein green and Calcein red-orange AM. Automated cell counting of fluorescent images was done using Fiji Image processing software using

fluorescent images of the samples. The final cell count was checked to make sure that none of the cells were missed. Additional cells were added in the cell counter window. Triplicate experiments were performed for all data sets. The percentages were calculated as follows:

$$Efficiency\ \% = \frac{Number_{green\ cells}}{Number_{control}} \times 100$$

$$Viability\ \% = \frac{Number_{red\ cells}}{Number_{control}} \times 100$$

We determined the optimum laser fluence for maximum delivery efficiency and viability by repeating each experiment described above on three separate substrates in three separate dishes at different laser fluences. Figure 3.9b shows the fluence dependence of the efficiency and viability. At the lowest fluence (48 mJ/cm^2) in Figure 3.9b, the viability is 98% and the efficiency is 70%. This means that most of the cells are surviving the laser treatment, but only 70% of them have cell- impermeable cargo (Calcein green) inside them. As the laser fluence is increased to 54 mJ/cm^2, 95% of the cells have Calcein green in them, and 98% of them are still viable. We define this point as our optimum fluence as viability and efficiency are maximized. Increasing the laser fluence beyond this point leads to the onset of cell death, as can be seen starting at 56 mJ/cm^2, where the viability drops to 80%. The efficiency is also around 80% and continues to follow the viability curve closely at higher fluences. This trend occurs because Calcein green can only remain within a cell if the cell is alive and has an intact cell membrane. Since a fraction of the cells begin to die starting at 56 mJ/cm^2, the efficiency decreases accordingly with viability. Past the optimum fluence, cells either survived the laser irradiation, had cell-impermeable cargo within, or were not viable anymore.

To determine if the pyramids experience any visible damage or melting during laser exposure at 54 mJ/cm^2, we chemically fixed the cells after laser scanning and took an SEM image

of the substrate. As Figure 3.10 illustrates, the pyramids in the laser- treated area experiences no visible damage despite undergoing intense thermoplasmonic heating at the apex (inset Figure 3.9h). We observe no damage to the pyramids in the fluence range 48–90 mJ/cm^2 (Figure 10). All subsequent experiments are performed at the optimum fluence of 54 mJ/cm^{2}because it offers the highest efficiency and viability and no visible damage. However, at 200 mJ/cm^2, we see gold melting at the pyramid apex (Figure 3.10e).

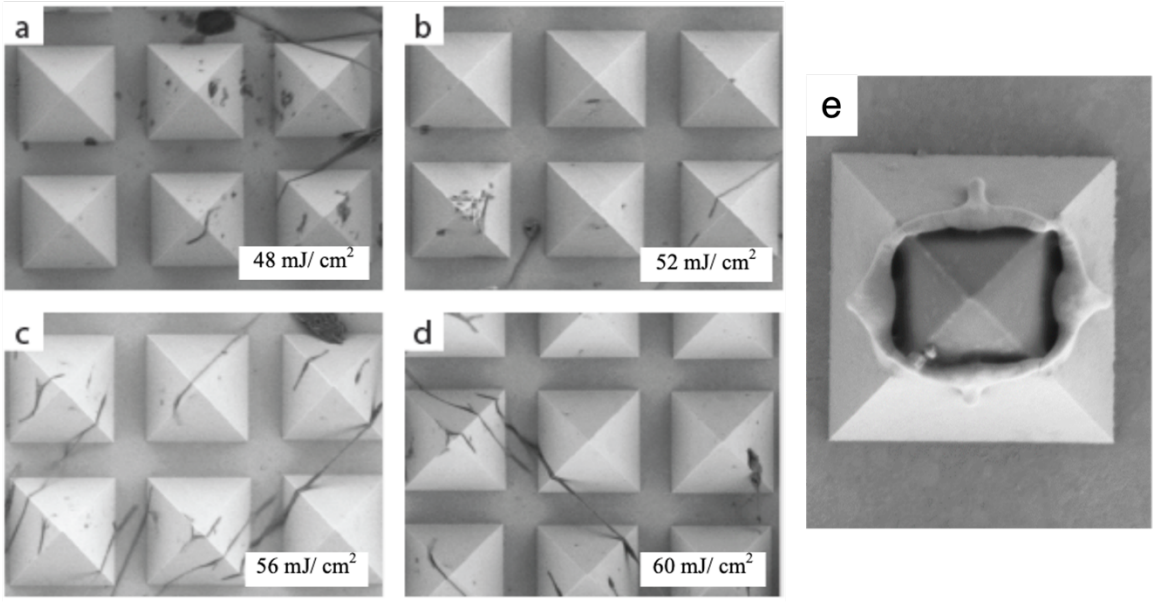

Figure 3.11: *(a – d) SEM images of pyramids after intracellular delivery. No damage observed on substrate after laser experiment at different fluence scans. Pyramids have base lengths of 2.4 μm. The dark lines and spots on the pyramids are portions of cells that remain after chemical fixing. (e) Damage image. SEM image of a pyramid after laser illumination at a fluence above 200 mJ/cm2. Severe melting is observed on the pyramid apex irradiated at high fluence. The damage indicates that melting only occurs in the thin metal film and there is no visible effect on the polymer layer under the gold film. The pyramid has a base length of 2.4 μm.*

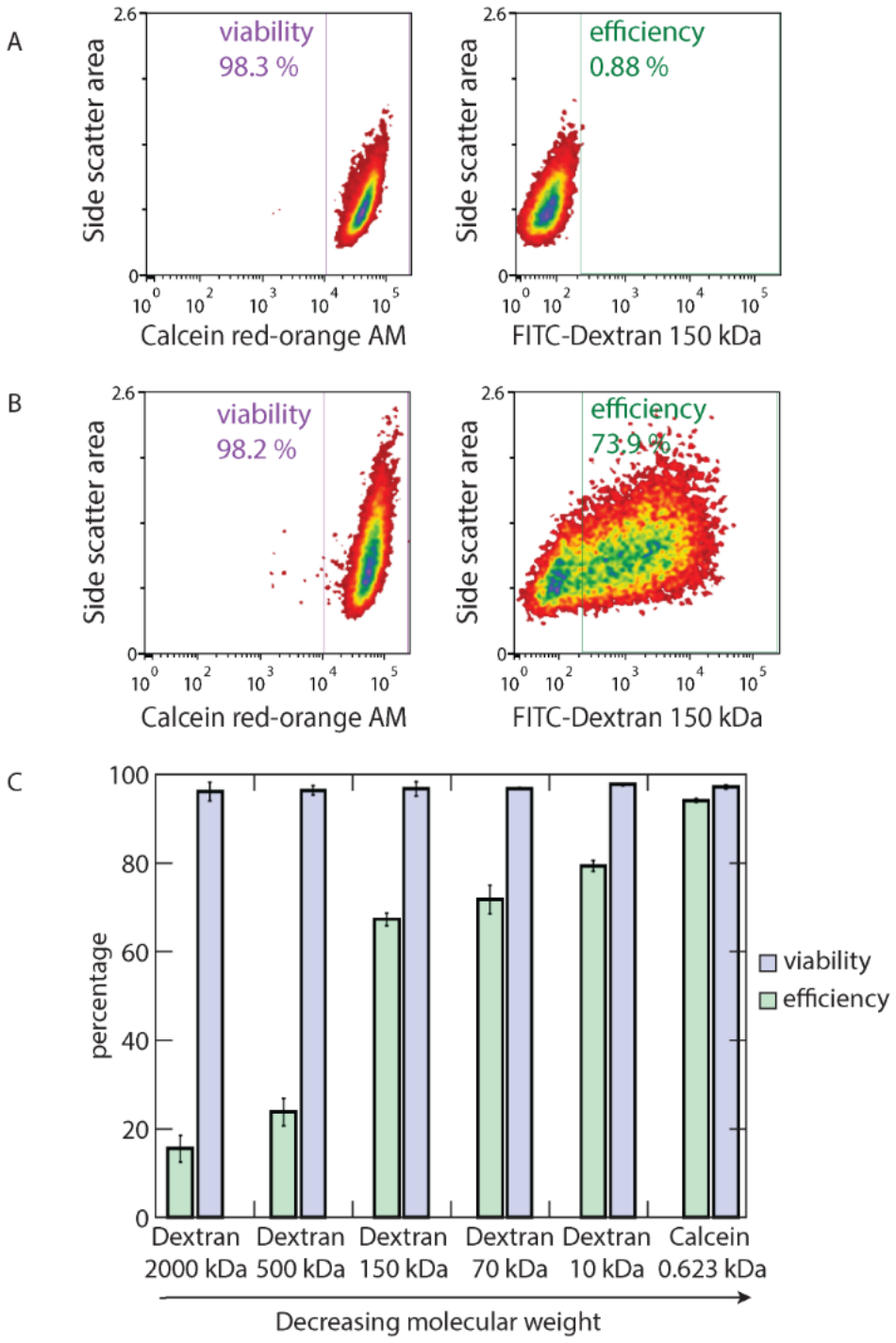

Figure 3.12: *Quantifying efficiency and viability of different-sized molecules using flow cytometry. (A, B) Representative data from FITC-Dextran 150 kDa experiment. The experimental sample (A) is laser scanned while the control (B) is not. A density plot of side scatter-area vs.*

calcein red-orange AM fluorescence determines viable cells. The viable cells are plotted in a side scatter-area vs. FITC- Dextran 150 kDa density plot to measure the delivery efficiency. The background signal is less than 1% in the control in (A). The delivery efficiency is 74% in the experiment (B). (C) Viability and efficiency for FITC-cargo ranging in size from 0.623 kDa to 2000 kDa. Data represent mean ± SE from n = 3 independent experiments.

We performed flow cytometry experiments to quantify the delivery efficiency and viability of cells for delivery of different cargo sizes with triplicate experiments performed on different substrates on the same day. We delivered a range of cargos (Calcein green, dextran 10 kDa, dextran 70 kDa, dextran 150 kDa, dextran 500 kDa, and dextran 2000 kDa) to 1 million HeLa cells by laser scanning the entire thermoplasmonic substrate in 3 min. We then used trypsin to detach the cells from the substrate to prepare them for flow cytometry measurements. Flow cytometry measured the forward and side-scattered light and the fluorescence of cells passing through a beam of light. The forward and side scattering gave information about cell size and internal granularity, respectively.

Figure 3.12 compares viability and delivery efficiency of cells that were not laser-scanned (Figure 3.12A) and cells that were laser-scanned (Figure 3.12B). For the substrate that was not laser- scanned, the viability is 98.3%, and the background signal for delivery is less than 1% (Figure 3.12A). For the laser-scanned substrate, the viability is 98.2% and the delivery efficiency is 74% (Figure 3.12B). The delivery scatter plots show a range of fluorescence signals, indicating that different amounts of FITC- cargo entered the cell. We performed triplicate independent experiments with flow cytometry for cargo sizes ranging from 0.6 to 2000 kDa. The largest cargo, FITC–dextran 2000 kDa, is delivered with an efficiency of 16% and a viability of 97% (Figure 3.12C). The largest increase in efficiency is between FITC–dextran 500 kDa (24%) and

FITC–dextran 150 kDa (68%). Calcein green (0.623 kDa) is delivered at 95% efficiency and 98% viability. We attribute the increased efficiency with decreasing cargo size to faster diffusion of smaller molecules. The cargos we delivered match functional proteins in molecular weight (13–150 kDa).

We observe cells proliferating after thermoplasmonic treatment, indicating high cell viability at 48 h after laser treatment (Figure 3.13). Dextran 150 kDa is retained in the cytoplasm during proliferation over 48 h.

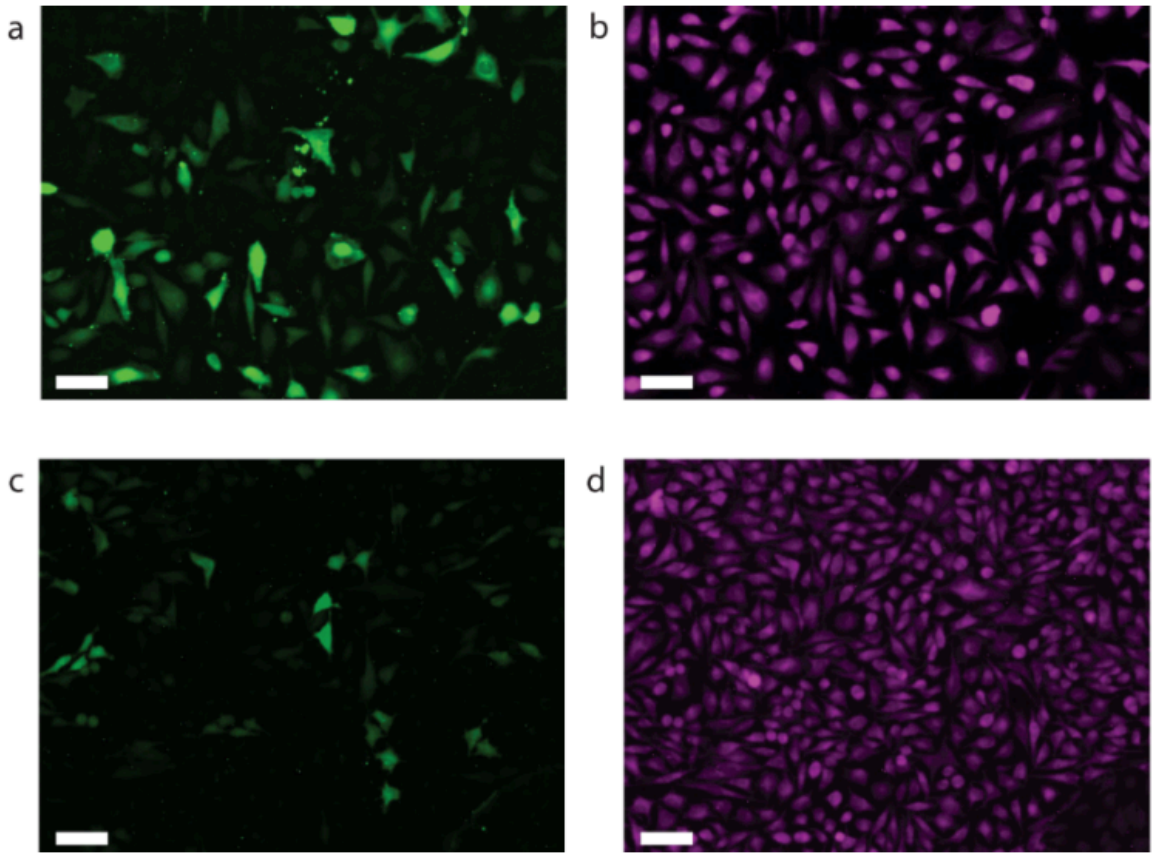

Figure 3.13: *Cells proliferate over 48 hours, with cargo inside. (a) FITC-Dextran 150 kDa delivery after 24 hours. (b) Calcein AM channel viability after 24 hours. (c) Dextran 150 kDa retention after 48 hours of the same region. (d) Viability after 48 hours. Cell density is higher after*

48 hours, indicating that the cells not only remain viable but continue to divide after the laser experiment. Scale bar is 50 μm.

The same cell culture and analysis protocols were used for the TiN inverted pyramids and upright pyramids. As shown in Figure 3.14, inverted pyramids achieve a maximum poration efficiency of 83% and a viability of 95% at a laser fluence of 16.5 mJ/cm^2 (Fig. 3.13d). As the laser fluence decreases/increases below/above 16.5 mJ/cm^2, there is a drop in poration efficiency, and viability decreases with increasing laser fluence. For the upright pyramids, the maximum poration efficiency of 66% occurs at a laser fluence of 15.8 mJ/cm^2 (Fig. 3.13e). At this fluence, the viability is 67%. Viability maximizes at 82% at 13 mJ/cm2 and decreases as the laser fluence increases. Overall, both designs show encouraging results in efficiency and poration. The inverted pyramids' maximum efficiency of 83% and viability of 95% are very close to the values achieved through the gold upright pyramids.

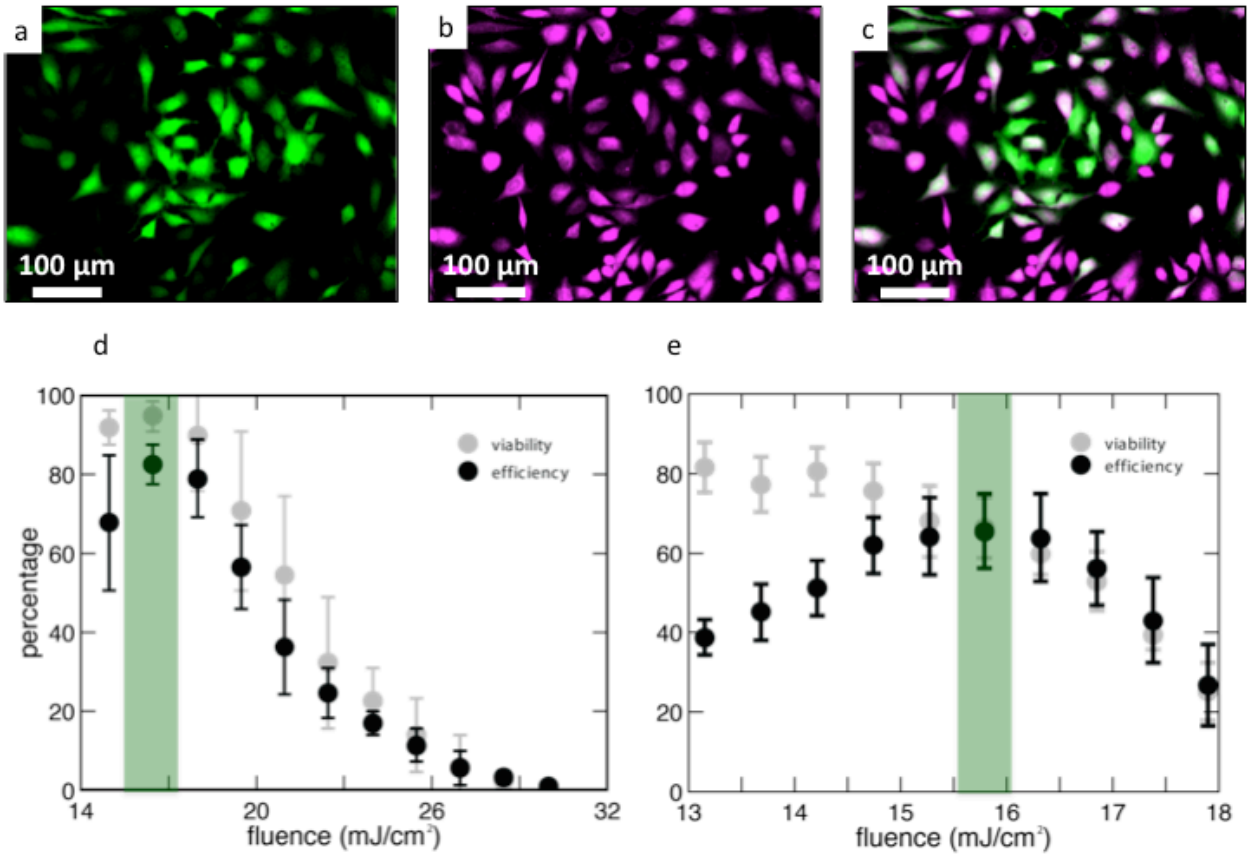

Figure 3.14: *Cell poration efficiency and viability results. (*a-c*) represent an example of cell counting methodology (*a*) Green cells represent cells that were porated and uptook Calcein Green dye. (B) The same area of cells showing the cells that survived. (*c*) An overlay of* (a) *and* (b)*, revealing cells that were porated and survived. (*d*) Quantified efficiency and viability results for the inverted pyramid substrate. The green bar highlights the optimal fluence for maximum efficiency and viability. (*e*) Quantified efficiency and viability results for the upright pyramids. The green bar highlights the optimal fluence for maximum efficiency and viability. Error bars represent* standard error *with n = 3.*

3.2.3 Pore dynamics

In this section, we use laser-activated plasmonic substrates consisting of template-stripped gold pyramids to induce membrane pores and study resulting changes in the area, cell position, pore size, morphology, and cytoskeleton behavior. C2C12 cells were cultured in Dulbecco's modified Eagle's Medium with high glucose containing 10% FBS and 1% penicillin streptomycin and incubated at 37 ºC and 5% CO2. Cells were passaged every other day and used for experiments at 50% confluence, between passage numbers 15 and 30. Cells were seeded on the substrate the day before experiments and placed in pre-warmed Phosphate Buffered Saline (PBS) for experiments for improved imaging. For differentiation, cells were grown to confluency before the medium was changed to differentiation medium containing 1% horse serum, 1 μM insulin, and 1% penicillin streptomycin. Cells were differentiated for 5 days before experiments, and cell medium was exchanged every day during differentiation.

Calcein AM and propidium iodide were used for time-lapse imaging of in- and outflow of dyes to investigate pore dynamics. Both dyes have previously been used in literature to investigate flow in- and outside of cells. We labeled C2C12 cells with 1 μM Calcein AM in PBS for 10 min at 37° C and washed once to reduce background fluorescence. Calcein AM is non-fluorescent initially due to an ester-bond-attached group (AM) that quenches fluorescence and makes the dye permeable to the plasma membrane. Once inside a viable cell, the quenching group is cleaved by intracellular esterases, leaving a membrane-impermeable, fluorescent dye molecule, Calcein, inside the cell. Propidium iodide was used at a concentration of 10 μM for inflow experiments as it can enter through the induced pores upon poration. This high concentration for inflow experiments was chosen to obtain a robust fluorescence signal at early time-points after cell perforation.

For laser exposure, a 532-nm pulsed Nd:YAG microchip laser with a pulse duration of 850 ps and repetition rate of 20.25 kHz was used. The laser spot diameter was 80 μm. We use an inverted fluorescence microscope to image C2C12 myoblast cells cultured on a gold pyramidal substrate. An 850-ps laser source illuminates the substrate at a repetition rate of 20.25 kHz to generate plasmonic hotspots at the tip of each pyramid, leading to the formation of heat-mediated bubbles. The plasma membrane is transiently permeabilized, enabling the exchange of intra- and extracellular molecules.

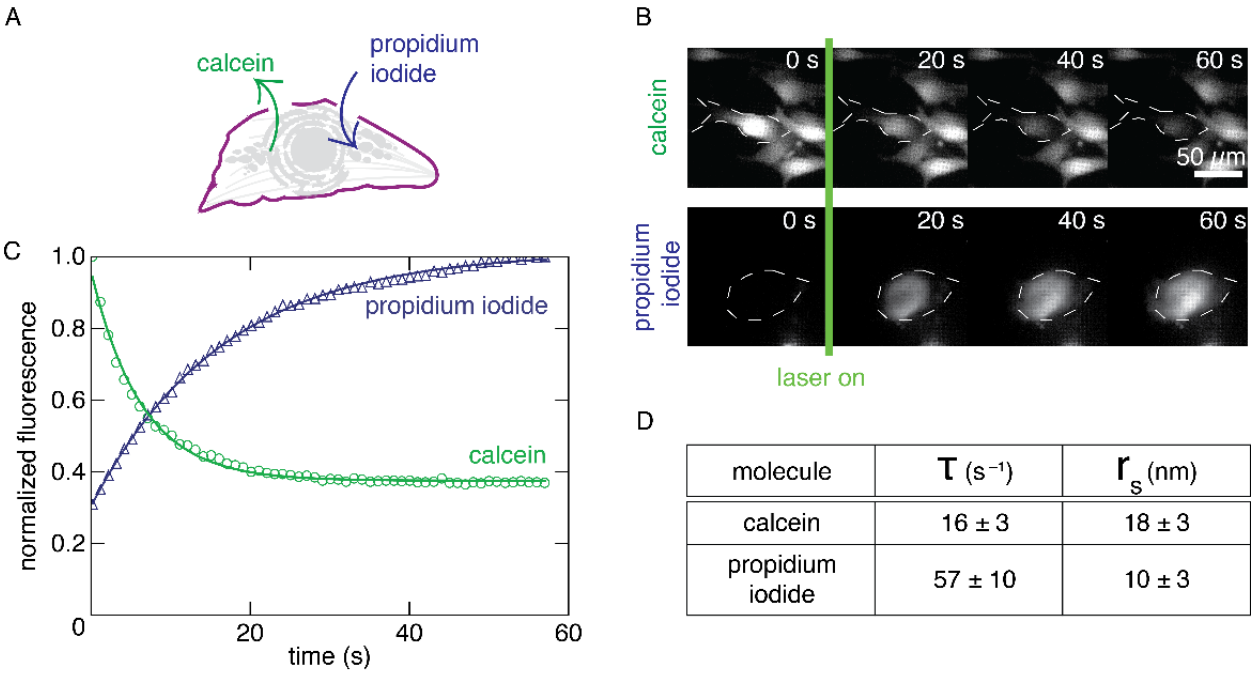

molecule	τ (s^{-1})	r_s (nm)
calcein	16 ± 3	18 ± 3
propidium iodide	57 ± 10	10 ± 3

Figure 3.15: *Determining the pore size using time-lapse imaging. (A) Calcein outflow and propidium iodide inflow. (B) Time-lapse imaging of C2C12 cells to determine the decrease in fluorescence over time at 10 frames per second (fps) for 60 s. Outlines of cells show the region in which fluorescence signal is measured. (C) Relative fluorescence of calcein and propidium iodide over time. The data is fitted to Eq. 2. (D) Data showing in/outflow exponential constants* τ *and a pore radius* r_s *of 18.4 ± 2.9 nm with calcein and 9.7 ± 3.4 nm with Propidium Iodide. Numbers obtained from three independent experiments, using five cells for each experiment.*

The number of molecules entering through pores in the plasma membrane is determined by the diffusivity of the molecule and by number and size of the induced pores and the time they remain open. The pore dynamics not only affect the delivery efficiency, but also affect membrane recovery. We measured calcein outflow and propidium iodide inflow to determine the size of the pores (Fig. 3.15). Time-lapse imaging of C2C12 cells shows a decrease in fluorescence from calcein (molecular weight 623 Da) and an increase in fluorescence from propidium iodide (670 Da) (Fig. 13.14b). Figure 2C shows the time-dependence of the relative fluorescence of calcein and propidium iodide in a single cell. The cell shows a reduction from a relative fluorescence value of 1 to 0.4 for calcein over 30 s and an increase from 0.3 to 1 for propidium iodide over 60 s (Fig. 3.14c). These timescales are different because calcein is a small diffusive dye molecule, whereas it takes additional time for the propidium iodide to bind with a nucleic acid complex. [92]

To determine the pore radius from these data, we consider a substrate-induced hole of radius r in the plasma membrane. As proposed by Davis, *et al.*, we take the radius r to be constant during the time it is open before closing rapidly. [56] The dye concentration in the cell $\Phi(t)$ then changes exponentially:

$$\Phi(t) = \Phi(0)\exp\left(-\frac{t}{\tau}\right) \quad , \qquad (1)$$

where $\Phi(0)$ is the initial fluorescence, t is the time, an τ is the decay/growth constant. The flow through the hole is given by [93]:

$$\frac{d\Phi(t)}{dt} = \frac{\pi r^2 D}{\left(\Delta Z + \frac{2\pi r}{4}\right)V}\,\Phi(t) \, , \qquad (2)$$

where D is the diffusion coefficient, ΔZ is the membrane thickness, and V is the volume of the cell. Using a diffusion coefficient D of 3.64^{-10} m^2/s for calcein and a cell volume V of 1200 μm [56], we obtain the hole radius r from the decay/growth constant in Eq. 2:

$$\tau = \frac{(\Delta Z + \frac{2\pi r}{4})V}{\pi r^2 D}, \qquad (3)$$

Davis *et al*. consider a single pore forming in the cell, whereas the plasmonic substrates used in this work induce multiple pores. Given the large pyramids peak-to-peak spacing of 1.6 μm, we assume that each pyramid induces a separate pore, and we take the radius of an individual pore to be $r_s = r/\sqrt{N}$, where N is the number of pyramids within the laser-exposed cell area. This approach yields a pore size of 18 ± 3 nm using the calcein data and 10 ± 3 nm using the propidium iodide data. We assume that both molecules diffuse through similar pores. The difference in value can be attributed to the slower rate of diffusion of propidium iodide, which only fluoresces upon binding to nucleic acids within the cell — a fact not accounted for in the pore size model. The propidium iodide diffusion would be mediated by the molecule itself and by the bound nucleic acid, while calcein diffuses independently. However, both values are of the same order of magnitude.

The pore radius sizes are in agreement with experiments delivering dextran molecules that have a Stokes radius in the range of 20 nm. [22,63] Membrane resealing occurs at this pore size. [46,94] However, a large number of simultaneous larger pores on the membrane leads to cell death at high fluences. About 70–80 pyramids contribute to the poration for each cell. Since the pyramids have a peak-to-peak spacing of 1.6 μm, each pyramid leads to an individual pore. We assume that due to this large spacing, it is possible to treat all fluid below the cell and in between the pyramids as

bulk fluid. However, as the pyramid tips are attached to the cell and might influence or hinder some inflow of molecules, our calculated pore size may be slightly underestimated.

Through this simple diffusion experiment, we develop a biophysical understanding of the poration process by quantifying changes in living cells. The resulting pore radius is in the range of 10–20 nm, which would decrease by 5–10% after laser exposure, and stabilizes after 30 min. Developing a biophysical understanding of the poration process enables the safe development of this technique for therapeutic applications.

3.2.4 Discussion

We demonstrate that nanosecond-laser excitation of template-stripped thermoplasmonic substrates offers an alternative intracellular delivery technique for cargos of different sizes. We use laser irradiation to form hotspots at the apex of gold-covered pyramids on a substrate. These hotspots make the surroundings, within a nanoscale region (tens of nanometers), reach high temperatures and permeabilize the membranes of cells adhering to the substrates and the temporary pores allow for cell-impermeable cargo to diffuse into the cytoplasm. The ability to deliver cargos ranging in size from 0.623 to 2000 kDa to cells makes this technique applicable to different research and clinical applications. The cargos delivered (especially the 70 and 150 kDa) are the same size as biologically relevant cargos, including proteins and antibodies, making this technique valuable for studying cellular function, accelerating drug discovery, enhancing gene therapy, and improving high-throughput screening technologies.

We also fabricated and delivered cargo to TiN micropyramid arrays in the inverted formation and the upright formation. Because this platform can be optimized further, there is great promise for improvements in intracellular delivery via TiN micropyramid substrates. Further research is required to study the reusability of the substrates as they have more robust mechanical

properties than the gold pyramids. Understanding the interaction between different materials in an optimal geometrical design is crucial to achieving this goal, for material interface effects such as differential heat expansion could have significant impacts on device performance and sustainability over time. In addition to optimization, a pump probe setup could be used to test temperatures reached during irradiation and to validate the pore-opening mechanism overall.

3.3 Self-assembled nanocavities

Optoporation, a physical delivery technique, utilizes a tightly focused laser beam to create a transient pore in the cell membrane. This technique offers high delivery efficiency and high cell viability. As a consequence of the physical nature of the process, optoporation is inherently versatile with respect to the chemical nature of the cargo and the cell type to be used. However, each cell must be porated individually by focusing the laser beam directly onto the membrane, putting limitations on the throughput. Modifications, including the use of active flow in microfluidic channels and a nondiffracting beam, slightly increase the throughput but not to the scale necessary for therapeutic applications, which require on the order of 1×10^8 cells. [95] Laser-activated thermoplasmonic nanostructures improve the throughput of this delivery technique by efficiently absorbing the laser energy at multiple localized hotspots and transferring energy to the surrounding medium. [96] This transfer of energy to the surrounding solution results in the creation of a bubble or pressure wave that generates a transient pore in the cell membrane. [62,97]

While laser-activated nanostructured substrates are a promising option for intracellular delivery, their small feature sizes typically require nanofabrication techniques that are serial in nature, and necessitate expensive and sophisticated instrumentation and clean room infrastructure. [21,22,98,99] These limitations hinder a widespread use of these substrates in research and technology. Here, we employ colloidal self-assembly and templating to design defined thermoplasmonic

nanocavity arrays over macroscopic areas. We show that these structures permit efficient laser-activated cell poration with high throughput and high spatial resolution, enabling the delivery of model components with different molecular weights with high efficiency and cell viability.

Figure 2 shows the delivery of membrane-impermeable cargoes into cells using a laser-activated self-assembled thermoplasmonic nanocavity substrate. The substrate consists of silica nanocavity structures coated with a thin titanium (Ti) film. Upon illumination with a nanosecond pulsed laser, the laser energy is absorbed by the metallic nanostructures and converted into thermal energy, resulting in localized heating. This high and rapid heating results in the formation of bubbles in the surrounding aqueous environment. When cells are cultured on the substrate, these bubbles porate the cell membrane that is in contact with the substrate. Membrane-impermeable molecules in the surrounding cell medium then diffuse through these pores into the cell before the cell membrane heals and seal the pores, encapsulating the cargo within the cell.

3.3.1 Fabrication of nanocavities

We use colloidal self-assembly and templating for the fabrication of the substrates, as schematically illustrated in Figure 15a. In the process, we take advantage of the ability of monodisperse colloidal particles to form close-packed, two- dimensional crystals at the air/water interface. [77] These close- packed, two-dimensional assemblies form as a result of attractive capillary forces acting on the colloidal particles at the air/water interface.

Colloids were synthesized by surfactant-free emulsion polymerization using styrene and acrylic acid as comonomers. The colloidal monolayer was fabricated by addition of a colloidal solution (50% water, 50% ethanol, solid content approx. 5%) to the air/water interface of a crystallization dish via a hydrophilic glass slide followed by manual transfer to a solid substrate; following a process from literature. [73] A No. 2 glass coverslip was used as a substrate. The transfer

of colloids to the coverslip was performed by carefully submerging the coverslip into the water and withdrawing it at a shallow angle with respect to the surface of the water.

To prepare the inverse colloidal monolayer, a protocol from literature was adopted. The colloidal monolayer is then backfilled with tetraethylorthosilicate as the silica sol–gel precursor material. The concentration of the sol–gel precursor is chosen to partially fill the colloidal monolayer, embedding the polymer colloids in a silica matrix. [100] In brief, a silica precursor solution of tetraethyl orthosilicate (TEOS), 0.1 N hydrochloric acid (HCl), and ethanol was mixed in a ratio of 2:1:1.5 by mass and stirred at room temperature for 1 h. The solution was then diluted with ethanol at a ratio of 1:1.1. 32.4 μL of the diluted solution was pipetted onto the colloidal monolayer on the glass coverslip. The solution was spread by spincoating at 3000 rpm for 30 s. The sample was calcined by heating from room temperature to 500 °C for 5 h, maintaining at 500 °C for 2 h, and cooling for 5 h to room temperature. Upon calcination at 500 °C, the organic colloidal particles combust, resulting in an array of nanocavities, termed an inverse colloidal monolayer. [101] Finally, 50 nm of Ti was then deposited onto the samples using an electron-beam evaporator.

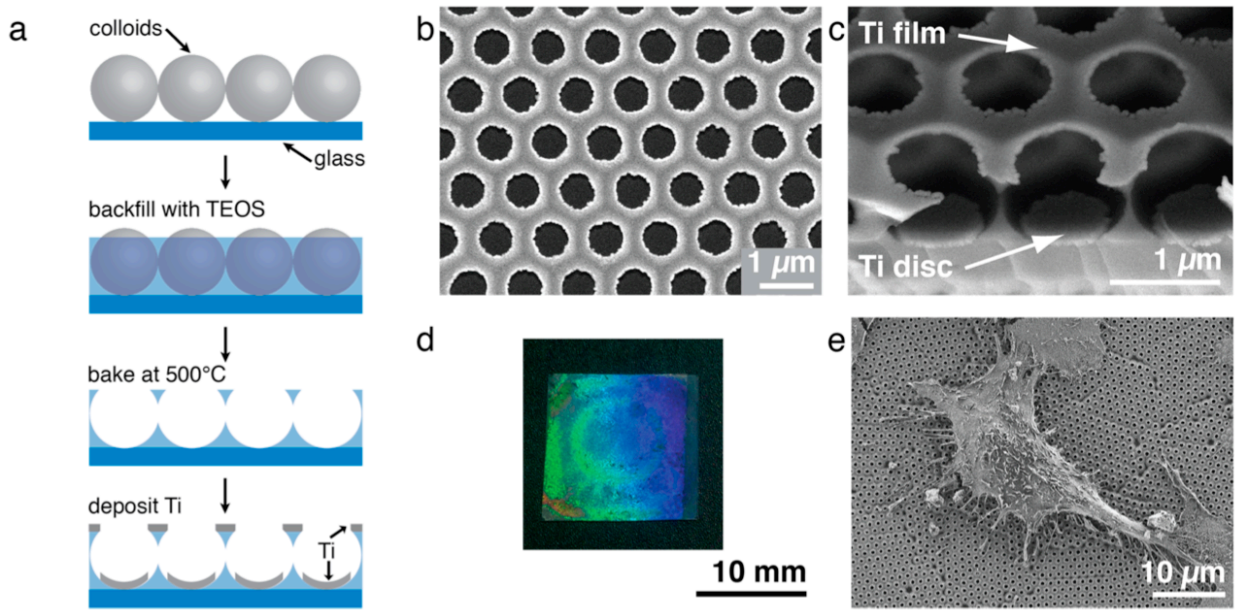

Figure 3.16: *Fabrication and characterization of self-assembled thermoplasmonic nanocavity substrates. (a) Fabrication process for the thermoplasmonic nanocavity substrate. (b) Photographic image of a thermoplasmonic nanocavity substrate. (c) Top-down scanning electron microscopy (SEM) image of nanocavities. The cavities are approximately 1 μm in diameter with pore openings of about 800 nm. (d) Tilted SEM image of nanocavities, showing the continuous porous Ti film on top of the nanocavities and the disconnected Ti discs at the bottom. (e) SEM image of chemically fixed HeLa CCL2 cell on the nanocavities. Each cell covers approximately 300 to 700 nanocavities, depending on the size of the cell.*

A top-view scanning electron microscopy (SEM) of the thermoplasmonic nanocavity substrate shows the uniform and regular arrangement of the nanopore array with pore diameters ranging in diameter from ~750 to 850 nm. The hexagonal symmetry of the pores reflects the symmetry of the colloidal templates (Figure 3.16b). The diameter of the pores is determined by the concentration of the sol–gel solution and can be precisely adjusted. The presence of the titanium nanostructures as a continuous film with nanopores and separated, individual discs at the

bottom of the nanopores can be directly seen in the inside-view SEM images (Figure 3.15c). The diameter of the cavities is about 1 μm and is determined by the size of the colloids used to form the monolayer.

Figure 3.16d shows a photograph of a thermoplasmonic nanocavity substrate completely and homogeneously covering a 14 mm by 14 mm glass coverslip. The structural coloration arising from the nanostructured surface coating demonstrates the high degree of uniformity of the self-assembled thermoplasmonic substrate over macroscopic dimensions. Figure 3.15e shows the morphology of a chemically fixed HeLa CCL-2 cell on one of the nanocavity substrates. Each HeLa CCL-2 cell covers several hundred nanocavities, with the exact number of nanocavities deter- mined by the size of the cell and how it adheres to the region. The density of nanocavities can be modified by altering the size of the templating colloidal particles, enabling the optimization of the number of nanocavities per cell and thus the poration efficiency for any chosen cell type.

3.3.2 Cargo delivery

We investigate the thermoplasmonic poration-induced delivery of molecules into HeLa CCL-2 cells as a function of laser intensity. As a model delivery molecule, we chose calcein green, a 0.623 kDa-sized membrane-impermeable green fluorescent dye. We use fluorescence microscopy to quantify the efficiency of delivery and viability of the cells as a function of the fluence of the applied laser pulses. The same cell counting and cell culture protocol is used for this section as in the above section of the nanofabricated pyramidal substrate. HeLa CCL-2 cells are cultured on the nanocavity substrate before being scanned with a nanosecond-pulsed laser. Only the cells in the laser-scanned region are porated, enabling the diffusion of membrane-impermeable calcein green dye into cells in the irradiated area. Cells expressing green fluorescence indicate successful intracellular delivery of the molecule. As shown in Figure 3.17a, only substrate regions

that have been exposed to laser light produce cells with green fluorescence, while unexposed surfaces remain dark, demonstrating the absence of dye uptake without light irradiation. Importantly, this thermoplasmonic delivery technique provides a high spatial selectivity of the delivered molecules, which may open pathways for the delivery of required substances to defined regions of an engineered tissue. Figure 3.16b shows a fluorescence microscopy image of HeLa CCL-2 cells on nanocavity substrates that were porated to take up membrane-impermeable calcein green dye. We tested the cell viability by staining the cells with calcein red-orange AM 4 h after laser-scanning the substrate. Figure 3.16c shows that the porated and delivered-to cells also express a calcein red-orange AM signal, indicating viability.

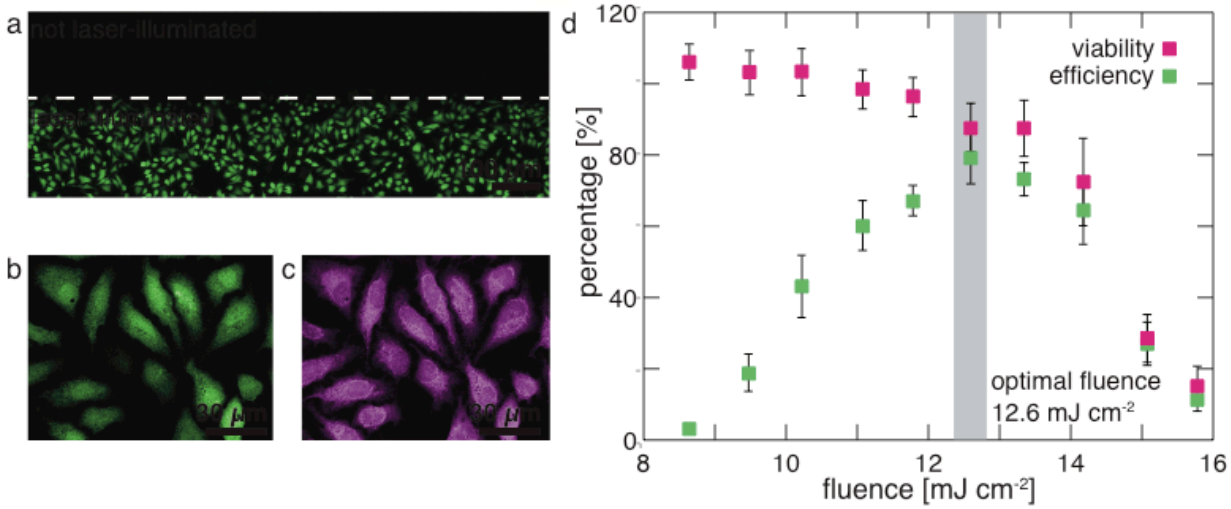

Figure 3.17: *High-efficiency, high-viability, spatially-selective intracellular delivery using self-assembled thermoplasmonic nanocavity substrates. a. Cells are porated and take up fluorescent dye, only in the region irradiated by the laser, demonstrating spatially selective poration. b. HeLa CCL-2 cells fluoresce green upon poration and uptake of membrane-impermeable calcein green dye. c. The same cells fluoresce after incubation with viability indicator Calcein AM, indicating that these cells exhibit healthy metabolic activity and remain viable after laser treatment. d. The nanocavity substrates are laser scanned over a range of laser fluences to determine the optimal*

fluence for maximizing delivery efficiency while maintaining cell viability. Cell counting of fluorescence images indicates a delivery efficiency of approximately 78% and a viability of 87% at a laser fluence of approximately 12.6 mJ/cm2. Data represent mean ± standard error from n = 5 data sets.

To maximize delivery efficiency and cell viability we scanned a single thermoplasmonic nanocavity substrate varying the laser fluence in different locations, repeating the experiment five times (Figure 3.17d). The laser beam was scanned across the substrate by moving the stage holding the sample at a speed of 10 mm/s, which equates to a throughput of ~30,000 cells/minute. This throughput could be easily scaled up by, for example, using galvo-scanning mirrors to scan the laser beam across the sample. To quantify the delivery efficiency and cell viability, we imaged the cells after exposure to the laser light using fluorescence microscopy and performed automated cell counting on the images. The delivery efficiency is defined as the number of cells that contain calcein green dye within a laser-irradiated region divided by the total number of cells in a nonlaser-irradiated region of the same size. The viability is defined as the number of cells that express a calcein AM signal within a laser-irradiated region, divided by the total number of cells in a nonlaser-irradiated region of the same size. It is important to note that, because the cell density is not perfectly uniform across a single substrate, viability values above 100% can result from the normalization procedure. At a laser fluence of 8.7 mJ/cm^2, we observe a delivery efficiency of 4% and a cell viability of 105%. Because the viability is calculated in comparison to the viability in the non-scanned regions, there may be some increase in viability above 100% when compared and calculated. As the laser fluence is increased to 12.6 mJ/cm^2, the delivery efficiency increases, while the cell viability remains above 85%. At a laser fluence of 12.6 mJ/cm^2, we observe a delivery efficiency of 78% and a cell viability of 87%. This delivery efficiency is 4.3 times higher than the

delivery efficiency observed for a comparison experiment, where a 50 nm thin film of Ti was evaporated directly onto an unstructured glass coverslip before being seeded with cells and scanned with a pulsed laser. In the case of the Ti-coated glass coverslip, we observe an 18% delivery efficiency and 88% viability at an optimum laser fluence of 10.8 mJ/cm^2 (Figure 3.17). It is worth noting that, although the glass coverslip is unstructured, the evaporated Ti does have some surface roughness that likely mediates bubble formation upon laser irradiation (Figure 3.18). As the laser fluence increases above 12.6 mJ/cm^2, the cell viability and delivery efficiency both decreases. The delivery efficiency decreases along with cell viability because calcein green only remains inside cells that are viable and have an intact cell membrane. At a laser fluence of 15.8 mJ/cm^2, we observe a delivery efficiency of 12% and a cell viability of 16%. These results show that we obtain maximum delivery efficiency at a fluence of 12.6 mJ/cm^2.

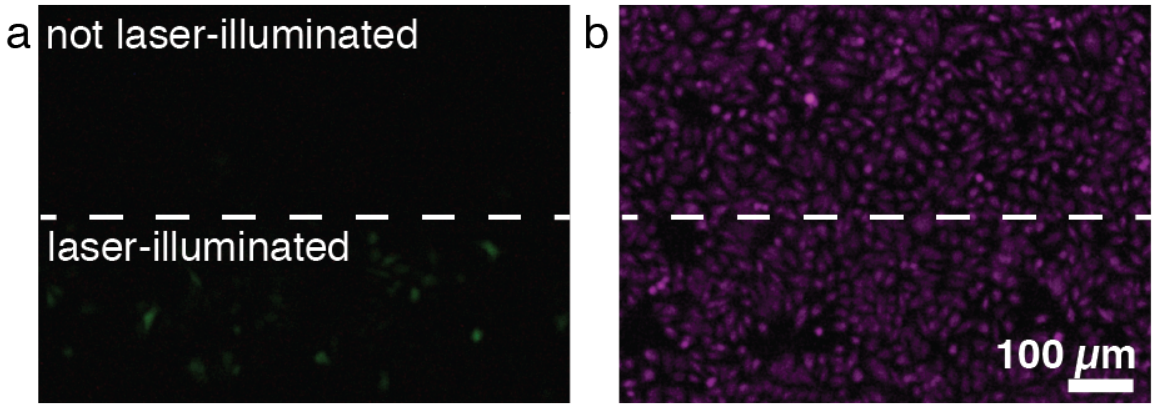

Figure 3.17: *Efficiency and viability of laser-activated delivery using an unstructured glass coverslip coated with 50 nm of Ti. a. A small percentage of HeLa CCL-2 are porated and take up green fluorescent dye in the region irradiated by the laser, demonstrating that laser scanning is necessary for poration. Cell counting of this region indicates a delivery efficiency of 18% ± 4% from n = 3 data sets. This is 4.3 times less than the delivery efficiency observed for a nanocavity-*

structured surface coated with 50 nm of Ti, demonstrating that the nanocavities significantly improve delivery efficiency. b. The same cells fluoresce after incubation with viability indicator Calcein AM, indicating that these cells exhibit healthy metabolic activity and remain viable after laser scanning. Cell counting of the laser-scanned portion of the fluorescence image indicates a viability of 88% ± 4% from n = 3 data sets.

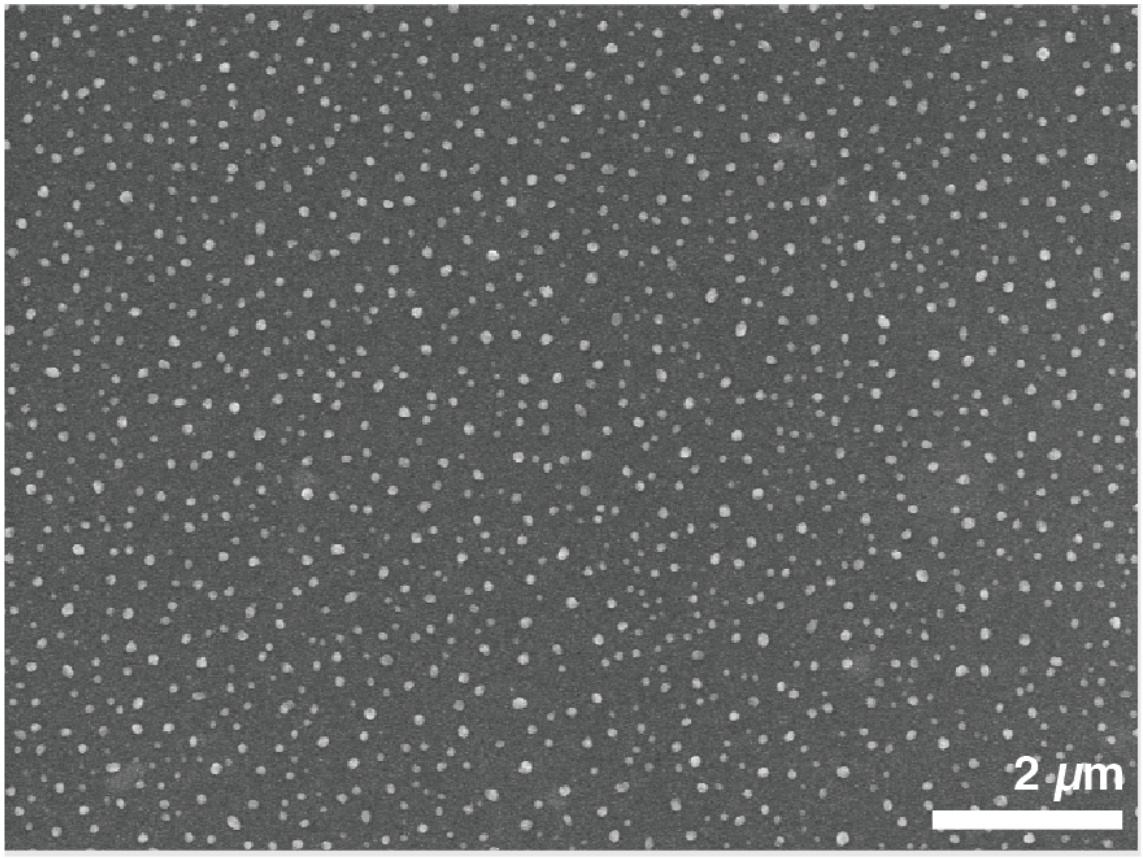

Figure 3.18: *SEM image of Ti evaporated onto unstructured glass coverslip. a. This sample was prepared by evaporating 50 nm of Ti onto a flat unstructured glass coverslip. Under the SEM we observe a surface roughness that likely mediates bubble formation, enabling low-efficiency intracellular delivery.*

Many membrane-impermeable cargoes of interest in biomedical research are orders of magnitude larger than the calcein green dye (0.6 kDa) used for our fundamental investigations. For instance, siRNA, a key component in gene therapy, has a molecular weight of ~13 kDa. [102] Proteins such as the CRISPR-Cas9 ribonucleoprotein complex, a powerful gene-editing tool, and antibodies, which are of interest for imaging, are ~150 kDa. To investigate the possibility of delivering high molecular weight compounds via our thermoplasmonic nanocavity array, we performed proof-of- concept experiments aiming to deliver fluorescently labeled dextran macromolecules (fluorescein isothiocyanate (FITC) dextrans), with molecular weights ranging from 70 to 2000 kDa, to HeLa CCL-2 cells. We used the optimal fluence of 12.6 mJ/cm^2, as determined by the calcein green delivery experiments. The same laser scanning system and laser scanning parameters used in the calcein green delivery experiments were used in the FITC-dextran delivery experiments. Figure 3.19a-d shows confocal fluorescence microscopy images of the cellular uptake of the different FITC-dextran polymers with molecular weights of 70, 150, 500, and 2000 kDaA. A fluorescence signal in the cell can be seen for all these molecular weights, indicating delivery of the cargo into to the cytoplasm of HeLa CCL-2 cells. Moreover, the 70 and 150 kDa FITC-dextrans appear to be delivered to the nuclei of the HeLa CCL-2 cells as well, as evidenced by the green fluorescence signal present throughout the entire region of the cell, including the nuclear region, in the confocal image slices. This is most likely due to the naturally-occurring nuclear pores. The intensity of the green fluorescence signal decreases for larger dextrans, indicating that the number of delivered molecules per cell decreases as the size of the delivered molecules increases. This is likely because the larger molecules diffuse more slowly, and therefore fewer molecules are able to diffuse into the cells before the pores in the cell membrane reseal. This inverse relation between delivery cargo size and the number of delivered

molecules per cell is in agreement with results from other thermoplasmonic-substrate-based intracellular delivery techniques. All cells that are successfully porated and encapsulated FITC-dextran also express a calcein AM signal, indicating they are viable after the experiment (Figure 4e–h). These proof-of-concept studies demonstrate the potential of the self-assembled thermoplasmonic nano- cavity substrates to deliver large membrane-impermeable cargo to HeLa CCL-2 cells while maintaining cell viability. The ability to deliver large cargoes is crucial for applications such as footprint-free gene editing and imaging of intracellular organelles. Although the development of laser-activated thermoplasmonic substrates recently enabled high-throughput, high-efficiency, and high-viability intracellular delivery of large cargoes, the nanocavity substrates introduced here are the first to utilize a simple, quick, and cost-effective self-assembly-based fabrication process without necessitating the use of expensive and sophisticated cleanroom equipment.

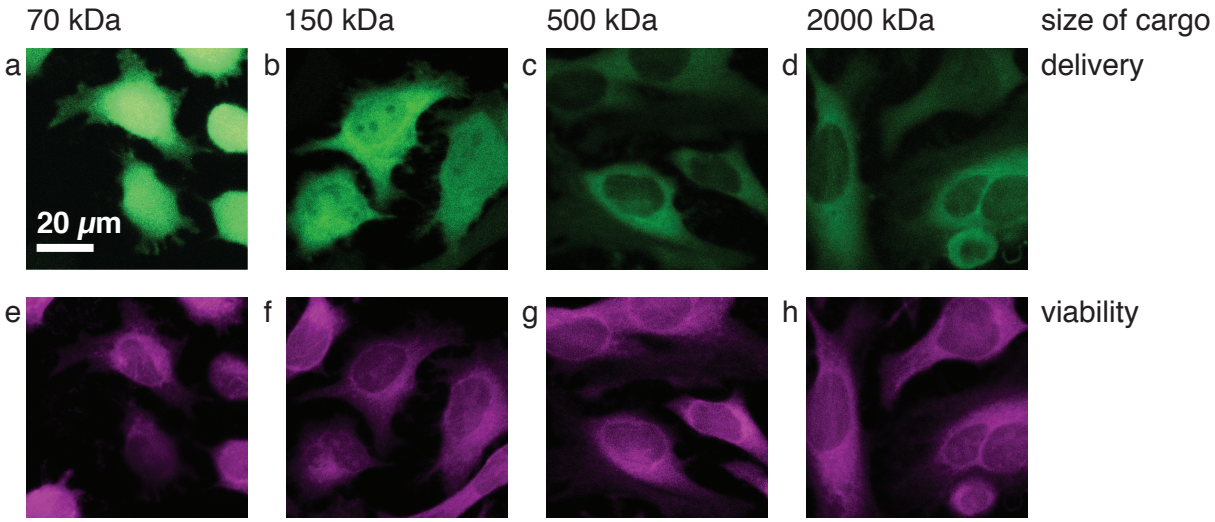

Figure 3.19: *Intracellular delivery of large cargoes using self-assembled thermoplasmonic nanocavity substrates. a-d. Confocal images of HeLa CCL-2 cells show green fluorescence, indicating delivery of FITC-dextrans (fluorescein isothiocyonate) ranging in size from 70 kDa to 2000 kDa. Cargoes of 150 kDa and smaller are delivered to both the cytoplasm and the nucleus,*

whereas cargos 500 kDa and above are delivered to only the cytoplasm. e-h. The same cells fluoresce after incubation with viability indicator Calcein AM, indicating that all cells that are porated and that enclose the target molecules also exhibit healthy metabolic activity and remain viable.

3.3.3 Discussion

In the previous section, we used nanofabricated pyramids with 2.4 μm baselengths and edge-to-edge spacings of 1.2 μm covered in a 50 nm thin layer of gold (Au) to deliver calcein green dye to HeLa CCL-2 cells. For the thermoplasmonic micropyramid substrates, we determined the optimal fluence to be 54 mJ/cm^2, which is ~5 times higher than the 12.6 mJ/cm^2 optimal fluence observed for the nanocavity substrates. The maximum calcein green delivery efficiency of 78% for the nanocavity substrates is slightly less than the 95% delivery efficiency measured for the micropyramid substrates. However, unlike with the micropyramid substrates, the fabrication process for the nanocavity substrates does not require the use of sophisticated and expensive cleanroom equipment. The same nanosecond-pulsed laser system and scanning parameters were used for both sets of experiments. The lower optimal fluence for the nanocavity substrates may indicate that the Ti- coated nanocavities are more efficient at absorbing and converting laser energy than the Au-coated micropyramids or may be due to the higher density of nanocavities on the patterned substrates compared to the micropyramids.

Laser-activated self-assembled thermoplasmonic nanocavity substrates offer a promising intracellular delivery platform. We show spatially selective delivery of membrane-impermeable calcein green into HeLa CCL-2 cells, at a delivery efficiency of 78% and a cell viability of 87%. Additionally, we show successful delivery for diverse cargoes, ranging in size from 0.6 to 2000 kDa. The optimal laser fluence for the self-assembled nanocavity substrates is a factor of 5 smaller

compared to similar thermoplasmonic substrates fabricated by nanofabrication. The spatially selective delivery enabled by these substrates opens the possibility of delivering cargoes to different cells or different regions of a tissue, which is important for generating complex tissues and studying interactions between subpopulations of cells. In addition, the nanocavity substrates can be activated using a nanosecond-pulsed laser system, which is less expensive, easier to operate, and more stable than the femtosecond and picosecond laser systems that are required for many plasmonic materials for intracellular delivery. The fabrication process is simple, quick, and cost-effective, making intracellular delivery experiments more accessible. The ability to efficiently deliver a range of membrane-impermeable cargoes into cells at high throughput while maintaining high cell viability, has the potential to advance the fields of biological and medical research by further enabling studies involving gene-editing, cellular engineering, imaging, and drug delivery.

3.4 Conclusions

In this chapter, four different substrates are discussed: gold upright pyramids, titanium nitride inverted pyramids, titanium nitride upright pyramids, and titanium nanocavities. All exhibit thermoplasmonic effects upon nanosecond pulsed laser excitation that are applied to spatially localized cargo delivery in a high-throughput protocol. Transient membrane pores are created and allow materials in the aqueous medium environment to diffuse into the cytoplasm before the phospholipid bilayer seals. The first three require cleanroom fabrication while the nanocavities do not need cleanroom tools.

Gold nanopyramid arrayed substrates created with a cost-effective method of large-area photolithography and template-stripping, a plasmonically optimized device which efficiently delivers cargoes ranging in size from 0.6 to 2000 kDa to cells with high viability (of up to 98%). The technique is also high-throughput, treating 50,000 cells per minute. There were minimal

residual fragments after laser-irradiation, unlike other plasmonic delivery methods using gold nanoparticles. Dense arrays of colloidal self-assembled nanocavities were thermally coated with 50 nm of titanium to create large macroscopic areas that can efficiently convert near-infrared laser light into heat. The substrate array geometry facilitates successful optoporation and cargo delivery. This colloidal substrate does not require cleanroom fabrication facilities that the gold nanopyramids do and is able to deliver the membrane-impermeable calcein green dye molecules into the cellular cytoplasm at an efficiency of 78% and at a throughput rate of 30,000 cells per minute. 87% of the cells survive treatment. All three substrate platforms are excited by 11-ns laser pulses of 1064 nm wavelength to create transient pores in cells. Adherent cell lines such as HeLa are grown on the substrates, and pores only form on the cells in the localized regions excited with nanosecond laser pulses—thus, allowing treatment selectivity within a population. The medium surrounding the cell contains the delivery cargo in solution, and cargoes diffuse into the cell before the transient pores are sealed. We use fluorescence imaging and flow cytometry to quantify the delivery efficiency and viability in a reproducible manner. Our light-activated substrate platforms can deliver important material directly into cells, furthering the field of nanomedicine in a cost-effective manner.

However, there are several limitations to the rigid-structured metal nanostructured substrate devices. One is that sensitive cell-lines, such as induce pluripotent stem cells and embryonic stem cells often cannot grow on metal substrates and cannot grow on materials that are so rigidly patterned. This may be remedied by using coatings such as fibronectin to promote cell growth, but this may decrease delivery rate. Another limitation to the samples is the restriction to 2-dimensional growth and thus, only adherent cells are used and treated with the methods covered

in this chapter. In the next two chapters, non-metallic polymer materials for cargo delivery to both adherent and suspension cell types are covered.

Chapter 4

Laser-Irradiated Polymer and Pressure Waves

This chapter has been adapted from the following publication:

Shen, W.; Kalies, S.; Madrid, M.; Heisterkamp, A.; Mazur, E. Intracellular Cargo Delivery Induced by Irradiating Polymer Substrates with Nanosecond-Pulsed Lasers. *ACS Biomater. Sci. Eng.* **2021**. https://doi.org/10.1021/acsbiomaterials.1c00656. [103]

4.1 Introduction

There is a great need in the biomedical field to efficiently, and cost-effectively, deliver membrane-impermeable molecules into the cellular cytoplasm. However, the cell membrane is a selectively permeable barrier and large molecules often cannot pass through the phospholipid bilayer. The work in this chapter show that nanosecond laser-activated polymer surfaces of commercial polyvinyl tape and black polystyrene Petri dishes can transiently permeabilize cells for high-throughput, diverse cargo delivery of sizes of up to 150 kDa. The polymer surfaces are biocompatible and support normal cell growth of adherent cells. The optimal irradiation conditions for poration, influx of fluorescent molecules into the cell, and post-treatment viability of the cells are determined. The simple and low-cost substrates used have no thin-metal structures, do not require cleanroom fabrication, and provide spatial selectivity and scalability for biomedical applications.

To advance basic research in medical biology and develop therapeutics, it is vital to understand and fix mechanisms at the cellular level[10] and manipulate biological functions through the delivery of molecular cargoes, such as proteins, antibodies, and genetic materials. [7,104] Proteins can be delivered into the cytosol to directly interfere with metabolic and signaling pathways of

cells. Genetic materials such as small interfering RNA can be deployed to manipulate gene expression. [105] With the development of CRISPR-cas9, gene-editing can be used for gene-therapy treatments, such as CCR5-knockdown for HIV treatments. [16,17,106–109] In the emerging field of nanomedicine, it is important to deliver biologically interesting cargo and molecules directly into cells. [9,11] However, direct delivery of such cargoes into the cellular cytoplasm is a challenge. [12,13] Existing intracellular delivery techniques, such as electroporation, viral transduction, and liposomal reagents, each come with strengths and weaknesses. While these methods may fit some application needs, they are hindered by problems such as toxicity, low efficiency, or low throughput. Another method, optotransfection, [56,110,111] provides high transfection efficiency, as well as high viability and selectivity, but has a very low throughput as it only transfects one cell at a time. In order to positively manipulate and fix diseases, a cargo delivery platform must be able to perform with high efficiency and throughput without sacrificing cell viability.

Nanotechnology and microfabrication have opened the door for the creation of devices on the scale of biological systems. [99] Many devices have been created for cargo-delivery, including devices that use squeezing as the physical mechanism, [47] microcapillary pipettes for microinjecting cargo, [112] microfluidic devices, [113] and plasmonic materials for cell poration. Plasmonic poration of cells has been demonstrated using metallic nanoparticles[114] and a variety of substrates made of titanium nitride, gold, and titanium, such as pyramidal arrays fabricated using photolithography and nanocavity structures fabricated using self-assembling colloids as described in the previous chapter. [21–23,68,115] However, metals used in nanophotothermolysis can fragment. [116] To avoid the risk of forming metallic fragmentation from thin-films and nanoparticles, it is important to explore other non-metallic thin-film materials. Non-metallic particles such as carbon nanoparticles[60] and polydopamine nanosensitizer particles[117] have been designed and synthesized for efficient cargo-

delivery and demonstrates that carbon particles and polymer particles can be used in place of metallic particles that have been traditionally used for targeted drug delivery. The development of non-metallic particles has also opened doors to non-metallic substrate systems as delivery devices.

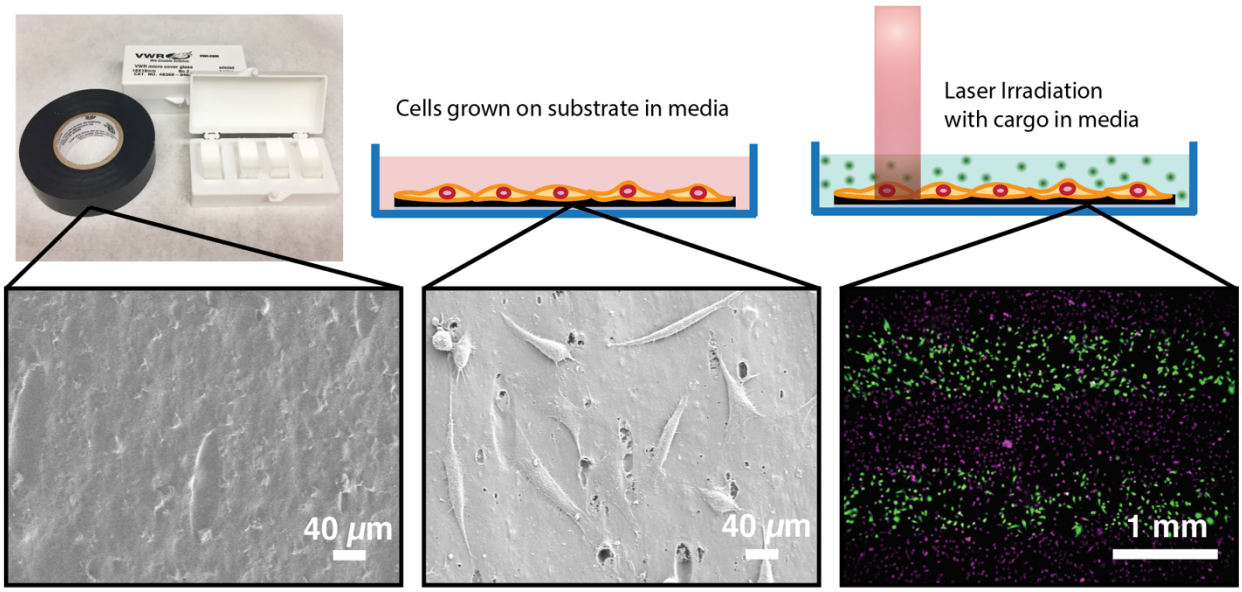

Figure 4.1: *Schematic of the method. The top left photo shows the off-the-shelf polyvinyl electrical tape and coverslips. The corresponding SEM images in the bottom left shows black tape and the bottom middle show HeLa cells chemically fixed on black tape. The bottom right image is an overlay of two fluorescence channels showing HeLa cells that have been loaded with calcein green with laser-irradiation and are alive, stained with calcein AM red-orange (altered to be magenta in the image), with the two laser-scan tracks.*

In this chapter, we demonstrate the use of polymer substrates for cell poration and cargo delivery. We use commercially available polyvinyl tape and black polystyrene Petri dishes to deliver fluorescent cargo to cells and measure the post-delivery viability of the cells, as shown in the schematic provided in Figure 1. The polymer substrates are nontoxic to cell lines and support

normal cell growth and adhesion for adherent cells. We use a near-infrared laser to minimize interference with biological processes in the cells. [118] By raster scanning the laser beam over the substrates, we are able to deliver cargo to cells at a rate of about 50,000 cells/min. We demonstrate delivery of fluorescent dye molecules, ranging from 648 Da to 40 kDa, to HeLa and Panc-1 adherent cell lines, and determined the optimal irradiation parameters for delivery of these molecules; for calcein green (648 Da), we achieve delivery efficiencies of up to 40% with viabilities of 60%. Our results demonstrate cargo delivery by nanosecond-pulsed laser irradiation of bulk, off-the-self polymer materials, obviating the need for nanofabrication and costly materials. The delivery system also is substrate-based as opposed to a free-flowing particle-activation system for delivery which may require specific chemical synthesis and functionalization.

4.2 Experimental Methods

4.2.1 Experimental protocol: cargo delivery

We use pigmented polyvinyl substrates on a glass coverslip, as shown in Figure 2a. Off-the-shelf polyvinyl Duck Brand Professional Electrical Tape of black color and white color are used and mounted on glass #2 coverslips, adhesive-side down, for rigidity. These substrates are placed in a 100-mm Petri dish for cell seeding. We grow adherent HeLa CCL-2 or Panc-1 cells on the substrates in a mixture of 10% fetal bovine serum medium, Dulbecco's modified eagle medium without phenol red, 1% L-Glutamine, and 1% penicillin streptomycin. The samples are incubated at 37°C and 5% CO_2 and passaged two to three times per week. The cells are used in experiments when they reach 80% confluence in flasks and before the 30th passage. Five million cells are seeded overnight in 15 mL of medium in a 100-mm Petri dish. After the cells are grown on the substrates, each seeded substrate is transferred from the media-filled 100-mm Petri dish to a 35-mm Petri dish with 2 mL of a phosphate buffered saline (PBS) solution. The solution contains the membrane-

impermeable fluorescent cargo of interest: Calcein green at 0.57 mg/mL or FITC-dextran (10, 20, 40, 70, and 150 kDa-sized) at 25 mg/mL. When the cell membrane is porated and the membrane-impermeable dye molecules diffuse into the cytoplasm before the pores close, the loaded cells are detected in the green fluorescence channel. Figure 2b shows HeLa cells that are chemically fixed on the polymer substrates, with a 5-nm thick coating of Pt/Pd to permit scanning electron microscopy. The cells adhere to the sample surface without any surface treatment.

The dish with the seeded samples is placed on an *xy* scanning stage to permit raster scanning the laser beam over a selected area of the sample. The system uses an 11-ns pulsed Nd:YAG (neodymium-doped yttrium aluminum garnet) laser with a repetition rate of 50 Hz, operating at a wavelength of 1064 nm, and is Q-switched and is turn key operated. The diameter of the laser beam spot on the substrate surface is approximately 1 mm and has a Gaussian beam profile. The energy output of the laser is varied using a built-in laser attenuator and a half-wave plate and polarizer combination, yielding an excitation fluence ranging from 30 to 130 mJ/cm^2 at the substrate surface. The scanning-stage raster scans the sample in the *x* and *y* directions, over a distance of 100 mm and 500 μm, respectively, at a speed of 10 mm/s. Given this speed, laser repetition rate, and laser beam spot size, each point in the scanned area is exposed to about six laser pulses.

To determine the viability of the cells post-treatment, we transfer the cell-covered substrate to a new 36-mm Petri dish, incubate them for 15 minutes in a solution containing 2 mL of Calcein AM red-orange (emission at 590 nm under 577-nm excitation), a viability indicator, and then rinse them twice in PBS. After acetoxymethyl ester hydrolysis of the Calcein AM red-orange by intracellular esterase, only cells with healthy metabolic activity express fluorescence in the red channel. Cells that express Calcein AM red-orange and the delivery cargo in the green channel

(emission at 515 nm under 495-nm excitation), are both alive and have the non-membrane permeable cargo delivered into the cytoplasm before the pores closed.

To quantify the treatment efficiency and viability for each experiment, we take two images of each area that has been irradiated: one in the green channel to determine efficiency of delivery and one in the red channel to determine viability. The images are overlaid and processed in ImageJ to count the number of cells in each channel in the selected area. Efficiency and viability are determined by dividing the number of green-emitting and red-emitting cells, respectively, by the number of red-emitting cells in an equally sized control area that was not irradiated. Each experiment is repeated three times to obtain standard error from three independent experiments.

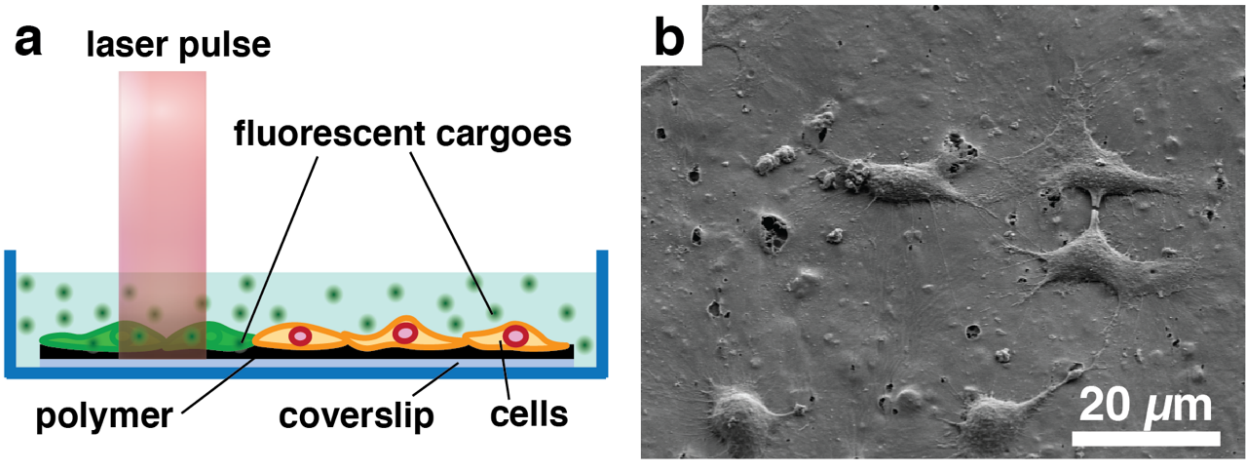

Figure 4.2: *(a) Schematic of polymer-based cargo delivery setup. Cells are seeded on a polymer substrate placed inside a Petri dish filled with a fluorescent cargo-containing medium. Laser energy absorbed by the polymer substrate causes transient pores in cellular membrane, allowing cargo to diffuse into the cells. (b) Scanning electron microscopy image of HeLa cells fixed on a carbon black-pigmented polyvinyl surface, showing cell adherence and material surface morphology.*

4.2.2 Experimental protocol: hydrophone measurements

A digitizing oscilloscope (Agilent Technologies MSO6104A mixed signal oscilloscope 1 GHz 4 GSa/s) was used to measure and store the data from the needle hydrophone. The pressure wave measurement was outputted by the oscilloscope as voltage over time. The measurements through the oscilloscope were triggered by the rise of the photodiode (ThorLabs DET110) signal from the first pulse of a train of six incoming laser pulse that excites the area. Figure 4.3 shows the schematic of the set-up. The Q-switched nanosecond laser was programmed to output six consecutive 11-ns pulses at 50 Hz. A photodiode was in proximity to the petri dish and captured signal from the laser pulses in order to trigger the oscilloscope to record immediately after the polyvinyl sample in DI water was excited by the laser.

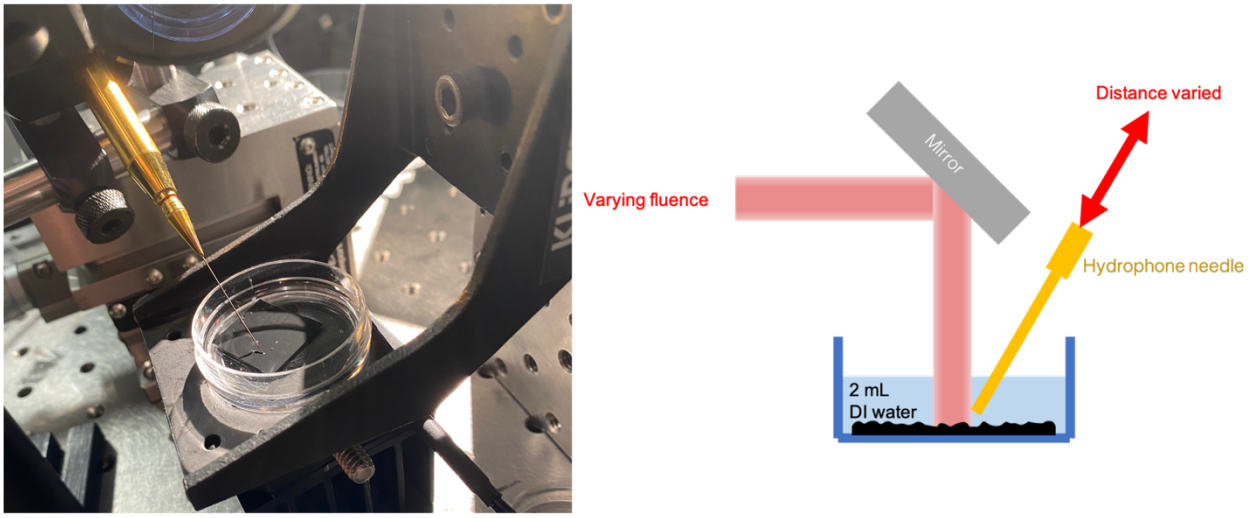

Figure 4.3: *(a) Photograph of (b) Cross-sectional schematic of the needle hydrophone set-up. The hydrophone needle comes at an angle of about 40 degrees relative to the horizontal plane of the black polyvinyl substrate sample. The measurements were done in a small 36 mm petri dish filled with 2 mL of deionized water. The distance of the hydrophone needle is varied using a micrometer it is clamped to.*

4.3 Results

4.3.1 Delivery to HeLa and Panc-1 cells

Figure 4.4 shows the fluence dependence of the Calcein-green delivery efficiency and post-treatment viability of HeLa CCL2 and Panc-1 cells grown on a black polyvinyl substrate. The post-treatment viability decreases with increasing fluence because the increased radiation causes the cells to lyse and so they can no longer hold the cargo inside. Although the delivery efficiency initially increases with increasing fluence, it is capped by the viability and therefore it decreases at high fluence. For both cell types, we obtain a maximum Calcein-green delivery efficiency of 40% and a viability of 60% at a fluence of 76 mJ/cm^2.

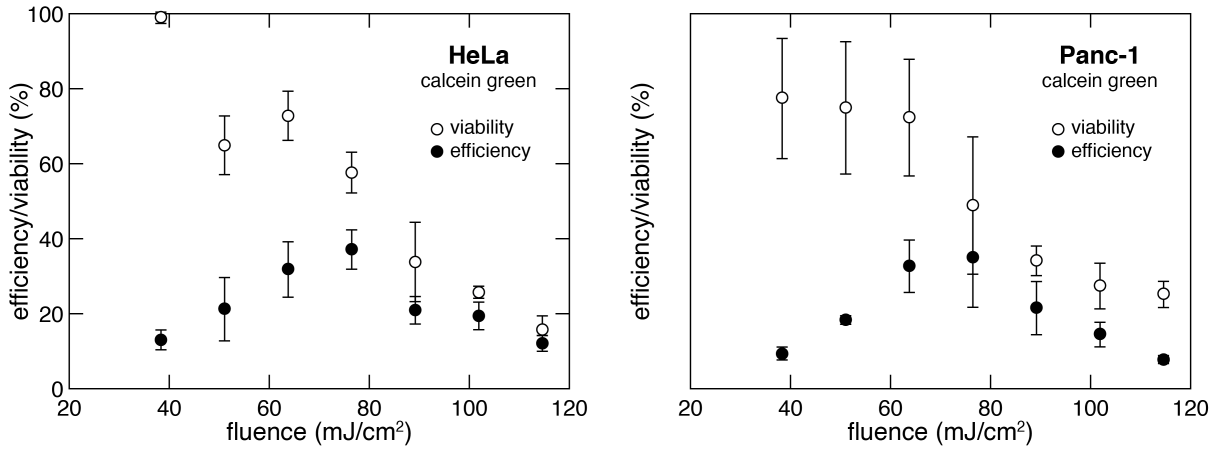

Figure 4.4: *Fluence-dependence of the viability (open circles) and delivery efficiency (closed circles) of calcein green delivery to (a) Panc-1 and (b) HeLa cells. Viability is defined as the number of cells that express calcein AM red-orange (a viability indicator) in a laser-scanned area divided by those in an equal-sized non-laser-scanned area. Efficiency is defined as the number of cells that show fluorescence in the green channel divided by the number of cells that express calcein AM red-orange in an equal-sized non-laser-scanned area. The mean efficiency and*

viability with corresponding error bars denoting standard error from n = 3 independent experiments are plotted.

To study the feasibility of larger cargo such we also studied the delivery of 10-, 20-, and 40-kDa FITC-dextran molecules to HeLa cells on a black polyvinyl sample. Figure 4.5 shows the green (left) and red (right) fluorescent images and integrated intensity profiles from the samples after irradiation, showing delivery and viability, respectively. The bright bands in the left images correspond to the regions where cargo was delivered to the cells; in each of the images, the top band was irradiated at a fluence of 89 mJ/cm^2 and the bottom one at 76 mJ/cm^2. The dark regions around these bands correspond to regions that were not irradiated and where no cargo was delivered to the cells. Note that the fluorescence intensity is higher at the higher irradiation fluence and that it decreases with increasing cargo size. The corresponding fluorescent images on the right show that there is little cell death at these fluences. Figure 4.6 provides a quantitative measurement, using flow cytometry, of delivery efficiency and viability for larger FITC-Dextran cargoes. We were able to achieve ~ 30% delivery efficiency for 10 and 20 kDa molecules, and ~20% for 40, 70, and 150 kDa molecules.

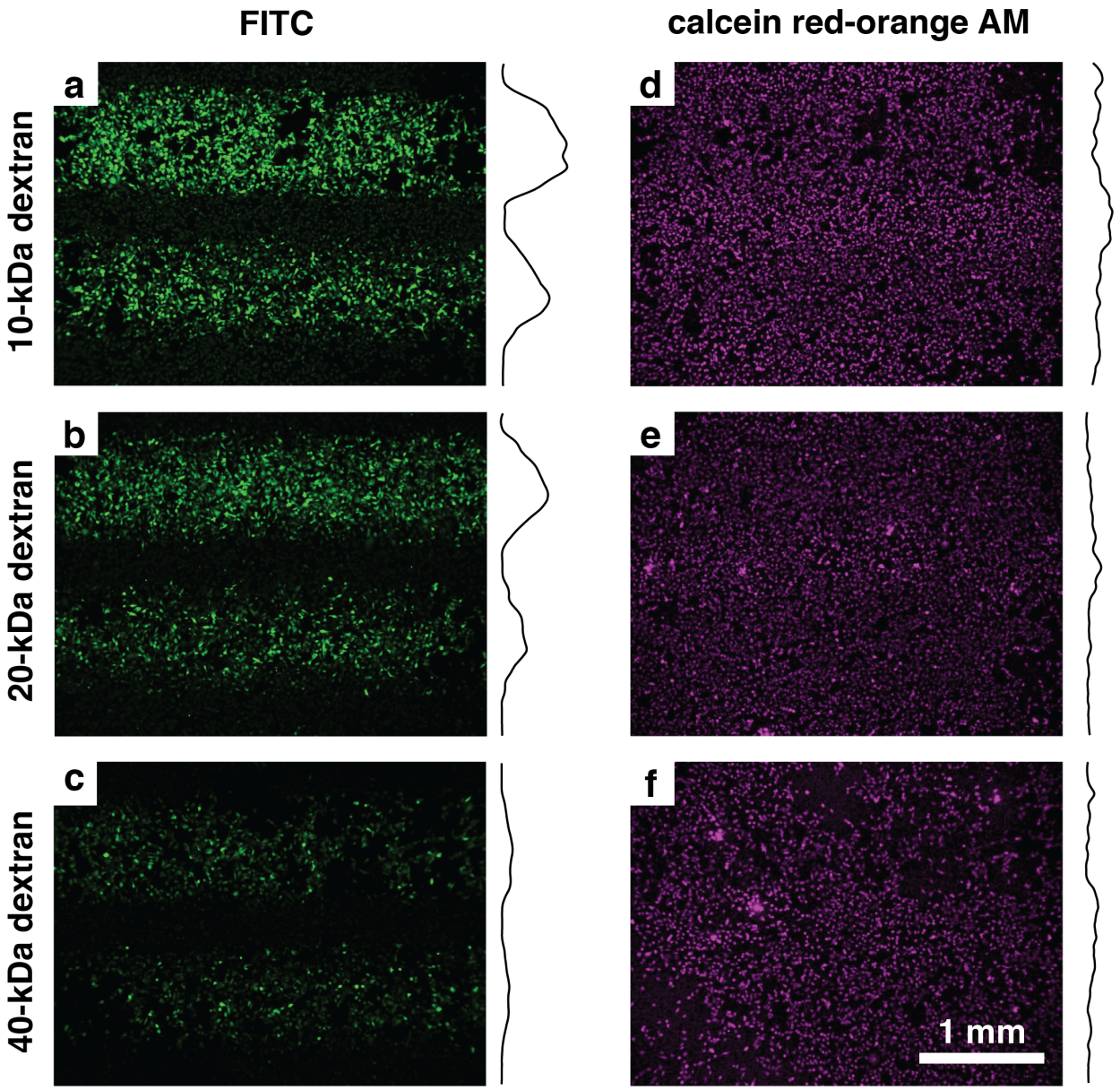

Figure 4.5: *Delivery efficiency and viability of delivery of dextran molecules of various molecular weights to HeLa cells using nanosecond laser irradiation of a black vinyl polymer surface. Expression of FITC-dextran of molecular weights (a) 10 kDa, (b) 20 kDa, (c) 40 kDa in HeLa cells. (d-e) Corresponding viability post-treatment with calcein AM red-orange (images altered to be magenta for color-differentiation clarity). The top strips in each image were exposed to a fluence of 89 mJ/cm2; the bottom strips to 76 mJ/cm2. The curves to the right of each image represent the horizontally-integrated intensity across the image.*

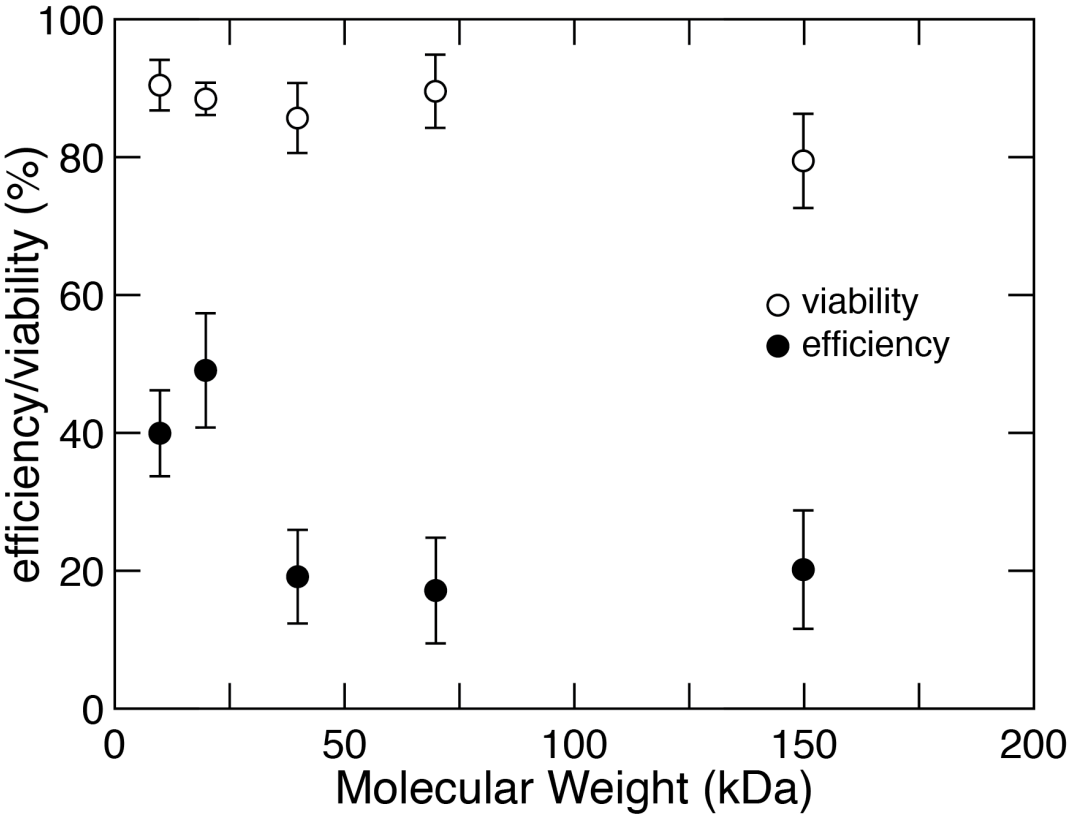

Figure 4.6: *Delivery efficiency and viability of differently sized FITC-dextran molecules using laser-irradiated black tape at 55 mJ/cm2, quantified by flow cytometry. Viability is obtained using propidium iodide to stain dead cells. The mean efficiency and viability with corresponding error bars denoting standard error from n = 3 independent experiments are plotted.*

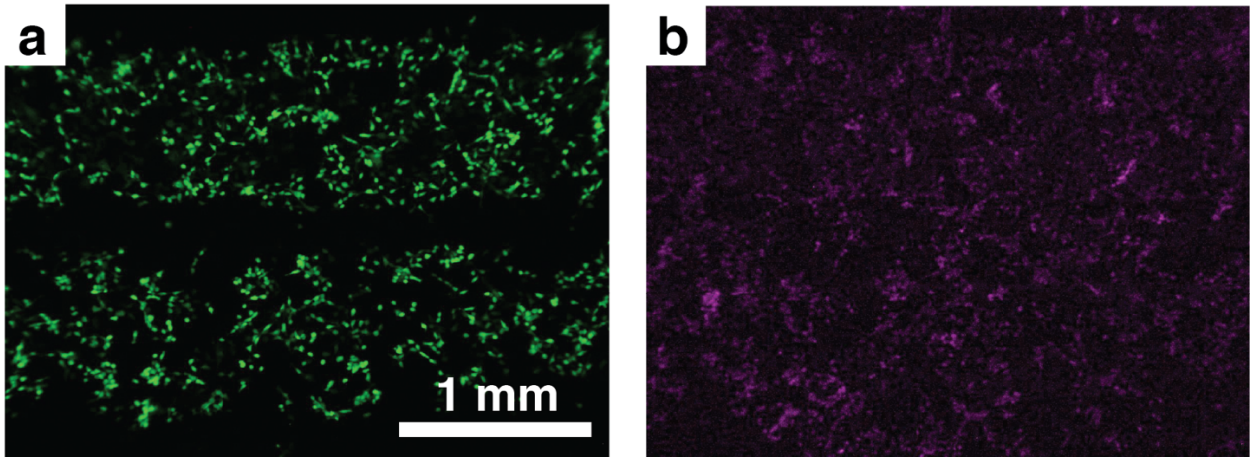

Figure 4.7: *(a) Delivery efficiency and (b) viability (altered to magenta for for color-differentiation clarity) of calcein green molecules to HeLa cells on laser-irradiated black polystyrene petri dish. The top strip area of the image was irradiated at used fluences of 140 mJ/cm^2 (top band) and 130 mJ/cm^2 (bottom band).*

We also investigated cargo delivery on black polystyrene (Figure 4.7) and white polyvinyl samples (Figure 4.8). Black polymers are pigmented with carbon black, whereas white polymers are pigmented with a metal oxide, such as titanium dioxide or zinc oxide. [119] We directly seeded HeLa cells on a black polystyrene Petri dish, while the white polyvinyl samples were placed in a regular Petri dish, seeded with HeLa cells. The white polyvinyl samples scatter the incident light, which causes a background signal in the images. As in Figure 4.5, the green fluorescence images show two bands, corresponding to the areas irradiated by the laser. For the white polyvinyl, we used fluences of 130 mJ/cm^2 (top band) and 120 mJ/cm^2 (bottom band). The images demonstrate that we also can deliver cargo to HeLa cells using white polyvinyl and black polystyrene. A higher range of laser fluence was used for the white polyvinyl than for the black polyvinyl, as lower laser fluence irradiation does not produce porated cells on the white polyvinyl substrates.

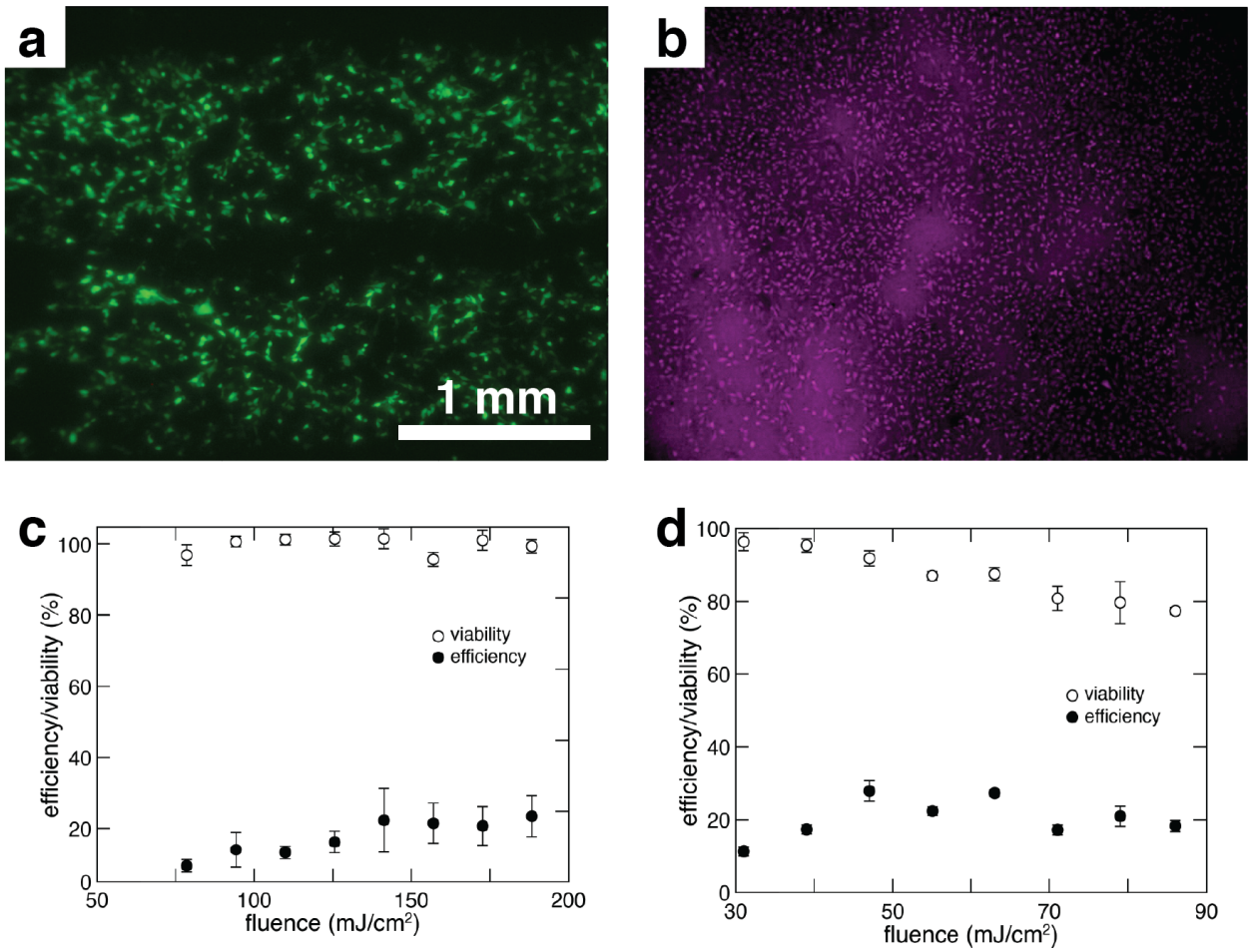

Figure 4.8: *a) HeLa cells with calcein green and (b) the same cells stained with a viability indicator, calcein AM red-orange (right; images altered to magenta for color-differentiation clarity). Measurement of delivery efficiency and viability of calcein green at varying laser fluences, quantified by flow cytometry. Viability is obtained using propidium iodide to stain dead cells. The mean efficiency and viability with corresponding error bars denoting standard error from n = 3 independent experiments are plotted for (c) white polyvinyl tape substrates and (d) black polyvinyl tape substrates.*

The polymer substrates vary greatly in optical absorption. Table 1 shows the spectrophotometer measurements of the white polyvinyl and black polyvinyl, indicating high

absorptance at 1064 nm for black polyvinyl and low absorptance at that wavelength for white polyvinyl and showing that delivery and absorption of energy are not correlated. Previous work, however, reports a relationship between impulse and laser-induced or shock-wave induced cargo delivery to cells. [45] To monitor any acoustic wave generated by the laser irradiation of the samples, we measured the pressure near the irradiated area, which will be covered in the next chapter. As one would expect, the amplitude of the pressure wave correlates with absorption. However, it does not correlate with cargo delivery, as we observe no pressure waves for white polyvinyl, which delivers cargo as efficiently as the black polyvinyl. It should finally be noted that we do not observe cargo delivery on clear polyvinyl tape, on a clear polystyrene Petri dish, or a clear glass coverslip, suggesting that pigments that interact with the laser wavelength are required for delivery.

	R	T	$A = 1 - R - T$
white tape	0.628	0.385	0.013
black tape	0.043	–	0.957
black Petri dish	0.054	–0.001	0.947

Table 1: *Spectrophotometer measurements of the white polyvinyl tape, black polyvinyl tape, and black polystyrene Petri dish at 1064 nm wavelength. The reflectance and transmission are measured directly from the samples, and the absorption is calculated and obtained as 1 minus the reflection and transmission. No transmission is measured from the black tape.*

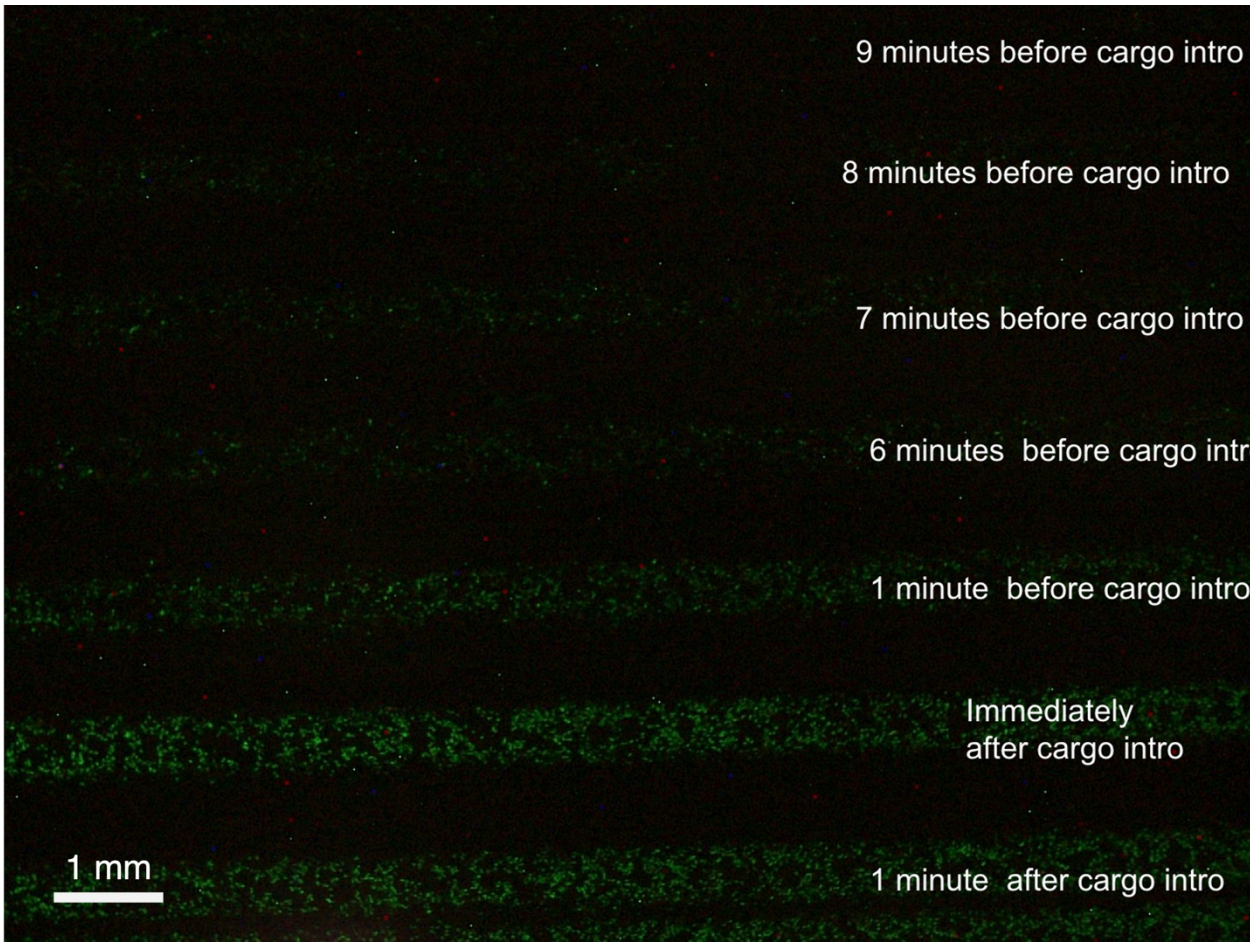

Figure 4.9: *Fluorescence image of calcein green in HeLa cells growing on black polyvinyl surface. Multiple horizontal scans of laser-irradiation were made before adding calcein green to the petri dish. The last scan at the bottom was made one minute after the cargo was introduced.*

By introducing cargo into the PBS medium after laser scanning, we can observe the time frame at which cargo enters into the cytoplasm, thus giving us an estimation of how the cell membrane is sealed completely. As shown in Figure 4.9 the brightness of the cargo in the cells that have been delivered to after cargo introduction decreases with increase in relative time before cargo introduction. There is still some brightness in the cells at the 8th minute before cargo introduction, where there is mostly none left by the 9th minute. This implies that it takes up to 9

minutes for cells to completely heal and for the pores to seal, preventing calcein green intake. This time frame is much longer than shown with the gold pyramids in Chapter 3. However, this image analysis is for a much larger number of cells and is analyzed quantitatively whereas the fluorescence change observation for the analysis done in Chapter 3 is just for one cell.

4.3.2 Delivery to human aortic valve interstitial cells and delivery of siRNA to HeLa

The laser-irradiated black tape can also support primary cell growth, as demonstrated in Figure 4.10. Calcein green and Dextran 10 kDa were delivered to primary human aortic valve interstitial cells. We were also able to deliver FAM-labeled Negative Control No. 1 siRNA (Silencer™ from Invitrogen) to HeLa cells at a rate of 9.2% with the black polyvinyl tape, as shown in the flow cytometry measurements in Figure 4.11. This is much lower than the 40% delivery efficiency we were able to achieve with the FITC-Dextran 10 kDa molecules. This may be due to the lower concentration of the siRNA molecules in the media during irradiation.

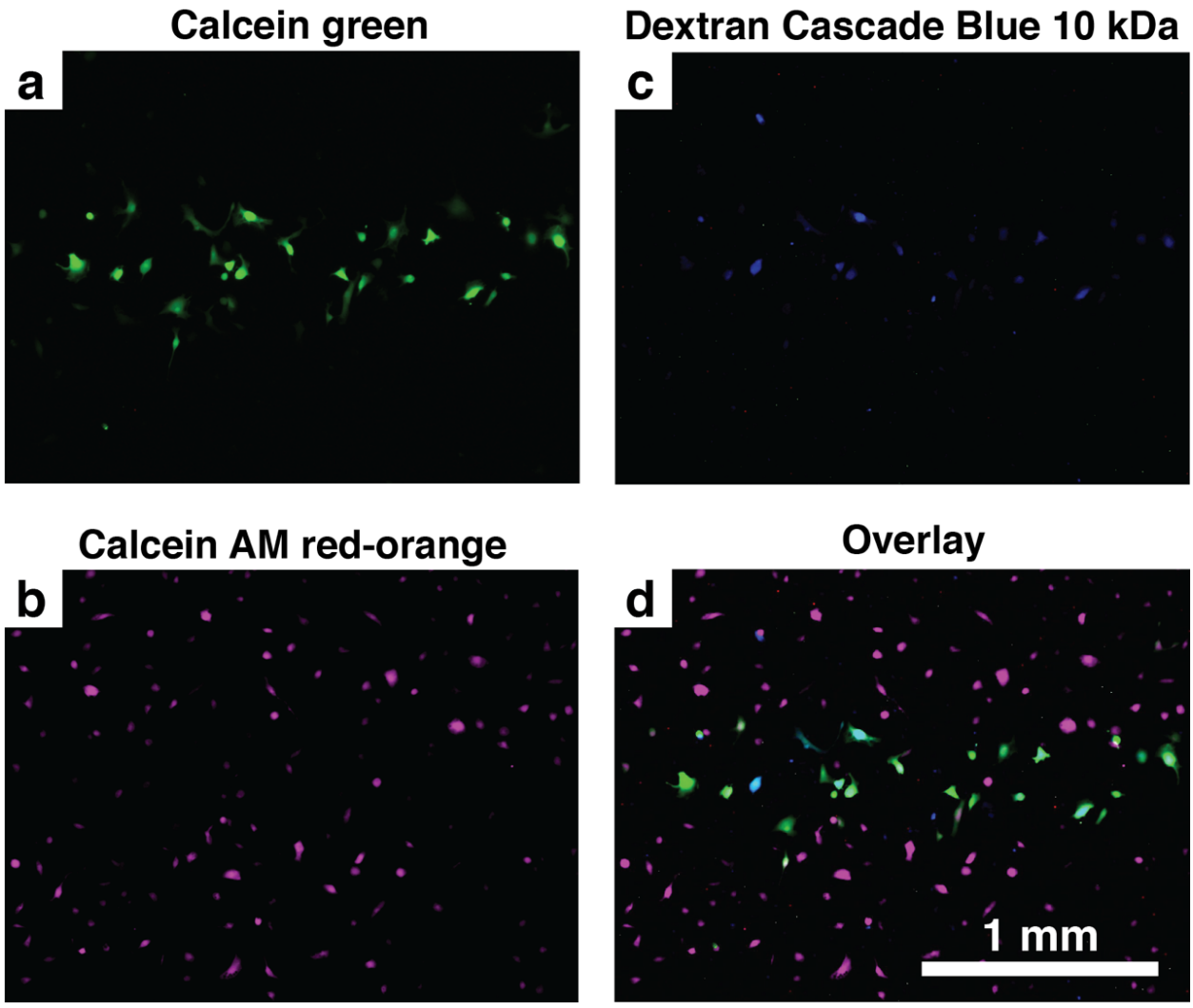

Figure 4.10: *Delivery efficiency of (a) calcein green and (b) Dextran 10kDa (Invitrogen™ Dextran, Cascade Blue) to primary human aortic valve interstitial cells and (c) corresponding viability (altered to magenta for for color-differentiation clarity). (d) overlay of the three images. The primary cells were provided by the Aikawa Lab at Brigham and Women's Hospital.*

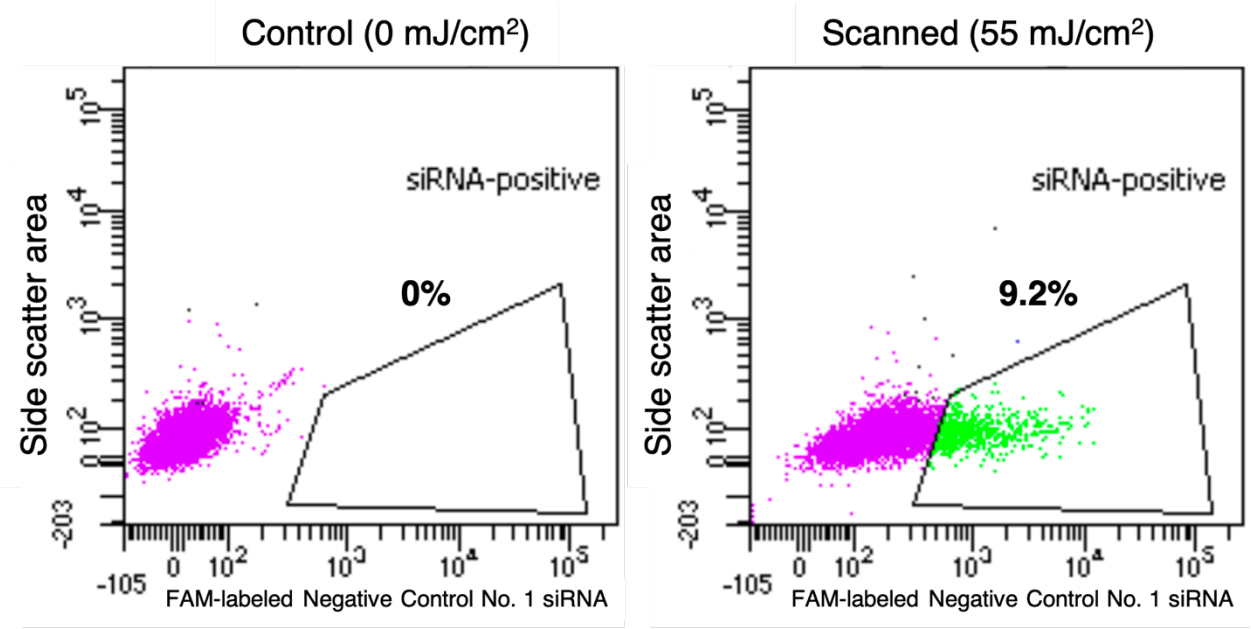

Figure 4.11: *Flow cytometry plot of the delivery efficiency of FAM-labeled Negative Control No. 1 siRNA to HeLa cells on black tape. Cell laser-irradiation was done when the substrates were submerged in a 16 µM solution of the siRNA.*

4.3.3 Surface morphology and pressure wave measurements

In order to understand the physical effects of the laser-irradiated polyvinyl tape surface, its effects on surface morphology, physical perturbations created in liquid, and its effects on cell poration and viability, we studied the surface roughness using scanning electron microscopy but as Figure 4.12 show a lack of obvious difference between unscanned and scanned substrates, optical profilometery was used to gain a quantitative understanding how the surface roughness changes with increasing laser fluence for the black polyvinyl tape and how the surface roughness does not change at all in relation to laser fluence for white polyvinyl tape.

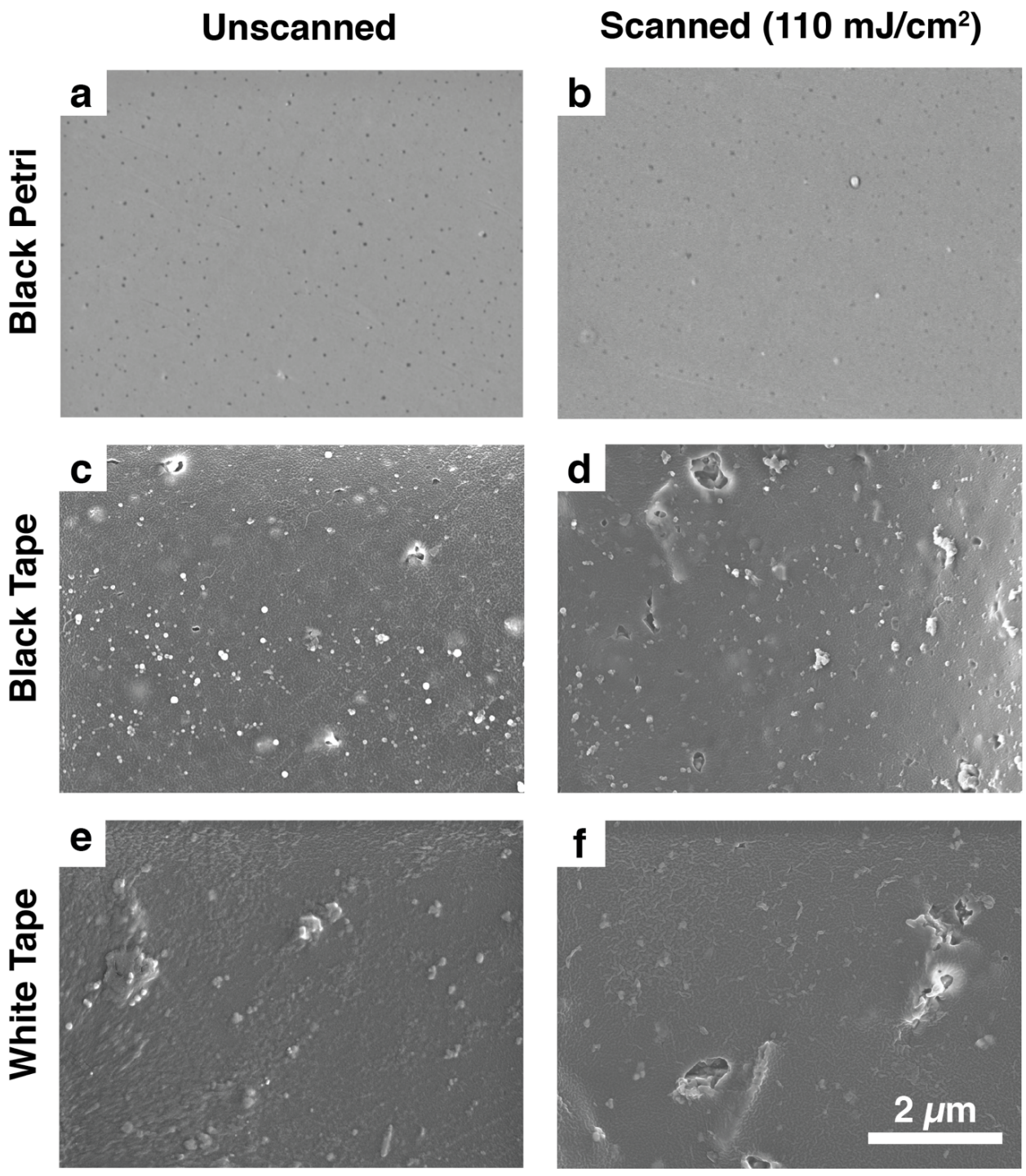

Figure 4.12: *Scanning Electron Microscopy images (using the InLens detector) of Black Petri dishes when (a) not laser-irradiated and (b) irradiated, black tape when (c) not laser-irradiated and (d) irradiated, white tape when (e) laser-irradiated and (f) irradiated.*

From the optical profilometer measurements, we define roughness as the root mean square height, which is calculated as:

$$Sq = \sqrt{\frac{1}{A}\iint_A Z^2(x,y)dxdy} \quad (eq.1)$$

With Z being the height at any given point, x and y being the 2-dimensional location of the point, and A being the area of interest (each of the three different areas were 800 x 800 μm). The right plot in Figure 4.13 shows that the surface roughness does not change for white polyvinyl tape. However, as seen on the left plot in Figure 4.13, the surface roughness of black polyvinyl tape changes with increasing fluence. Interestingly enough, the surface roughness starts to change around 65 mJ/cm^2 which is around the fluence where we see a plateau of pressure wave impulse magnitude as plotted in Figure 4.14. This fluence is also where we begin to see a decrease in cell viability.

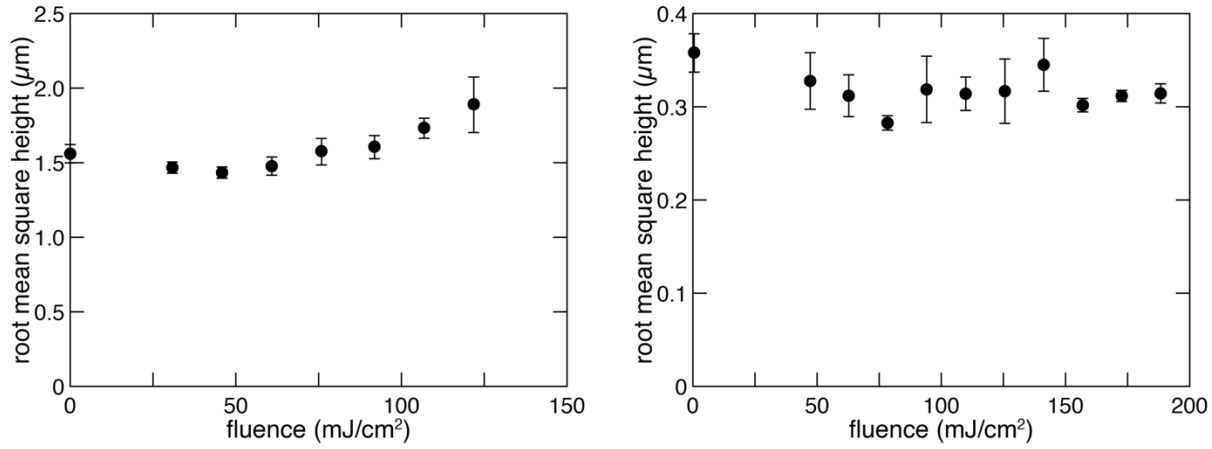

Figure 4.13: *(left) Optical profilometer measurements of the surface roughness (root mean square height is the same as standard deviation of heights) of the black polyvinyl surfaces after being exposed to lasers of varying fluences. (right) Optical profilometer measurements of the surface roughness (root mean square height is the same as standard deviation of heights) of the white polyvinyl surfaces after being exposed to lasers of varying fluences. Each measurement is repeated in three different areas, with the same laser-irradiation fluence to obtain standard error as denoted by the error bars.*

To monitor any acoustic wave generated by the laser irradiation of the samples, we measured the pressure near the irradiated area using a polyvinylidene fluoride needle hydrophone with a 0.04-mm diameter element with a sensitivity of 6 nV/Pa. The needle is positioned at about 45° approximately 0.5 mm from the laser spot on the sample. Needle hydrophone measurements of pressure waves were done for multiple fluences for three different relative needle hydrophone distances: 0.127 mm, 0.381 mm, and 0.635 mm. The stress-wave propagation was detected by the needle tip, which were read as voltage magnitude over time by the oscilloscope. For all three distances, we see that the impulse magnitude is plateauing around 70 mJ/cm^2. This fluence range

is also the maxima in the delivery and viability post-treatment rates from Figure 2. The impulse magnitude changing from the initial linear relation to fluence suggests that the surface is starting to deform at higher laser fluence excitation. The fluence range for higher pressure wave and subsequent deformation is the same for lower viability for cells.

The six voltage signals created in the water, from the six pulses, were averaged on the oscilloscope. These voltage versus time measurement outputs were then analyzed on MATLAB. The pressure conversion was 6 mV = 1 MPa, and the impulse were calculated from taking the integral of pressure over time while calibrating for the baseline noise voltage. This was then plotted, as shown in Figure 11 with error bars denoting the experimental uncertainty for each point, explained below. Figure 12 shows the impulse vs. fluence plot (for one distance, about 0.3 mm away from the source) for the black Petri dish, which is on the same order of magnitude as the black polyvinyl tape. The error accounts for the peak-to-peak noise being averaged over the six laser pulse shots and uses the 4-mV error the oscilloscope creates for the voltage uncertainty. No pressure waves were detected from laser-irradiated white polyvinyl tape, so the impulse cannot be calculated and plotted.

The MATLAB in the appendix was used for a folder containing an individual .csv file for each variation in fluence and variation in needle distance. The voltage vs. time is plotted for each experimental condition. Then, the voltage is converted to units of pressure, according to the needle hydrophone manufacturer. The data is also calibrated (ds.floor) according to the average of the first 100 data points of the set, where there is no event and only noise. After the calibration is made, the peak highest-pressure data point is found in the set. Then, the integration boundaries are set as the two points before and after this peak point. These two points are where the pressure is only 10% of the peak point, thus identifying and extracting the peak shape from each data set for

the integration of pressure over time, arriving at a calculation of impulse. Then, this calculated impulse is plotted with respect to other measurements with different fluences but same needle hydrophone distance.

In order to find the experimental error, the following calculations were made and incorporated in the code and subsequent scatter plot figure. To find the experimental uncertainty for the impulse plot in Figure 6b, the experimental uncertainty for pressure must be found first, as impulse is an integral of pressure over time:

$$I = \int P dt \; (eq. 2)$$

$$\sigma_P = \sqrt{\left(\frac{\partial P}{\partial V}\sigma_V\right)^2} \; (eq. 3)$$

The experimental uncertainty for voltage, σ_V, is found from the oscilloscope model manual (in this case, the uncertainty is 4 mV). The experimental uncertainty for impulse depends on pressure, as it does for the peak-to-peak noise of the oscilloscope measurements. Since, the measurements were averaged over 6 measurements (due to 6 shots of laser excitation for each measurement, to mimic the 6-shot count of the cellular experiments), we divide the uncertainty for voltage by the square root of 6:

$$\sigma_I = \sqrt{\left(\frac{\partial I}{\partial V}\frac{\sigma_V}{\sqrt{6}}\right)^2} \; (eq. 4)$$

The partial of impulse with respect to voltage uses the integral from equation (1), remembering the conversion of 6 mV = 1 MPa:

$$\frac{\partial I}{\partial V} = \frac{\partial}{\partial V}\int P dt = \int P\frac{dt}{dV} + dt\frac{dP}{dV} = \int_{t_0}^{t_1}\frac{\partial P}{\partial V}dt = \int_{t_0}^{t_1}\frac{1}{6}\frac{MPa}{mV}dt \; (eq.5)$$

Thus, we arrive at the experimental uncertainty of impulse for each data point to be:

$$\sigma_I = \sqrt{\left(\int_{t_0}^{t_1}\frac{1}{6}\frac{MPa}{mV}dt \cdot \frac{4\,mV}{\sqrt{6}}\right)^2} = \sqrt{\left(\int_{t_0}^{t_1}\frac{4}{6\sqrt{6}}\frac{MPa}{mV}dt\right)^2} \; (eq.6)$$

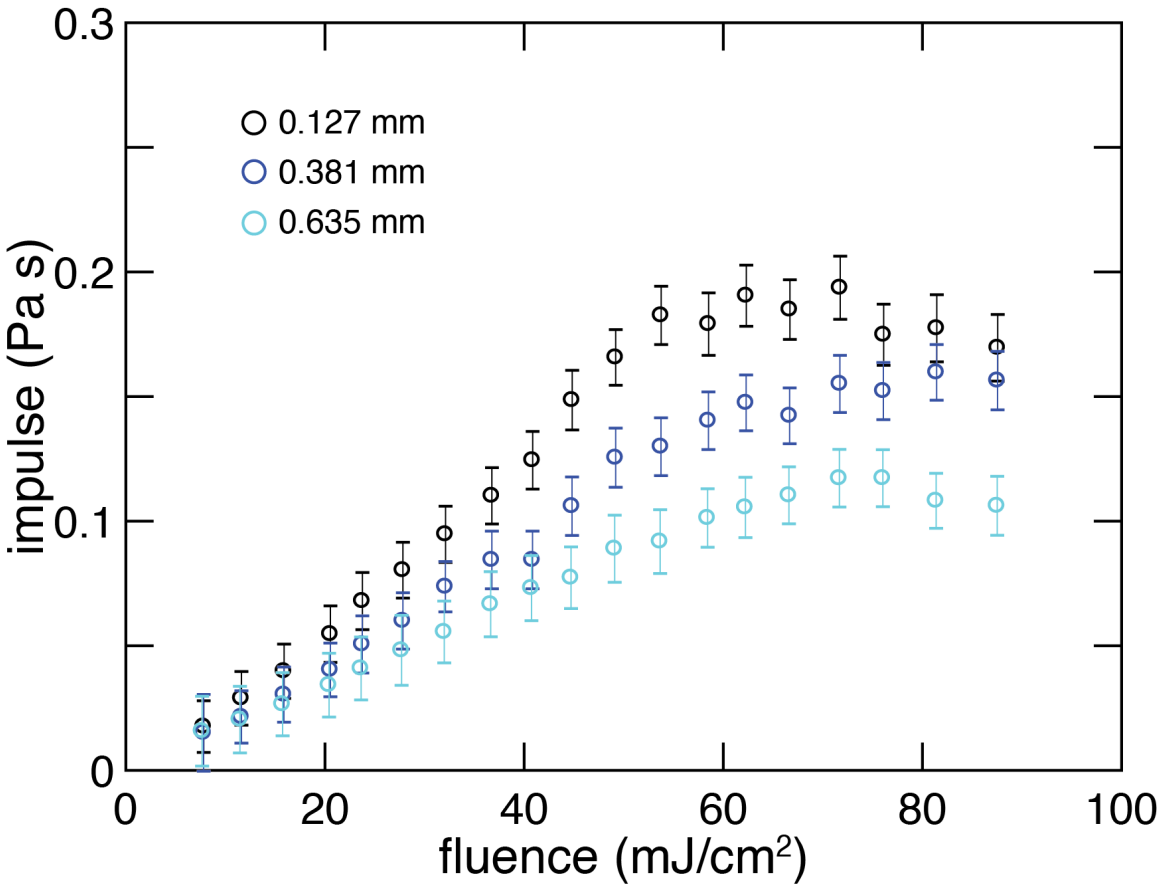

Figure 4.14: *The magnitude of the localized pressure wave impulse created by the laser-irradiated polyvinyl is plotted with respect to fluence. The differently colored curves represent the relative distance between the source of laser-irradiation and the top of the hydrophone needle.*

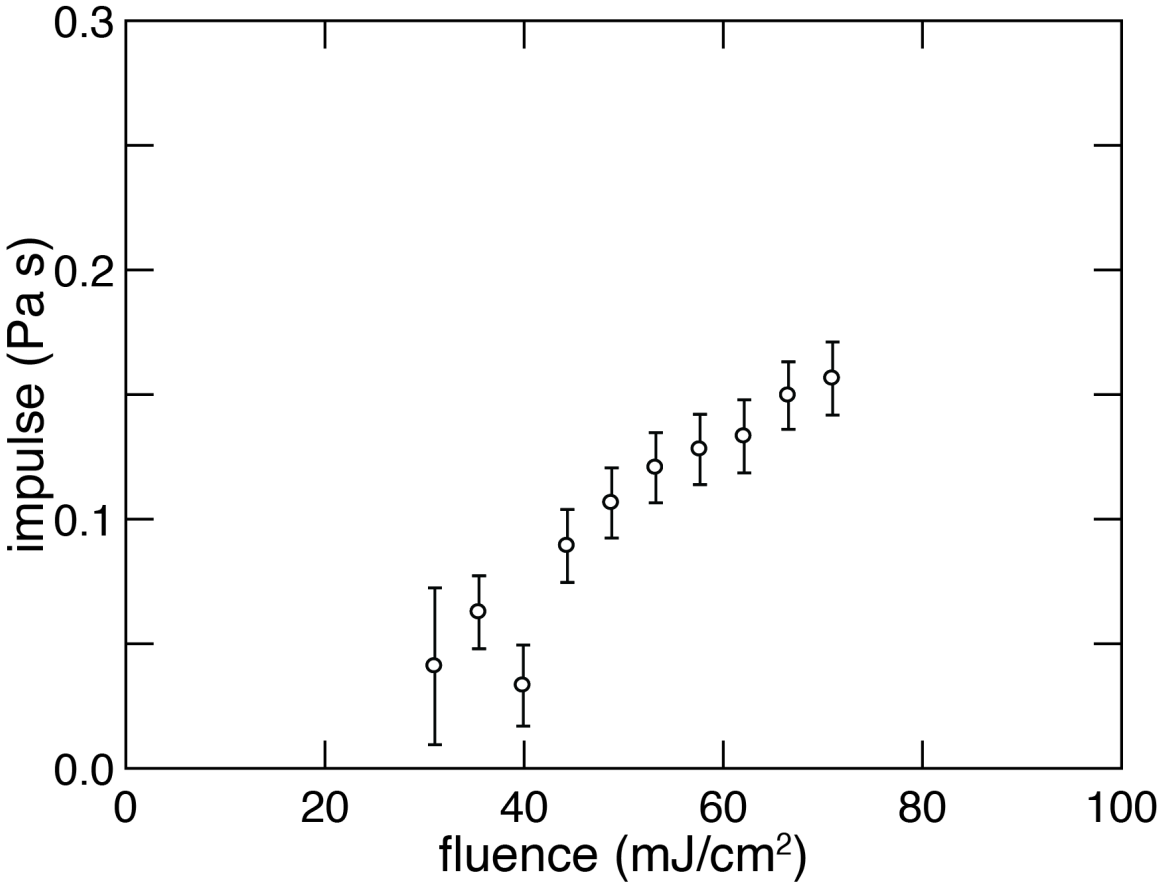

Figure 4.15: *The magnitude of the localized pressure wave impulse created by the laser-irradiated black polystyrene Petri dish is plotted with respect to fluence.*

4.4 Conclusions

Our results conclusively show that we can deliver cargo to cells using a variety of polymer surfaces. We demonstrate delivery of cargo up to 40 kDa, which is on the scale of siRNA, and obtain efficiencies and viabilities approaching those obtained with nanofabricated gold pyramids[22], titanium-nitride inverse pyramids[68], and self-assembled titanium nanocavities[67] which were also irradiated with the same pulsed-laser wavelength and parameters as discussed in the previous chapter. The viability at maximum efficiency we obtain for the delivery of calcein green to HeLa

cells on off-the-shelf polymer substrates (60%) is somewhat lower than the viability obtained for the metallic nanostructured substrates (87–98%) and requires a higher laser fluence (7.5 mJ/cm^2 vs. 1–5 mJ/cm^2). Similarly, the maximum efficiency on the polymer substrates (40%) is lower than that for metallic nanostructured substrates (78–95%), but part of this decrease in efficiency is due to the lower viability.

While it may be possible to improve the efficiency by optimizing the surface morphology of the polymer substrates, it is worth pointing out that polymer substrates are cheap and simple, flexible, and easily integrated into microfluidic devices. Unlike the nanostructured substrates, they involve no metals and do not require nanofabrication or clean-room handling. However, polymer structures may be combined with metals such as gold to fabricate a controlled heating substrate for efficient cargo delivery of around 90% in the kDa-sized range.[120] Dynamic photothermal polymers have also been synthesized and functionalized to harness localized heating to perform transfection of 100kDa-sized genetic materials at around 85% efficiency,[121] further motivating the direction of not relying on thin-film metal structures for efficient cell-membrane poration and to lower the cost of device production.

Laser-irradiated delivery of cargo to cells relies on diffusion through transient pores that are formed in the cell membrane during laser irradiation. [56] The larger the cargo, the lower the probability that it will enter the cellular cytoplasm via the transient pore before the pore self-heals. Indeed, the deliver efficiency decreases with cargo size, both for the polymer substrates and for the nanofabricated gold pyramids[22].

All previous work on cargo delivery with laser-irradiated metallic substrates involves nanostructured surfaces. The polymer substrates, however, have a very different surface morphology from the nanostructured substrates. Scanning electron microscopy reveals random

structures over a range of sizes while profilometry shows that the surface roughness is around 1 μm. The surface roughness increases slightly after irradiation with fluences for which the viability decreases. In the scope of pulsed-laser irradiated substrate-based platforms, between the polymer substrates and metallic substrates and particles from previous literature, there appears to be no correlation between surface features and poration.

Polyvinyl chloride begins to deform around 170 to 180°C[122], which suggests the black polyvinyl tape substrates to reach those temperatures at high laser-fluence irradiation. However, the surface roughness does not change even at higher fluences for the white polyvinyl substrate, further pointing at little energy absorption. The lack of pressure wave measured from irradiated white polyvinyl and the low absorption at 1064 nm in the spectrophotometer point to the absence of a high temperature rise for the poration method. High absorbent and low absorbent substrate both cause cargo-delivery upon laser-irradiation. The higher viability attained in the flow cytometry measurements for the white polyvinyl tape compared to the black polyvinyl tape suggests laser-irradiating inert metal oxides may prevent post-treatment cell death. The laser-material interaction between nanosecond pulsed laser and metal oxides, such as Titanium Dioxide, may be further explored in the future. Beyond impulse- and heat-driven cell poration methods, there are chemical or localized charging effects that may cause cell poration.[26]

We demonstrated direct intracellular cargo delivery using simple, off-the-shelf polymer substrates and a turn-key pulsed laser, which permits spatially selective cargo delivery within a population of cells. Even without optimization of the substrates, the delivery method with absorbent black polyvinyl surfaces is effective for cargo up to 150 kDa in mass, opening the door to the delivery of small genetic molecules using very simple and inexpensive means. The spatial selectivity of the method allows *in situ* control experiments in a single Petri dish, with cargo

delivered only to selected regions in the dish. The simple method also opens the door for a more sophisticated design incorporating inert oxides such as Titanium Dioxide and for further investigation on the controlled perturbation of the cell membrane.

Because polymers are readily molded into scaffolds, the technique we present can support direct intracellular cargo delivery for different biological and biomedical applications such as microcuvette chambers for suspension cell types which is covered in the next chapter. Some polymers, such as bioplastics using agarose or chitosan, are both biocompatible and biodegradable. These polymers could be combined with pulsed-laser systems to create potential *in vitro* cell treatments. The combination of biocompatible — and possibly biodegradable — polymers and pulsed-laser excitation creates a simple and versatile intracellular delivery platform that paves the way for new research and treatments in cell biology and medicine.

Chapter 5

Particle-Embedded PDMS Materials

This chapter has been adapted from the following publication in preparation:

Shen, W.; Chen, A.; Black, N.; Weitz, D.; Mazur, E. siRNA delivery with laser-irradiated PDMS microcuvettes embedded with carbon black. *[pub. pending]*

5.1 Introduction

The previous chapter has shown that upon nanosecond pulsed laser irradiation, polymer that is absorbent of the laser produces pressure waves at magnitudes appropriate for targeted drug delivery.[45] The proof-of-concept of the polyvinyl tape substrate experiments leads to the development of a simple material of PDMS (polydimethylsiloxane) being embedded, or mixed, with carbon and carbon black nanoparticles which are in abundance and has been used as nanoparticle suspension in media for laser-mediated drug delivery.[60,123] Outside of cargo delivery, PDMS has also been integrated with gold nanostructures for the application of enhanced ultrasound imaging.[124] PDMS has also been blacked with carbon black to create platforms to reduce background fluorescence for imaging.[125] It can also be used to create nanoneedle arrays for drug delivery.[126] PDMS is a thermosetting polymer, which are cured upon exposure to the appropriate amount of heat, radiation, pressure, or mixing with a catalyst. Unlike polymers with individual linear polymer chains, PDMS is made up with polymer chains that cross link and is often used for soft lithography fabrication methods which this chapter covers. PDMS is the most widely used silicon-based organic polymer.[127] Embedding PDMS with nanoparticles instead of having nanoparticles be free-flowing in a liquid media can also decrease the chances of nanoparticles remaining on or inside cells after treatment.

The integration of PDMS also allows for applications in microfluidic lab-on-chip experiments that can scale up treatment, study cell properties, and lower the liquid volume of experiments.[128] The use of a microfluidic platform also allows for other manipulation of cells outside of using laser-enabled heating, namely: squeezing where the deformation of cell membranes can be amplified by deformation in cell shape.[48,49,129,130] This chapter will discuss two applications of PDMS embedded with carbon black: (1) as a substrate material for spatially localized concurrent delivery of multiple cargo to different populations of adherent cells in a petri dish and (2) as a microcuvette that can lower the liquid volume of the experiment and expand the cargo delivery treatment to suspension cells, which is an important category of cells that blood and immune cells fall under.

5.2 Experimental Methods

The experimental methods section will first cover the simple protocol for embedding carbon black into PDMS. The subsequent section will use the embedded PDMS in the integration of the microcuvette chamber fabrication for the treatment of suspension cells. The third and final section of the experimental methods section will briefly cover the importance of suspension cells for immunotherapy and the cell culture protocols used.

5.2.1 Particle-embedding in PDMS

PDMS elastomers are commonly used for soft lithography fabrications. Soft lithography allows for the precise replication of microstructures required for microfluidic and micron-sized engineering applications.[131] While particles are often coated with polymer and lipids for higher biocompatibility and polymer nanoparticles have been synthesized and applied for cargo delivery, the method for the embedding of carbon black in PDMS is simple and creates bulk materials rather than nanoscale materials.[8,18]

Dow Corning Sylgard PDMS is used throughout the experiments in this chapter. The transparent PDMS is prepared by mixing the elastomer base with the accompany curing catalyst agent at a mass ratio of 10:1. It is mixed in a Thinky model ARE-250 mixer at a speed of 2000 rpm for 5 minutes. After the base and catalyst have combined, carbon black nanoparticles averaging 42 nm in size (Strem Chemicals, acetylene carbon black 50% compressed) is added at varying mass percentages (2% or 5%; adding more than 5% mass of carbon black causes the viscosity of the PDMS greatly and makes pouring difficult) before mixed again at a speed of 2000 rpm for 5 minutes. This carbon black-PDMS mixture is then poured into a container with a flat base, such as a wide 100 mm x 20 mm petri dish so a thin layer (<1 mm) is created. It is then degassed in a vacuum chamber for 15 minutes and transferred into a 65°C oven for 5 hours to be cured. Finally, the surface of the thin carbon black-PDMS layer is plasma treated (Gala Instrumente Plasma Prep 2) at 80 W for 30 seconds to create a hydrophilic surface to promote cell growth upon cell culture. Small 1x1 cm pieces of the carbon black-PDMS are then sliced and can be used in a smaller 36 mm petri dish for subsequent experiments. Adherent cells, such as HeLa cells, are directly cultured on the carbon-black surface using a standard protocol as discussed in the previous chapters, and the cells grow normally.

Additionally, to make titanium dioxide-PDMS, the mass of carbon black can be replaced with titanium dioxide microparticles (Sigma Aldrich Titanium(IV) oxide, anatase) that have an average particle size of 5 μm. 1:3 ratio of TiO2 to PDMS is used to create white substrates.

5.2.2 Soft lithography protocol for microcuvette chamber fabrication

The following soft lithography protocol is broken down into two different steps: (1) the creation of the silicon wafers that serves as the mold masters for the (2) PDMS microcuvette chambers. Unlike the previous silicon mold fabrication used for the thermoplasmonic gold

pyramids, the following photolithography procedure does not require chemical etching or thin metal depositions.

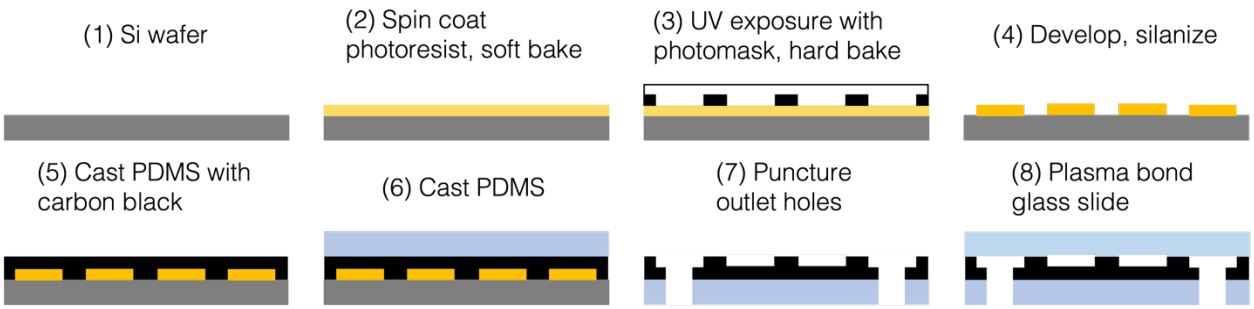

Figure 5.1: *Schematic for soft lithography. Steps (1) through (4) describe the fabrication process done in a soft matter clean room to create the micron-sized features subsequently used for casting PDMS to make the final microcuvette chambers shown through steps (5) and (8).*

First, before the photolithography procedure can begin, the photomask featuring the device pattern must be made in CAD and printed (CAD/Art). The photomask is a thin plastic transparent sheet with the pattern printed in black ink and will be later used for step 3 as depicted in the schematic of Figure 5.1. An example of a photomask cad file is shown in Figure 5.2. Because the width of each chamber is 10 mm, the photomask can fit multiple chambers on a 3-inch wafer.

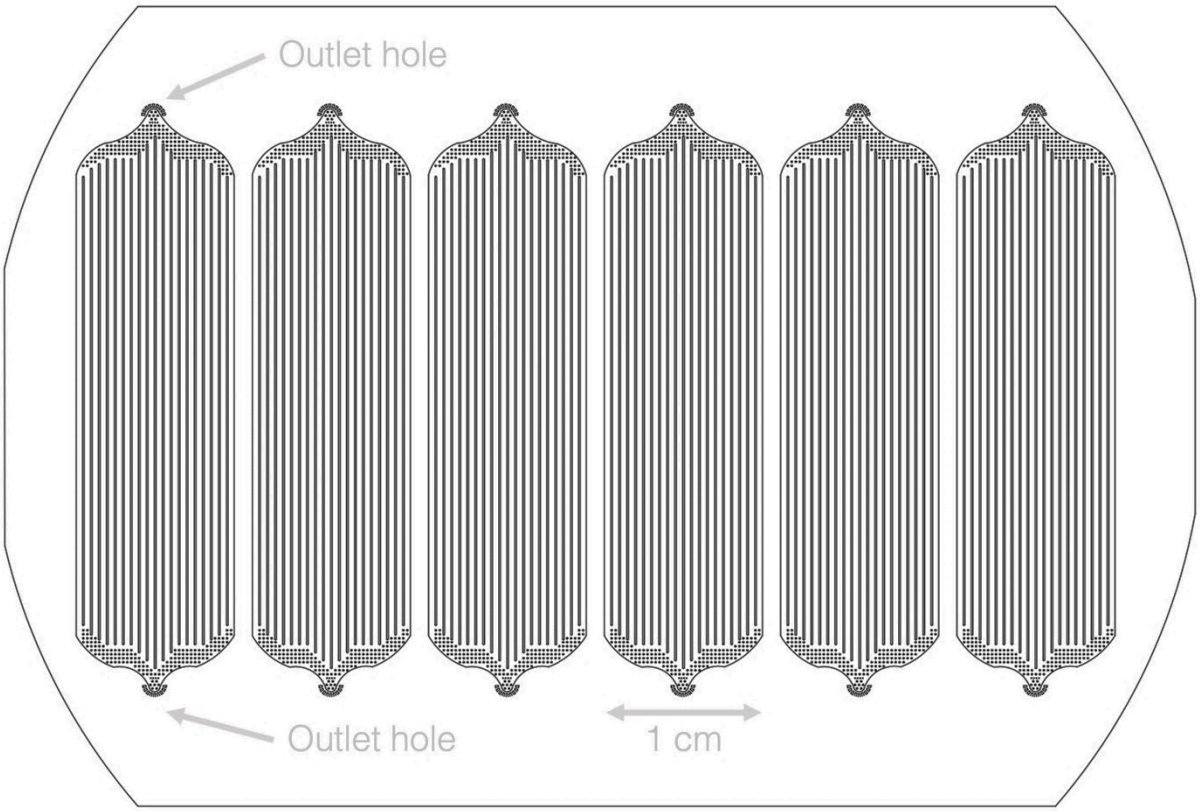

Figure 5.2: *CAD drawing of a photomask with six chambers. Each chamber has a width of 1 cm and a length of 3.5 cm from outlet to outlet. When the mask is printed, the surrounding area with no features is black, and so is the wall and pillars inside each chamber. The parallel walls and pillars near the outlets are needed due to the high aspect ratio of the chamber width and length and the chamber height (used for 10 and 12 µm height microchambers; for 15 and 25 µm height chambers, less structures are needed). Without these features, the chamber would collapse as the soft PDMS is plasma-bonded with the glass slide. The apex labelled outlet hole are the areas that are subsequently punctured to create outlets for cell injection and ejection during experiments. The grey text and arrows are not part of the CAD drawing and serve as reference.*

To begin the microfabrication process in a soft matter clean room, a silicon wafer is spin-coated with an SU8 photoresist. The different spin speeds determine the thickness of the

photoresist, which defines the height of the final microcuvette chamber. To make a layer of photoresist of 10 μm in height, SU-8 3010 is spun at 3000 rpm for 30 seconds, at 2000 rpm for 12 μm, and at 1000 rpm for 15 μm. To create the taller 25 μm height chambers, SU-8 3025 (which has a higher viscosity than 3010) is used and spun at 3000 rpm. The silicon wafer, with the SU8 coating, is then soft baked to stabilize the photoresist. For 10 μm height, it is soft baked for 2 to 3 minutes at 95 °C, 5 to 10 minutes for 12 and 15 μm height, and 10 to 15 minutes for the 25 μm height. Then, the photomask is then placed on top of the photoresist coating with the black in facing down to prevent any light diffraction by the transparent side of the sheet. Then, UV light is exposed to the entire wafer, and the light interacts with the negative photoresist in a way where the parts of the mask that is covered by black ink will be the parts that does not remain on the wafer. The portions of the photoresist that is unexposed is dissolved by the photoresist developer. For 10 μm height chambers, a UV light exposure energy of 100 to 200 mJ/cm^2 is used, 125 to 200 mJ/cm^2 for 12 and 15 μm heights, and 150 to 250 mJ/cm^2 for 25 μm height. The areas of the photoresist that was blocked from the UV light by the black ink in the photomask are left soluble as shown in step 4 in Figure 1. Thus, after the wafer is post-exposure baked at 95 °C for 1 to 5 minutes and then developed (in ethyl lactate, a solvent), the identical copy of the photomask pattern is left. To avoid adhesion between the PDMS and wafer, the surface of the cured photoresist and silicon wafer are treated. PDMS and silicon have similar surface chemistry, so they are likely to adhere to each other. The pattern may be damaged due to the adherence when the PDMS is removed. Finally, to make the surface fluorophilic, the surface of the cured photoresist and silicon wafer are silanized. The surface is covered with 0.1% fluorosilane dissolved in HFE7500 for a minute and the washed away with isopropyl alcohol, and the surface is now covered with organofunctional trichloro(1H,1H,2H,2H-perfluorooctyl)silane molecules to create a hydrophobic

coating. The silicon wafer master is now created and can be used multiple times upon PDMS casting.

The protocol to embed PDMS with carbon black has been explained in the previous section of the experimental methods. The carbon black-PDMS is poured onto the silicon masters to form a 1 to 2 mm layer ensuring that each microfeature in the wafer is covered. The wafer is then placed in a vacuum chamber for at least 15 minutes to get all the air bubbles out and baked in a 65 °C oven for at least 4 hours. Then a thicker layer of clear PDMS, serving as a backing, is poured to create a composite slab of about 5 mm as shown in step 6 of Figure 1. Air bubbles are then removed by being placed in a vacuum for 5 to 10 minutes before being baked in a 65 °C oven for at least 4 hours. The PDMS slab is then removed from the silicon master using a scalpel and peeled off. The PDMS have the structures that is inverse of the master, as shown in step 7 of Figure 5.1. Then, a biopsy punch with a diameter of 1 mm is used to create outlet holes in the carbon black-PDMS-clear-PDMS slab. The small, dashed line markers near the ends of the chambers and shown in Figure 5.2 serve as visual guides for punching. Masking tape is used to remove any debris generated by the punching. As depicted in Step 8, the chambers are bonded to a glass slide (2 mm thick) so each of the entire microcuvette chamber is enclosed except the outlets. To create a strong covalent bonding of the glass slide and carbon black-PDMS, both are plasma treated (Gala Instrumente Plasma Prep 2, at 30 W for 10 to 20 seconds) on the sides of that will be touching each other and pressed against each other with gentle pressure. Then, the device is baked with glass slide down on a 65 °C hot plate for 10 to 15 minutes. This process allows for a permanent seal to form. Finally, to make the interior of the chambers hydrophobic, they are flooded with injections of Aquapel and then immediately flushed out using air before being baked at 65 °C for half an hour to evaporate any residual Aquapel. Aquapel, which is comprised of fluoroalkylsilanes,

is often used for microfluidic devices so aqueous phase liquids can be "slippery" and move through features easier.[132] The surface treatment also promotes cell ejection at the end of each experiment so many of the cells in the chamber are retrieved for subsequent experiments.

5.2.3 Suspension cell culture and cargo preparation

In the previous experiments pertaining to metal nanostructures and polyvinyl tape surfaces, the configuration of the two-dimensional substrates constrains the applications to only cells that adhere to the surface. While the membrane of adherent cells can be functionalized to grow on surfaces, that is not a viable option for sensitive cells – particularly primary cells from a patient. Another option in handling suspension cells for substrate devices is to centrifuge the cells on the substrate to force them to be in proximity to the substrate but the cells easily become resuspended again and it would not be a robust platform. One can also simply wait for gravity to cause suspension cells to sink down to the bottom of a petri dish but that also requires a long wait period, and the cells would move away from the bottom at any slight disturbance. Thus, in order to work with suspension cells with substrate-based devices, the cells must be brought in proximity to the active material during laser irradiation. With the microcuvette chambers, we do so as shown in the schematic provided as Figure 5.3. The cells are in direct contact with the carbon black-PDMS material on the opposite side of the glass slide which allows the NIR 1064 nm nanosecond laser pulses to traverse through and activate the carbon black on the other side of the monolayer of cells.

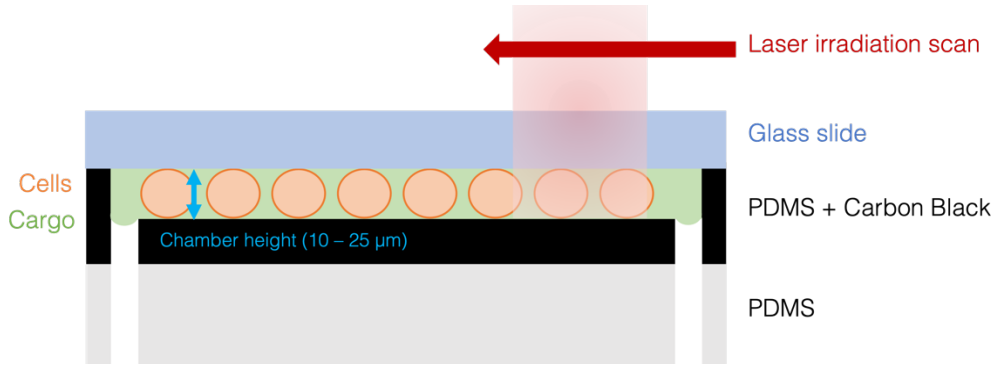

Figure 5.3: *Schematic of cells suspended and formed in a monolayer between the glass slide and carbon black-PDMS. The image is no to scale.*

For the experiments we conduct with the microcuvette chambers we can use adherent cells (HeLa CCL-2) if they have been treated with trypsin to detach from the culture flask and force them to be in suspension in the media (and thus being able to skip the step of waiting for cells to adhere overnight). However, in the work presented in this chapter, we use suspension cells (K562-s). K562 cells are a line of hematopoietic human chronic myeloid leukemia at blast crisis cells. The K562 cells are cultured normally in suspension 500 mL RPMI-1640, 50 mL FBS, 5 mL 200 mM L-Glutamine, and 5 mL Penstrep. They are cultured at 37 °C with 95% air and 5% carbon dioxide and maintained at a cell culture density of 0.2 to 1 x 10^6 cells/mL. Unlike HeLa cells, the K562 cells are always in suspension and negates the trypsinization step of the experimental protocol and does not require waiting overnight for the HeLa cells to properly grow and adhere to the substrate surface.

The first step of the experimental protocol is to prepare the cargo with which the cells will be in suspension during the laser-irradiation. For the Fluorescein isothiocyanate-Dextran polysaccharide molecules, a concentration of 25 mg/mL is used, and Leibovitz's L-15 Medium is used as a medium as it is designed to support cell health in environments without CO_2 equilibration

(which is not possible due to the microchamber configuration). Fluorescein isothiocyanate (FITC) has excitation and emission peaks wavelengths of 495 nm and 519 nm, respectively. Molecular weights ranging from 4 to 70 kDa are studied with the microcuvette chambers. For the siRNA, fluorescently tagged siRNA were used (ThermoFisher Silencer™ Cy™ 3-labeled Negative Control No. 1 siRNA with excitation max = 547 nm, emission max = 563 nm) and bulk stocks are made at a concentration of 100 μM with nuclease-free water to prevent any nucleic acid degradation in storage. For the experiments, the final concentrations of 0.1, 1, 5, and 10 μM are used and the final solution is diluted using Leibovitz's L-15 Medium instead of the nuclease-free water as the osmolarity of just nuclease-free water would cause hypotonic lysis of the cells. Cell counting is done on the K562 cells and centrifuged at 1200 rpm for 5 minutes at room temperature. The supernatant media is removed with a pipette, and the pellet of cells at the bottom of the centrifuge tube is then resuspended with the cargo-containing Leibovitz's L-15 Medium to create a final cell concentration of 80 million cells/mL. In order to insert the cells and force them to form a monolayer in the microcuvette chambers, the cells are loaded into a syringe with a blunt needle and injected through an outlet hole until the whole chamber is visibly filled with liquid (about 3 μL containing 240,000 cells for a chamber of 10 μm in height).

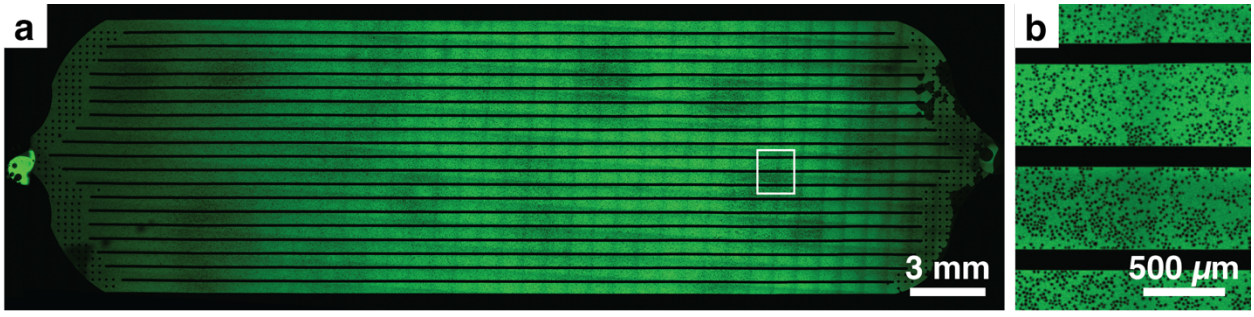

Figure 5.4: *(a) Tile scan of confocal fluorescent images of one microcuvette chamber that is 12 μm deep. The fluorescent cargo is FITC-Dextran 4 kDa and the cells are K562. The white rectangle denotes (b) zoomed in image of the cells along the walls.*

Figure 5.4 shows a stitched together confocal fluorescence tile scan image of K562 cells surrounded by green fluorescent FITC-Dextran 4 kDa cargo in a chamber. The walls and pillars supporting the PDMS and adhered to the glass slide appear black because there is no liquid with cargo there. The cells also appear black because the fluorescent cargo is not present in the cytoplasm. The faint grid-like striation in Figure 4a is due to the software's image processing or uneven illumination of the confocal laser, and not because of the IR nanosecond laser. The rough edges on the right side of the chamber are due to that area not having been completely filled with liquid, not due to fabrication error. The microchamber has not been laser irradiated before imaging and the darker splotches in the 2 mm-scale are areas where the cells have settled closer together in the monolayer formation. For example, in the inset highlighted by the white rectangle and zoomed in for Figure 4b shows that there are some areas where cells are more in proximity than in other areas.

Finally, the glass slide with the microcuvette chambers filled with cells and cargo are placed on a raster scanning stage that moves at a speed of 7,500 μm/s through a beam of 1064 nm wavelength 11-ns pulsed laser. The Gaussian beam is 1.2 μm in diameter and held constant, so accounting for the repetition rate of the 50 Hz, each point and thus each cell in the microchamber receives 8 pulses. To change the laser fluence of excitation, the laser output energy is simply increased or decreased so the beam size and shape are not changed. After irradiation, the cells are imaged in a confocal microscope to observe cargo uptake as shown in Figure 5.5.

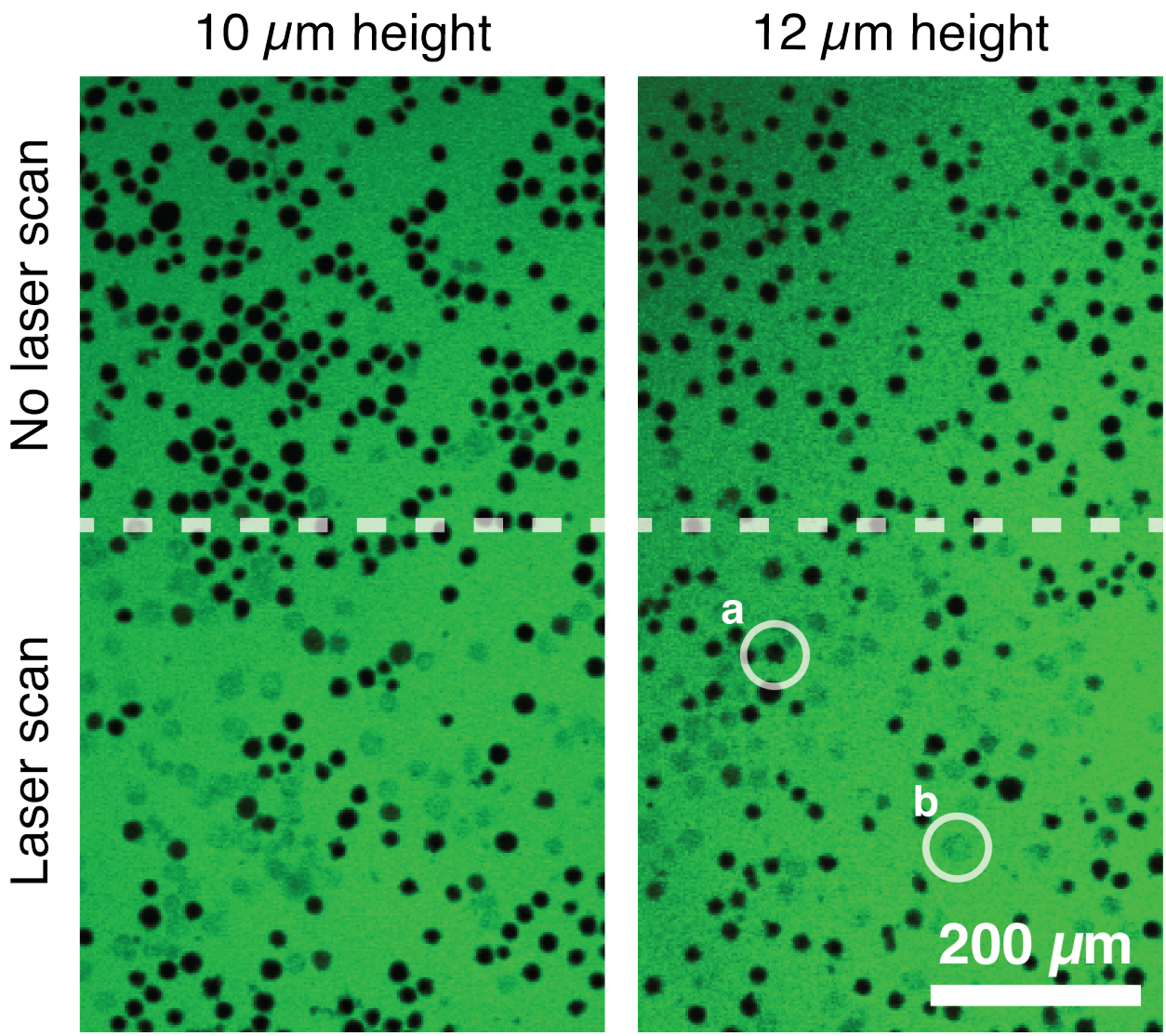

Figure 5.5: *The left panel show a fluorescence image of FITC-Dextran 4 kDa with K562 cells in a chamber of 10 μm in height and the right panel shows a chamber of 12 μm in height. The top halves of each image are areas where there was no laser excitation. The bottom halves, under the white dashed lines, are areas where a laser beam traversed through. In this case, the fluence of the laser is 50 mJ/cm². The cell circled and labelled as a is a black cell that did not uptake cargo and thus does not have green fluorescence in it. The cell that is labelled b is a cell that is faintly green because cargo has entered its cytoplasm and there is fluorescence from that location. There are some cells that appear greener and thus blend in with the background fluorescence in the*

surrounding media. Due to the saturation of the cargo in media, it is difficult to do large-scale image analysis and cell counting with imaging and thus flow cytometry is used to analyze rates of cell viability and delivery. Unlike what is depicted in this figure, experiments that are measured with flow cytometry require the entire chamber to be exposed to the laser as all the cells end up in the same tube for measurement.

To eject the cells, a plastic tubing is inserted into one of the two outlets with a vessel (petri dish or Eppendorf tube) for collection. Then a blunt syringe needle is loaded with 1 mL of Leibovitz's L-15 Medium and 0.5 mL is first manually injected through the other outlet so the medium with cells is ejected through the tubing into the collection vessel. Then, 0.5 mL of air is then injected to completely evacuate the chamber before a final 0.5 mL of medium is injected. The ejected cells are now ready to be prepared for flow cytometry.

To minimize background signal from the cargo left over in the medium, the tubes of cells for each chamber are centrifuged at 1200 rpm for 5 minutes at room temperature. The supernatant media with the remaining cargo is removed and each pellet is resuspended with 200 μL of Leibovitz's L-15 Medium and 1 uL of the fluorescent viability stain propedium iodide (mixed with DMSO at a concentration of 1 mg/mL) is mixed in and incubated at room temperature for a minute for when the cargo is FITC-Dextran. Propidium iodide (PI) is a chromosome counterstain by intercalating between DNA bases and is permeant to only dead cells. It has excitation/emission wavelengths of 535/617 nm. For when the cargo is ThermoFisher Silencer™ Cy™ 3-labeled Negative Control No. 1 siRNA, DAPI (4',6-Diamidino-2-Phenylindole, Dihydrochloride, dissolved to be 2 mg/mL in phosphate-buffered saline. 0.2 μL is added to the 200 μL of cells in medium and incubated for 5 minutes in room temperature) is used instead of PI, because PI has overlapping wavelengths as the labelled siRNA. DAPI is a nuclear and chromosome counterstain

that emits fluorescence upon binding to AT regions of DNA and has excitation/emission wavelengths of 358/461 nm. For each set of experiments of varying cargo type and concentration, a population of cells in medium with cargo present but not loaded into a microchamber serves as a complete control. Then, for each varying cargo type and concentration, another population of cells are loaded into a chamber but not laser scanned. This serves as another control to decouple the effects of cells being in the chamber and the effects of laser irradiation. Three chambers are scanned for each combination of variables (cargo type and concentration, laser irradiation fluence, and chamber height) to have a triplicate set of data.

5.3 Results

In this section of the chapter, the first two subsection will cover adherent HeLa cells grown and treated on substrate devices. The rest of this results section will cover K562 cells in microcuvette chambers.

5.3.1 Effects of carbon black concentration and laser-exposure on substrate devices

Like the black polyvinyl tape in the previous two chapters, the HeLa cells are directly grown on the carbon black-PDMS substrates, exposed to laser, imaged in fluorescence microscopy, and image analyzed using imageJ to perform cell counting to attain the viability and delivery rates for each parameter variable. As shown in Figure 5.6's SEM image, even with the addition of carbon black, the PDMS can conform and produce pyramids with sharp edges and apexes. The viability and efficiency curves in the two plots of Figure 5.6 also demonstrate that there are no significant differences in cell survival and cargo delivery rate between carbon black-PDMS that have been patterned and carbon black-PDMS that are flat with no regular micron sized features. While the gold thin film pyramids prove to deliver cargo to cells and flat gold does not, the carbon black-PDMS may not focus the laser-enabled heating effect.

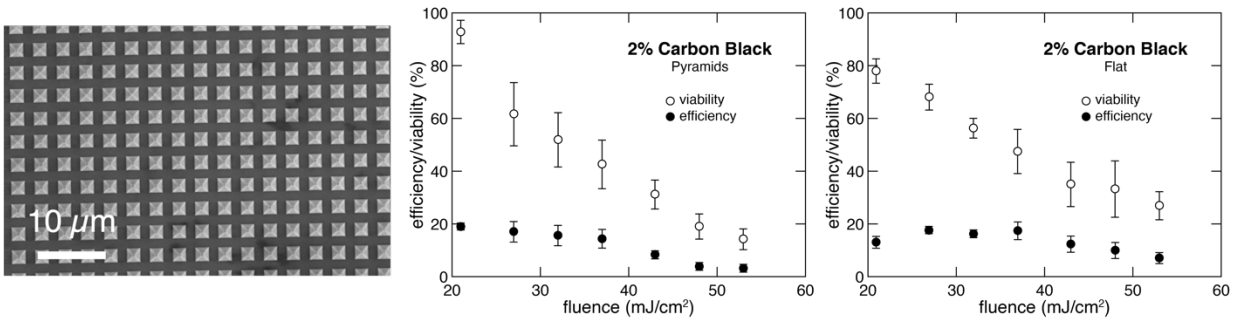

Figure 5.6: *The SEM image on the left shows 2% carbon black-PDMS that have been patterned using the inverse pyramid silicon master mold that was previous presented in Chapter 2. The left plot shows the viability and efficiency rates of calcein green to the cells when they are grown on these pyramid-patterned substrates, at varying laser irradiation fluences. The right plot shows the viability and delivery rates of calcein green to the cells when they are grown on flat substrates, at varying laser fluences. Each point in the plots represent the mean of three samples and the error bars represent standard error.*

Upon the increase of carbon black concentration in the PDMS, the delivery rate of calcein green (0.648 kDa) does not increase significantly but the viability rate decreases by half when comparing substrates with 0.5% carbon black to 2% carbon black as plotted in Figure 5.7.

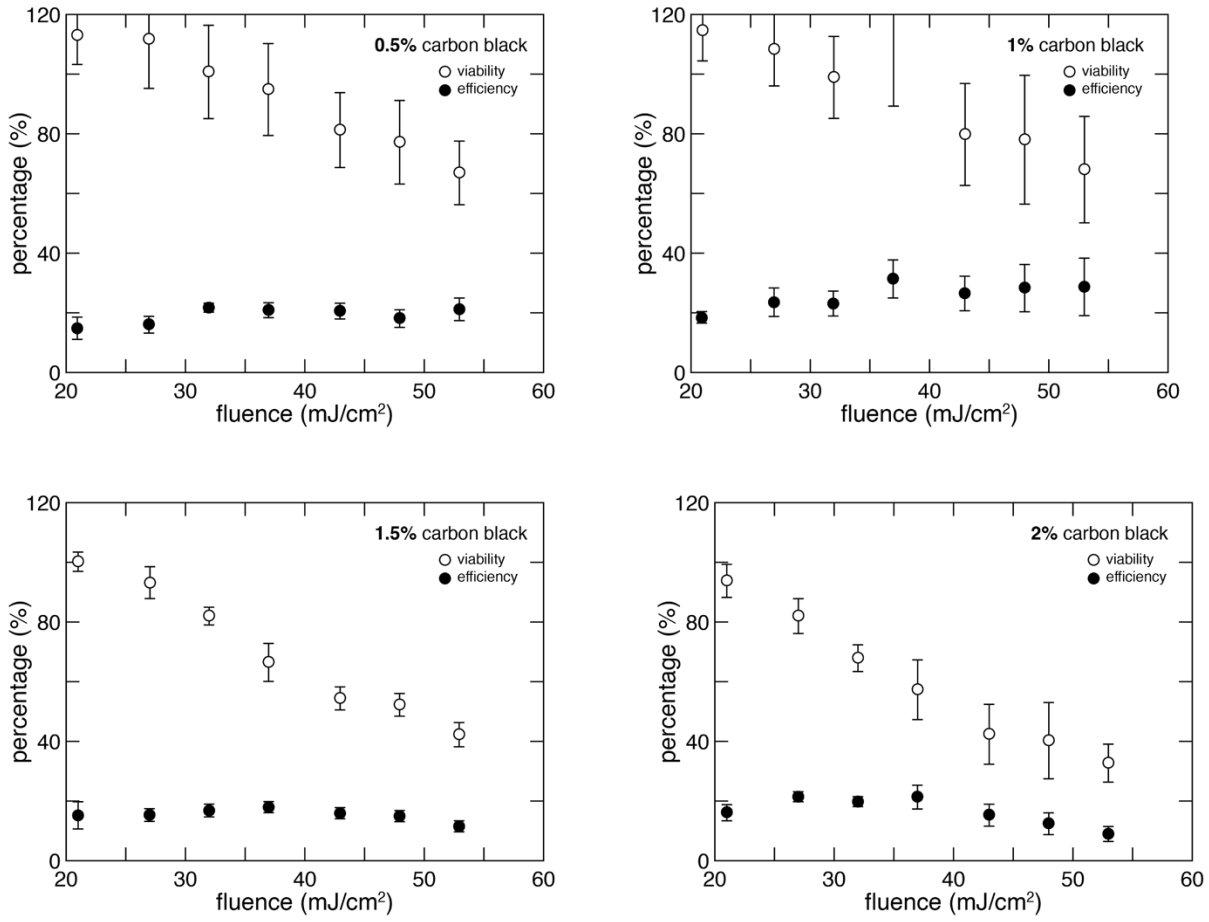

Figure 5.7: *Delivery and viability rate for PDMS substrates with varying carbon black mass percentages. The cargo delivered was calcein green, and image analysis with imageJ was used to obtain triplicate samples. Each point is the mean of three samples and the error bars denote standard error. The viability and delivery rates are calibrated with the number of cells in a non-scanned area. However, for 0.5 and 1% control areas, the cell density was relatively low which is why the viability percentage in those plots for lower laser fluences go above 100%.*

Although varying the laser fluence does not change the delivery rate of calcein green to HeLa cells very much and the viability begins to drop as the fluence is increased, the cell viability sacrifice can be decreased by simply decreasing the laser fluence but increasing the number of

pulses each cell is exposed to. Figure 5.8 explores this semi-quantitatively as no triplicate experiments are shown but the percentage of delivery and viability are performed using imageJ cell counting. A substrate of 2% carbon black-PDMS is used. A relatively low laser fluence of 30 mJ/cm^2 is used. To vary the number of laser pulses that are exposed to every cell, instead of changing the repetition rate of the laser pulses, the scanning speed of the stage is simply varied. When the stage moves at 10,000 μm/s, each cell receives 6 pulses and at 5,000 μm/s, each cell receives 12 pulses. As shown in the left green fluorescence image in Figure 5.8, when number of pulses are increased from 6 to 12, the delivery rate increases from 28% to 42%. When the viability of the cells in the two regions is compared as shown in the right red fluorescence image, the viability rate has only gone down by 3% because the laser fluence of 30 mJ/cm^2 is relatively low. This shows that by varying laser parameters other than laser fluence, such as number of pulses, can deliver to more cells within a population without sacrificing viability.

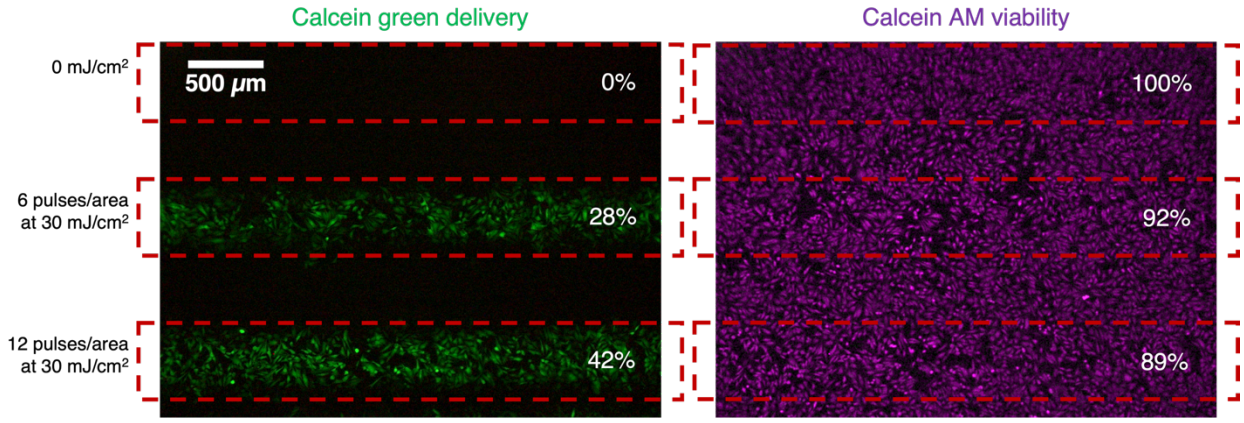

Figure 5.8: *The image on the left is the fluorescence microscopy image of HeLa cells that have calcein green successfully delivered into the cytoplasm. The areas surrounded by red dashed lines are where the laser irradiation has occurred. The image on the right are the same cells as the cells shown on the left but in the red fluorescence channel. The image has had red altered to magenta for ease of viewing and the cells that are magenta are cells that have survived the laser irradiation.*

The percentages in each dotted rectangles show either the percentage of cells that have been delivered two (left image) or the percentage of cells that have survived (right image) compared to the non-laser irradiated area. The top third of each image where no laser has been scanned serve as the control.

As the previous chapters have shown, white polyvinyl tape can also deliver cargo to cells with very high viability. In Figure 5.9, HeLa cells are grown on 33% TiO2-PDMS substrates. The left green fluorescence image shows the two tracks where the laser was scanned at 10,000 μm/s. The top track is irradiated at a higher fluence of 53 mJ/cm^2 and the bottom track is irradiated at a lower fluence of 42 mJ/cm^2. There are more green cells in the higher fluence region than in the lower fluence region. The other dark areas are where there was no laser exposure, thus none of the cells in those regions have calcein green delivered into the cytoplasm. The viability image in Figure 8 shows little to no cell death when areas of laser irradiation occurred compared to control no laser areas.

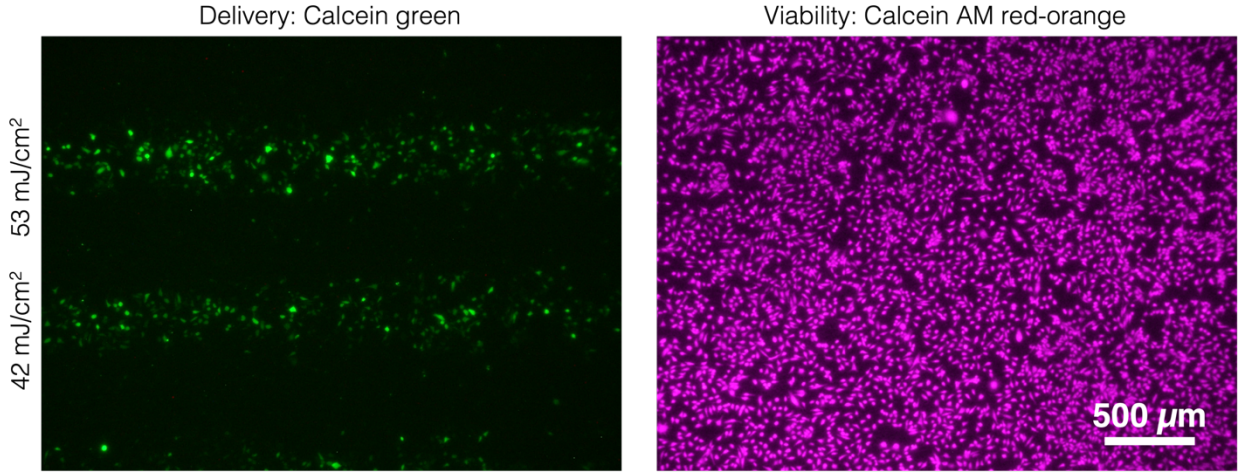

Figure 5.9: *The image on the left is the fluorescence microscopy image of HeLa cells that have calcein green successfully delivered into the cytoplasm. The image on the right are the same cells as the cells shown on the left but in the red fluorescence channel. The image has had red altered*

to magenta for ease of viewing and the cells that are magenta are cells that have survived the laser irradiation.

5.3.2 Spatially and temporally selective multiple-cargo delivery

One benefit that substrate devices have is the ability to selectively deliver different kinds of cargo to the adherent cells at different time points in one petri dish. This may be of interest to developmental biologists, especially because sensitive cells may grow better on polymer substrates instead of metal nanostructures.[133] For example, if a population of embryonic stem cells are growing in the same petri dish but only selective cells in specific areas are treated to have gene expression, how would the non-treated cells behave upon the difference? For the scope of this section, HeLa cells and calcein green and Dextran cargoes are continued to be used as proof-of-concept in place of more sensitive cell lines and more dynamic cargoes such as CRISPR-cas9.

Figure 5.10 shows an experiment where two laser scans were done at different times while different cargo were present in the petri dish. A laser fluence of 40 mJ/cm^2 is used while the beam size is 1 mm. First, a square and the horizontal mark of the letter H are scanned by moving the scanning stage in a macro-programmed path while there is 1 mL of 25 mg/mL Invitrogen™ Dextran, Cascade Blue™ , 3000 MW (excitation/emission of 400/420 nm) in PBS present. Then, 5 minutes are waited to allow for the cell membrane pores to reseal before the medium with Cascade Blue-Dextran is removed and replaced with 1 mL of 0.57 mg/mL calcein green. Then, the entire letter H is scanned again, overlapping the horizontal marking with the same area of the horizontal marking scanned during the exposure to Cascade Blue-Dextran 5 minutes prior. When fluorescence imaging is done, it can be seen in Figure 10c that cells in the path of the square have fluorescence in the blue channel, along with the cells in the horizontal marking of H. Meanwhile, the cells in the green channel show that the cells scanned in the H path have calcein green delivered

to them as shown in Figure 5.10b. However, there are some cells in the square around the H, that were irradiated 5 minutes before introduction of calcein green, that also has calcein green. This indicates that not all the cell membrane pores have resealed in the 5 minutes. A longer time duration of wait period can be taken in order to allow for all the cells to reseal before the introduction of a second cargo type. The cells in the horizontal marking of the H scan show uptake of both Cascade Blue-Dextran and calcein green cargoes as they are fluorescent in both the blue and green channels. However, significant cell death is shown in this region in the calcein AM red-orange channel in Figure 5.10 which indicate that 5 minutes was not long enough to allow for the cells to recover from the laser irradiation. This shows concurrent delivery of different cargo at

different time points, with spatially selective treatment by varying the scanning stage movement path underneath the laser beam.

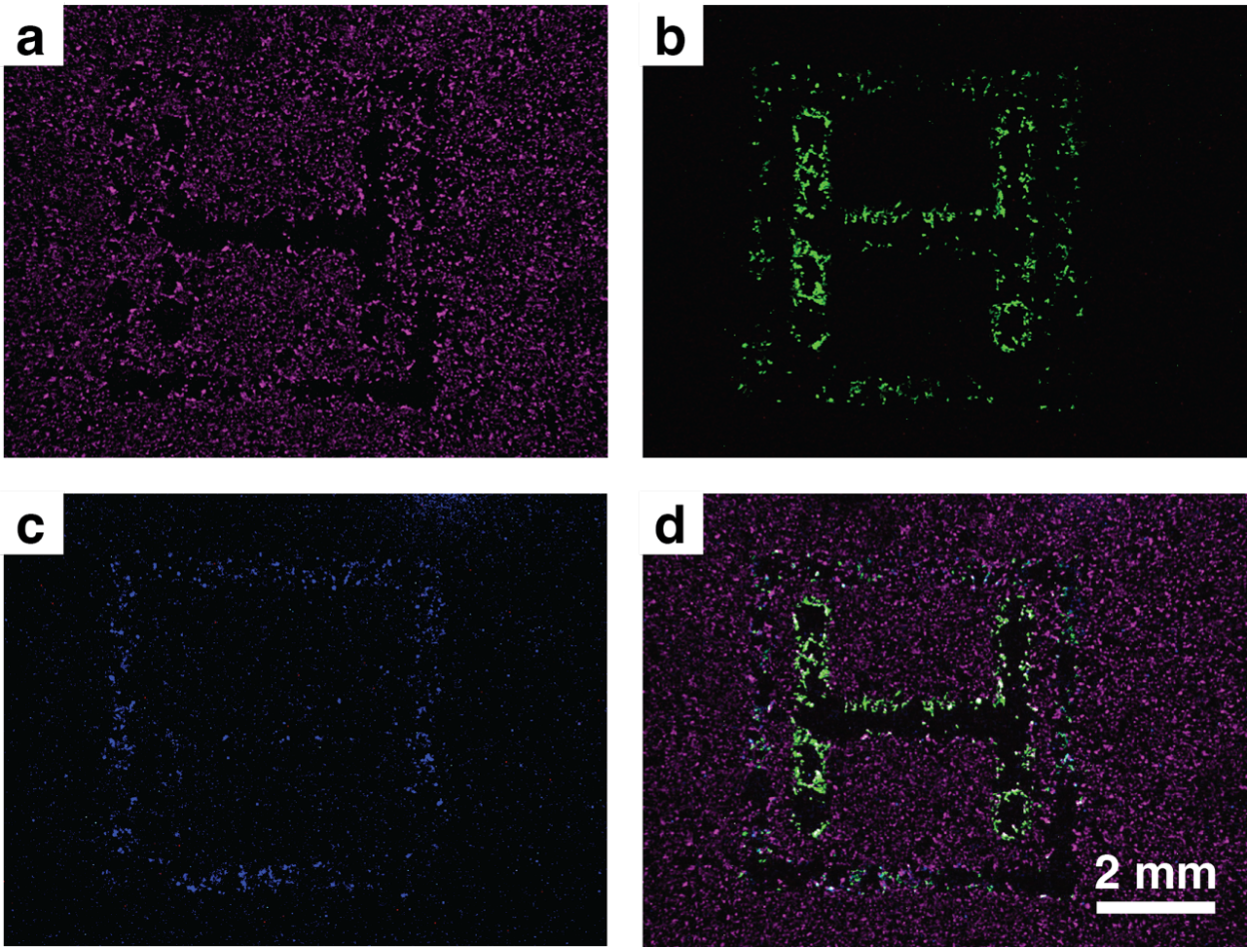

Figure 5.10: *Each of the four image in this figure are of the same area of cells but in different fluorescence channels. (a) Calcein AM red-orange fluorescence altered to be red instead of magenta, showing cells that are alive and remain growing on the substrate. (b) Calcein green fluoresence. (c) Cascade Blue-Dextra 3 kDa fluorescence. (d) an overlay of the red, green, and blue channels that are shown by (a) – (c).*

5.3.3 Effects of carbon black concentration and laser-exposure on microcuvette devices

From this section on, the rest of this results section will cover the experimental results of laser-irradiated microcuvette devices for cargo delivery to K562 suspension cells. The introduction of carbon black to PDMS allows for delivery in the chambers, whereas clear PDMS does not, as shown by the bar chart in Figure 5.11. When the concentration of 2% mass carbon black is added to the PDMS for the chamber microfabrication, there is only about 28% delivery of FITC-Dextran 4 kDa. When the carbon black concentration in the PDMS is increased to 5%, the average delivery rate is increased to 44%. This implies that the carbon black is indeed necessary to create cell membrane permeation for cargo delivery upon laser irradiation, and that increasing the amount of carbon black also increases cargo delivery. This may be because there is more absorption of the laser energy as the presence of carbon black is increased in the PDMS. The viability rate for the experiments is all nearly 100%, comparable to the control cells that were never injected into the chambers, even for the highest 5% concentration of carbon black. If the concentration of carbon black is increased in the PDMS, the combination causes the PDMS to be very thick and produces inconsistent and inaccurate microcuvette chambers with the silicon wafer masters. This may be remedied by using a PDMS catalyst-base ratio that lowers the initial viscosity before adding the carbon black. Thus, for the rest of the experiments in this section, 5% carbon black is used. For outlook, to increase the carbon black concentration and thus increase the delivery rate, a polymer base with a lower viscosity than PDMS 10:1 base to catalyst may be used. It should also be noted that if the 5% carbon black is replaced by 33% titanium dioxide and formed into the same microchamber shape, no uptake of cargo occur, even when irradiated at a high fluence of 66 mJ/cm^2, unlike the TiO2-PDMS material when it is used as a substrate device and cells are delivered to as shown in Figure 5.9.

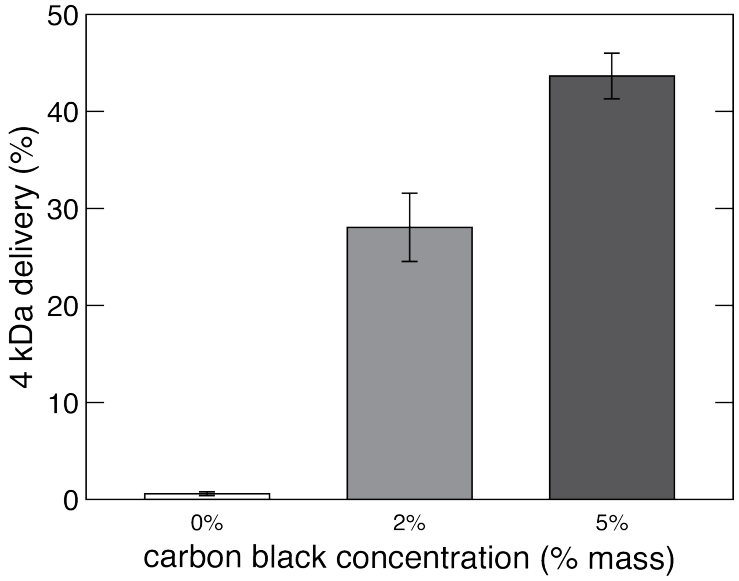

Figure 5.11: *Bar chart showing the delivery rate of FITC-Dextran 4kDa to K562 cells using microcuvette chambers containing varying percentage mass of carbon black. The solid bars represent the mean of three different samples and the error bars represent the standard error of the n = 3 sample set. A laser irradiation fluence of 50 mJ/cm² is used for each, and the only parameter that has changed is the amount of carbon black in the PDMS chamber. This data is from flow cytometry, and 10,000 cells were analyzed for each sample.*

Another experimental parameter which is important to explore is laser irradiation fluence. As shown in Figure 5.12, as the laser fluence is lowered, less and less green cells (cells with cargo in it) are seen and more cells remain black (without cargo). This means that higher delivery rate is in correlation with higher laser fluence. However, with the cells are ejected from the respective chambers, many cells that have cargo inside are stuck and remain inside the chamber. Also, at high fluences (above 50 mJ/cm²), bubbles can sometimes be seen in the chamber and do not disappear for over an hour, so they may not be vapor bubbles are vapor bubbles collapse very quickly. [134] Since PDMS is a reticulated polymer and all the molecules are bonded to each other with covalent

bonds, it cannot be reformed with heat. Unlike polyvinyl which melt at higher temperatures, PDMS does not deform. This implies that the chamber height does not change above 50 mJ/cm^2 and perhaps the reason why the cells are stuck in the higher fluence irradiated chambers is due to cells swelling too much and getting stuck or extreme heat degrading proteins.

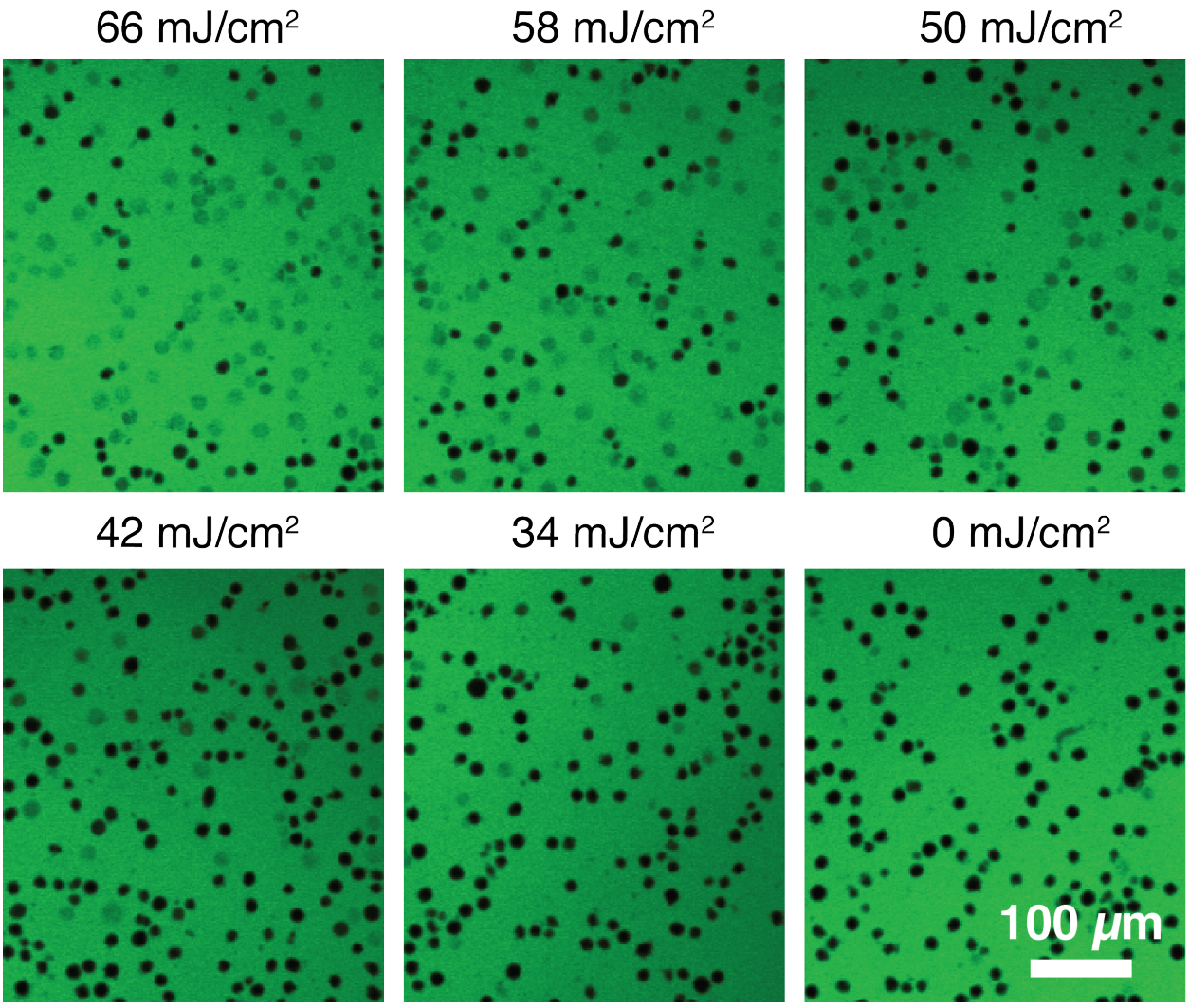

Figure 5.12: *Fluorescence microscopy images of K562 cells with FITC-Dextran 4kDa in media. The corresponding fluence of the laser that irradiated the region is labelled above each image. The cells in these images are in a 12 μm height chamber with 5% carbon black embedded in the PDMS.*

Because it is important to retrieve and recover the cells after laser-irradiation and cargo delivery, the highest fluence we use and subsequently show in the next figures is 50 mJ/cm^2. Repeated scanning or increase in number of laser pulses exposed (by slowing the stage speed) with a lower laser fluence may be explored in the future but at 50 mJ/cm^2, the cells are ejected and have the same range of high >95% viability as cells in non-irradiated control chambers and control cells that were not injected in the chamber or exposed to laser. The suspension cells in the microcuvette chambers show higher cell viability than the adherent cells on the substrate devices upon laser irradiation.

5.3.4 Delivery of kilo-Dalton range fluorescent particles

As it has been demonstrated in the prior chapters, FITC-Dextran is used as model cargo for the following experiments. The concentration of the FITC-Dextran is held constant at 25 mg/mL, but the polysaccharide chain length is varied: 4 kDa, 10 kDa, 20 kDa, and 70 kDa. Figure 5.13 is a compilation of fluorescence images of various FITC-Dextran sizes, upon laser irradiation and without as control. The images provide a qualitative visual of how the delivery rate of the fluorescent cargo decreases as the size of the cargo increases. Additionally, the cells that appear green and with cargo inside for the small 4 kDa cargo is more brightly green than the cells with cargo inside for the larger 70 kDa. This implies that more cargo has been delivered to each cell that have cargo in it for the smaller cargo than for the large cargo, as it is easier for smaller molecules to diffuse into the transient pores. The Stokes radius, or effective hydrated radius in solution, is roughly 1.4 nm for Dextran-4 kDa, 2.9 nm for 10 kDa, 4.3 nm for 20 kDa, and 7.1 nm for 70 kDa, implying that the pore sizes created in the membrane ranges have diameters that range between 1.4 and 7 nm.[135,136]

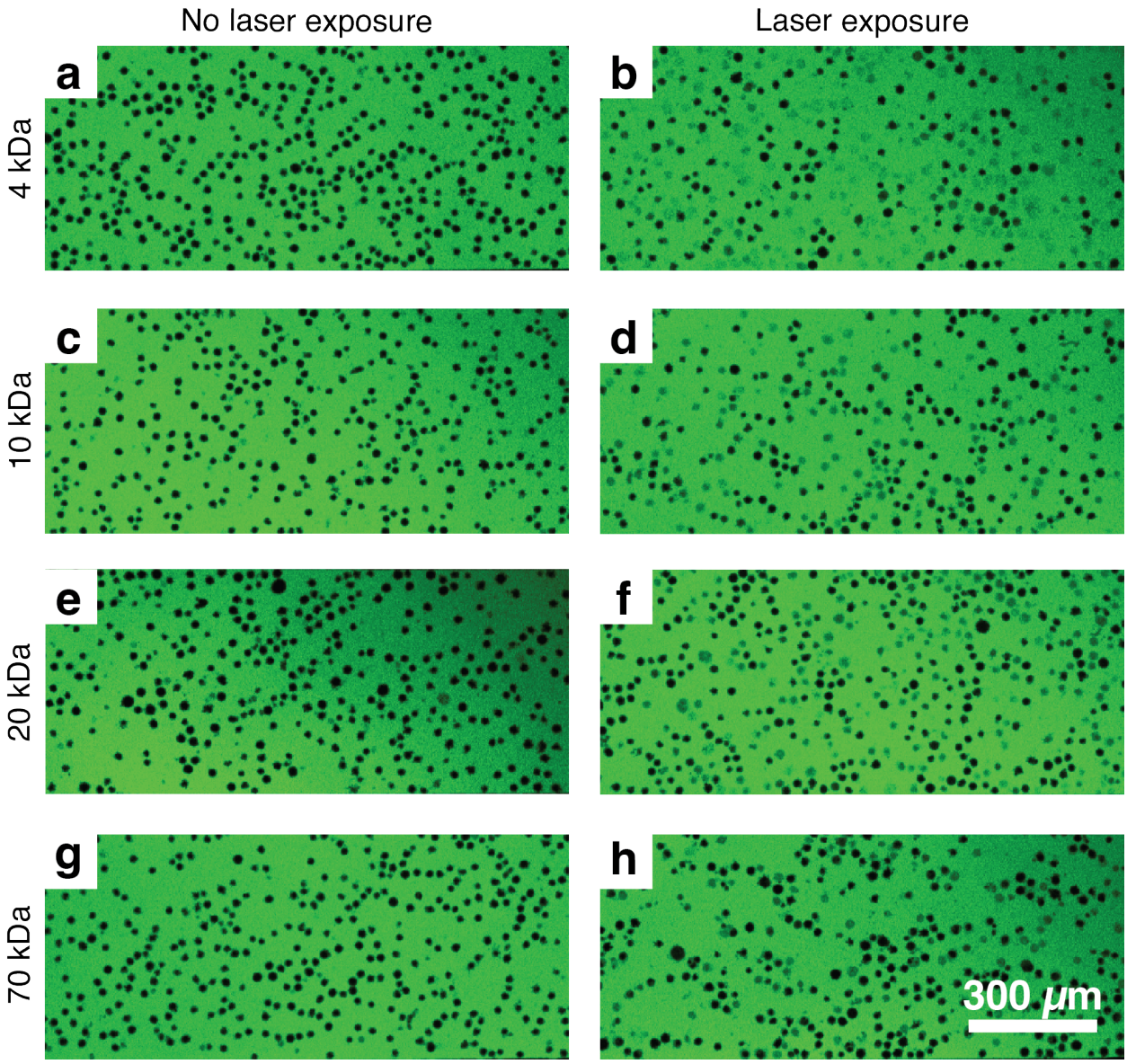

Figure 5.13: *Fluorescence images for K562 in 12 μm height chambers. The images in the left column are control areas where laser was not scanned. The images in the right column have been irradiated with laser at a fluence of 50 mJ/cm² at a speed of 7,5000 μm/s, so each cell receives 8 pulses. (a) and (b) have FITC-Dextra 4 kDa, (c) and (d) have 10 kDa, (e) and (f) have 20 kDa, and (g) and (h) have 70 kDa. The cells that appear faintly dark green against the green background media are cells that have the fluorescent cargo in the cytoplasm. The black cells are where there is no fluorescence, thus no cargo in the cytoplasm.*

Flow cytometry measurements were also conducted for 10 μm and 12 μm height chambers with the same cargo shown in Figure 5.13. Figure 5.14, in this case, provides a quantitative analysis of delivery rate. The delivery rate for large cargo decreases as the cargo size is increases. It should also be noted that viability is not plotted here, as for 50 mJ/cm^2 laser irradiation, the viability is near 100% as compared to the control group of cells that were neither injected into the chamber nor laser irradiated.

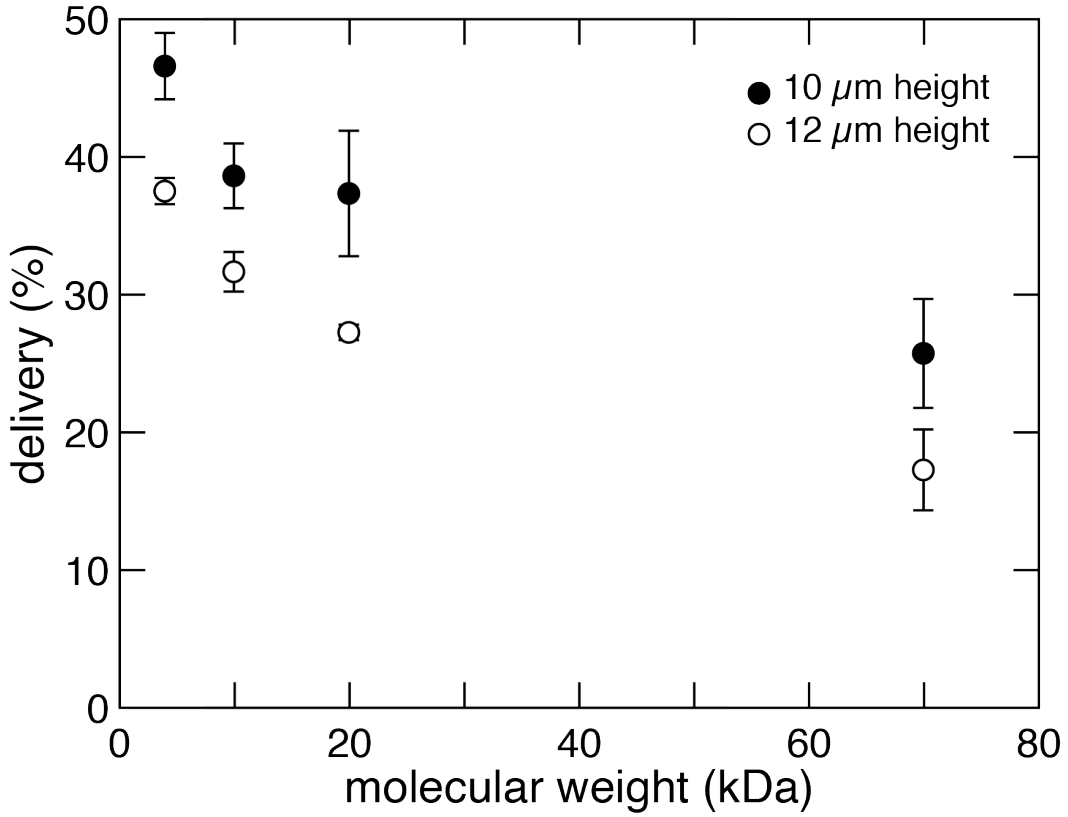

Figure 5.14: *Flow cytometry measurements of cargo delivery of various FITC-Dextran sizes. The black dots indicate the delivery rate for 10 µm height chambers and the white open dots represent the delivery rate for 12 µm height chambers: average of three different chambers with the error*

bars representing the standard error. 10,000 cells are analyzed from each chamber and calibrated to no laser irradiation as the zero-delivery rate.

The delivery rate with 10 μm height chambers are always higher than delivery with 12 μm height chambers, indicating that the chamber height plays a role in determining the delivery rate, so the delivery rate of Dextran 4 kDa and 10 kDa with 10, 12, 15, and 25 μm height chambers are plotted in Figure 5.15. The delivery rates drop significantly from the 12 μm chambers to the 15 μm chambers, but the delivery rates for 15 and 25 μm are similarly low to one another.

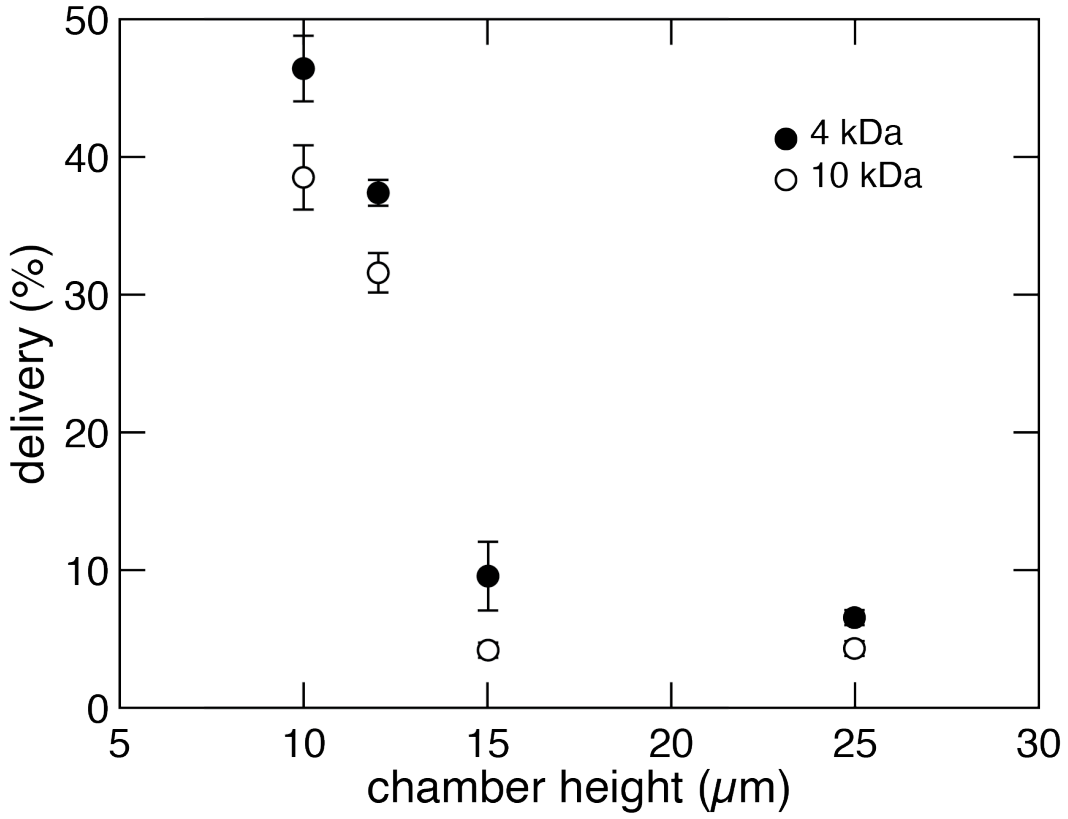

Figure 5.15: *Flow cytometry measurements of cargo delivery of FITC-Dextran 4 kDa and 10 kDa with chambers of various heights. The black dots indicate the delivery rate of 4 kDaand the white open dots represent the delivery rate of 10 kDa: average of three different chambers with the error*

bars representing the standard error. 10,000 cells are analyzed from each chamber and calibrated to no laser irradiation as the zero-delivery rate.

The influence of chamber height on delivery may indicate that cells must be in direct contact with the carbon black-PDMS in order to receive enough perturbation to become permeated to allow cargo to diffuse into the cytoplasm. Figure 16 shows fluorescence images of K562 cells in chambers with different heights. Because the 25 μm height chamber has enough space the cells to effectively float around, the cells move around in the chamber and form two layers of cells. This is why the density of cells are also high in the image and some of the cells are out of focus.

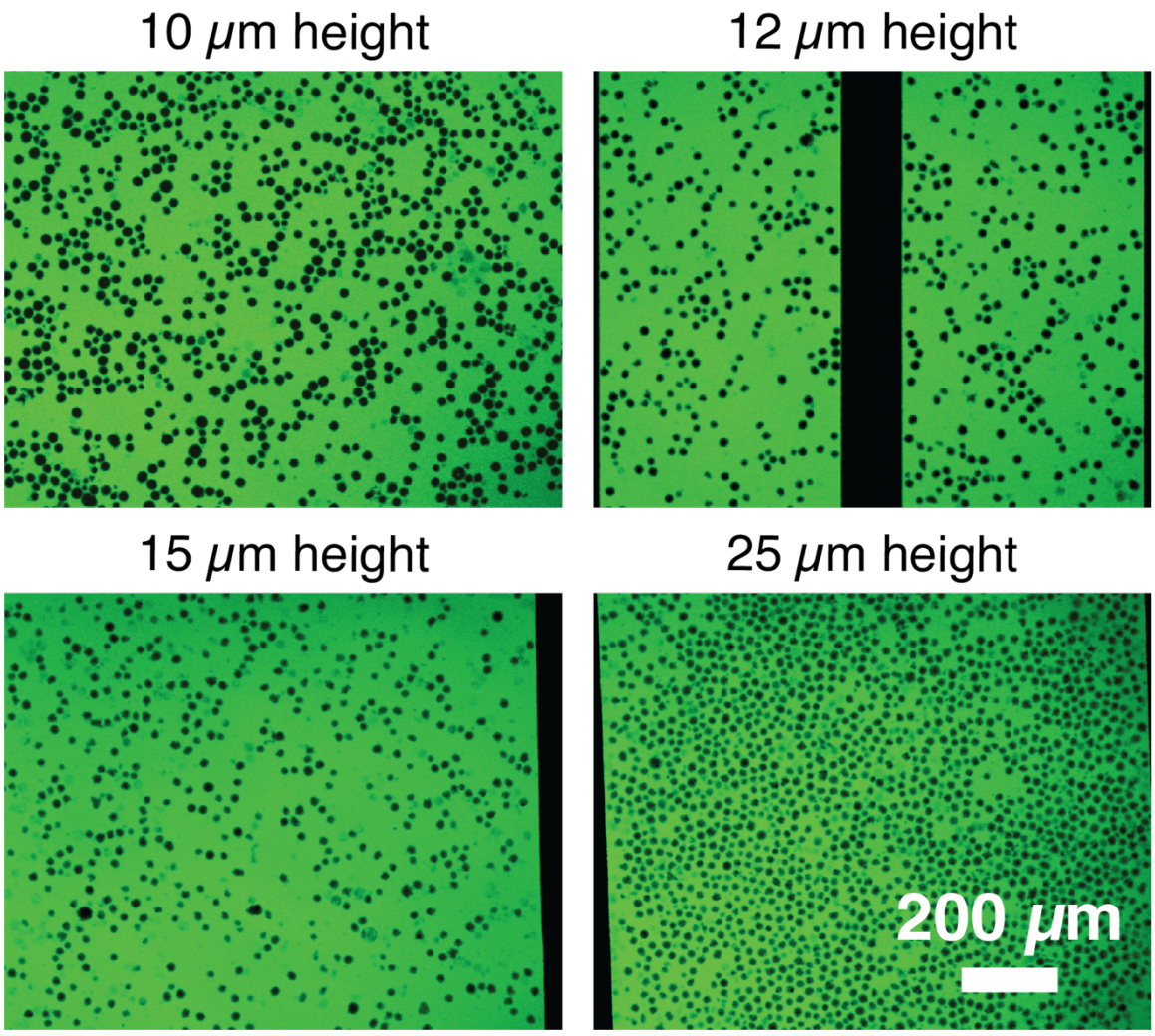

Figure 5.16: *Fluorescence images of non-laser irradiated cells in chambers of different heights. These cells are K562 in a solution of media with FITC-Dextran 4 kDa. Green cells can be seen in the 15 and 25 μm heights, but that is not due to fluorescence inside the cellular cytoplasm. The change in brightness is due to the cells being at different heights in the focal plane of the microscope. Only the black cells are analyzed, so cells in different planes are not accounted for in particle size analysis done subsequently. The black striation in the images is the microcuvette chamber wall that prevents collapse against the glass slide upon plasma bonding during microfabrication.*

The images from Figure 5.16 are then analyzed and the area of the cells are processed and calculated using the Analyze Particles feature of imageJ, and then the diameter is calculated from the area and plotted as a swarm chart plot in Figure 5.17. These suspension cells are generally spherical. The cells in the 15 and 25 μm have a diameter that is less than the chamber height (12.1 and 12.3 μm, respectively, and are both less than their chamber heights, showing that the cells are indeed floating around and are not subject to any compression force from the chambers. However, when the chamber height is decreased to 12 μm, the average diameter is 12.73 μm which is bigger than the chamber height and bigger than the average diameter for the taller chambers. This implies that the cell is being forced to form a monolayer and touching both the glass slide side and the carbon black-PDMS surface. This chamber height is also when the delivery rate for 4 kDa at 50 mJ/cm^2 jumps from 10% with 15 μm chambers to 38% with 12 μm chambers. Finally, the average cell size diameter in the 10 μm chamber is 14.33 μm which is almost 50% bigger than the chamber height. This strongly suggests that the normally spherical cell is being squeezed into a pancake shape and is under compression stress between the carbon black-PDMS and glass slide. Although the dimension of the 10 μm chamber is not nearly as narrow as some delivery platforms using narrow microfluidic squeezing, this implies that the cells are deformed in the smaller chambers. However, the viability of the cells after they are ejected is nearly 100% when irradiated at 50 mJ/cm^2 which shows that this amount of squeezing (while in the chamber ranging from 30 minutes to several hours of consecutive experiments before being ejected) does not cause so much stress that the K562 cells die any more than they would be in a tube of cells that are not injected in a chamber nor laser irradiated. The average delivery rate of 4kDa with the 10 μm chambers is 48%, 20% higher than that with the 12 μm chambers. Both the increase in surface area of the cell membrane pressed against the carbon black-PDMS or increase in compression pressure applied to

the entire cell may have a role in that jump in delivery increase. While this plot is specifically featuring K562 cells, larger or smaller cells may require different chamber heights to produce a similar cargo delivery magnitude effect.

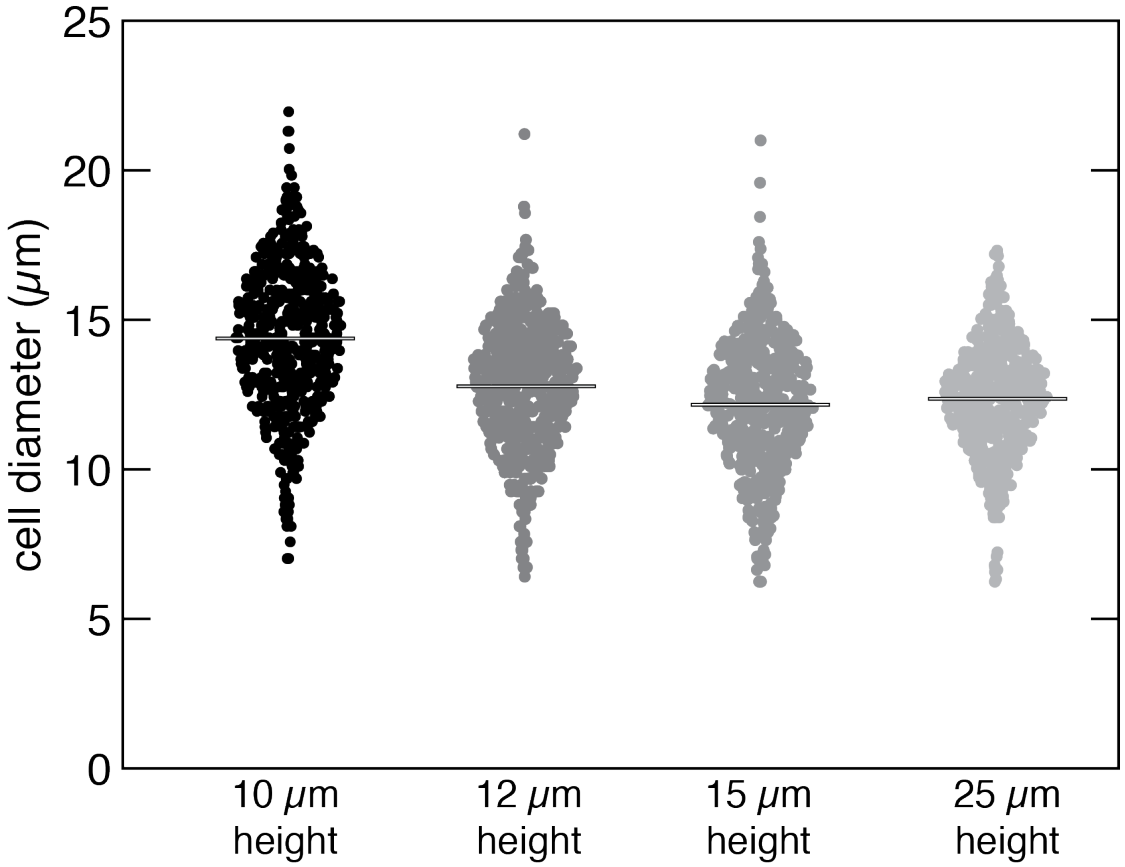

Figure 5.17: *Swarm chart plot of cell diameter from the images in Figure 16. The bar in the middle of each plot indicates the average diameter size of the cell. The average diameter for the cells is 14.33 µm in the 10 µm chamber, 12.73 µm for 12 µm chamber, 12.1 µm for 15 µm, and 12.3 µm for 25 µm. Each swarm features 515 points, representing 515 cells from each image.*

5.3.5 Delivery of siRNA

Small interfering, or sometimes known as short interfering ribonucleic acid (siRNA) is a type of double stranded RNA that is usually 21 base pairs in length and operate in the RNA interference pathway in a cell. It can interfere with the expression of specific genes that have the complementary nucleotide sequence. RNA interference with siRNA has promising therapeutic applications and are interesting to study in vitro for cell biology research purposes as well. For example, siRNA can be used as a research tool to probe single gene function.[137–139] One way to detect siRNA delivery is with gel electrophoresis and Western blot analysis, but for this section of experimental results, the siRNA that is delivered has been tagged with a fluorophore.[140] Thus, we continue to use fluorescence microscopy and flow cytometry to detect the delivery of siRNA into the cytoplasm. The molecular weight of the 21-nucleotide double-stranded siRNA molecule is about 13 kDa, but as with all genetic materials it is negatively charged while Dextran is neutrally charged.[141] Similar to the experiments with FITC-Dextran, the cell viability is measured and compared to control cells and the viability always remains at the same level as K562 cells that are not laser scanned nor injected into the chambers. For functional proteins like siRNA, there is a limit to how concentrated the cargo can be in the liquid medium (unlike Dextran, which is abundant, so it is easy to saturate the cargo in the medium). If these siRNA experiments were done in a petri dish with a substrate device, the liquid volume needed to treat 240,000 adherent cells in a 24-well plate would be at least 300 μL for consistent experiments. Whereas to treat the same number of cells in a 10 μL chamber, only 3 μL of liquid volume with cells suspended (at a density of 80 million/mL) in it would be needed.

Figure 5.18 shows a plot of delivery rate percentage of siRNA to K562 cells in a 12 μm height chamber. If the concentration of the siRNA in the medium surrounding the cells is increased, the delivery rate increases as well. The average delivery rate when the cargo

concentration is 0.1 μM is 12% and when the concentration is increased an order of magnitude to 1 μM, the delivery rate increases to an average of 29%. However, the average delivery rate at 5 μM and 10 μM are both around 45%. Surprisingly, the delivery rate of FITC-Dextran 10 kDa with the same parameters (5% carbon black 12 μm height chamber irradiated with 50 mJ/cm^2 laser fluence, 8 pulses per cell) yield an average delivery rate of 32% which is below 45%. It should be noted that the concentration of 10 kDa at 25 mg/mL is 2.5 mM which is orders of magnitude greater than 10 μM. Additionally, the fluorescently tagged siRNA is 13 kDa, greater than 10 kDa and is also negatively charged – and so is the cell membrane and there should be a repulsion force to be accounted for in addition to the diffusivity. One reason that the delivery rate of the siRNA may be higher than of the FITC-Dextran may be because Dextran is a long polysaccharide chain that has a Stoke's radius of 2.9 nm, siRNA has a Stokes radius of 2 nm and could more easily diffuse into the smaller transient pores formed in the cell membrane.

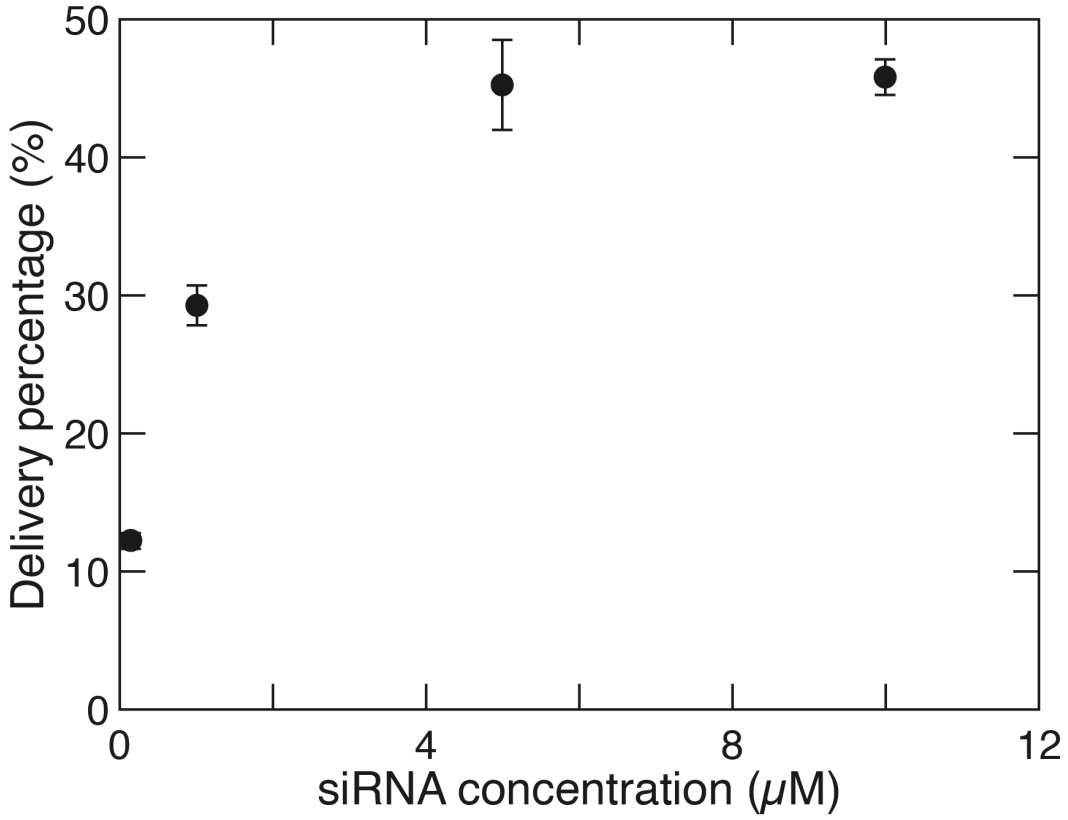

Figure 5.18: *Delivery rate plot of Invitrogen™ Silencer™ Cy™ 3-labeled Negative Control No. 1 siRNA to K562 cells in a 12 μm height chamber, irradiated at 50 mJ/cm2. The delivery rate is measured using flow cytometry and each data point represent the average of cells in three different chambers (10,000 cells are measured for each chamber) and the error bars denote standard error.*

The fluorescence images of FITC-Dextran delivery to K562 cells show that the brightness of the surrounding medium is higher than the brightness of the successfully delivered to cell. This means that the concentration of the cargo is higher outside of the cell than inside of the cell, which is intuitive as the pores allowing the cargo to diffuse into the cytoplasm is transient and the cell membrane seals back up before equilibrium of the cargo concentration can be met. Thus, it would have been safe to assume that due to the dependence of passive diffusion to allow cargo into the

cell, the concentration of the cargo outside of the cell will always be higher than inside the cell. However, this does not seem to be the case for siRNA. As Figure 19 shows, the green delivered-to cells in the lower concentrations seem to have a great difference in brightness between in the cell and outside of the cell than for the higher siRNA concentration images. Because the confocal laser excitation voltage is the same throughout each image, for example the concentration of cargo in the medium for Figure 5.19b is lower than the concentration of cargo in the K562 cytoplasm which has a brighter emission. This effect is not seen with FITC-Dextran and suggests that the delivery of the siRNA molecules is not entirely based on passive diffusion but there may be another feature that promotes the intake of siRNA cargo that is not present for when FITC-Dextran is delivered.

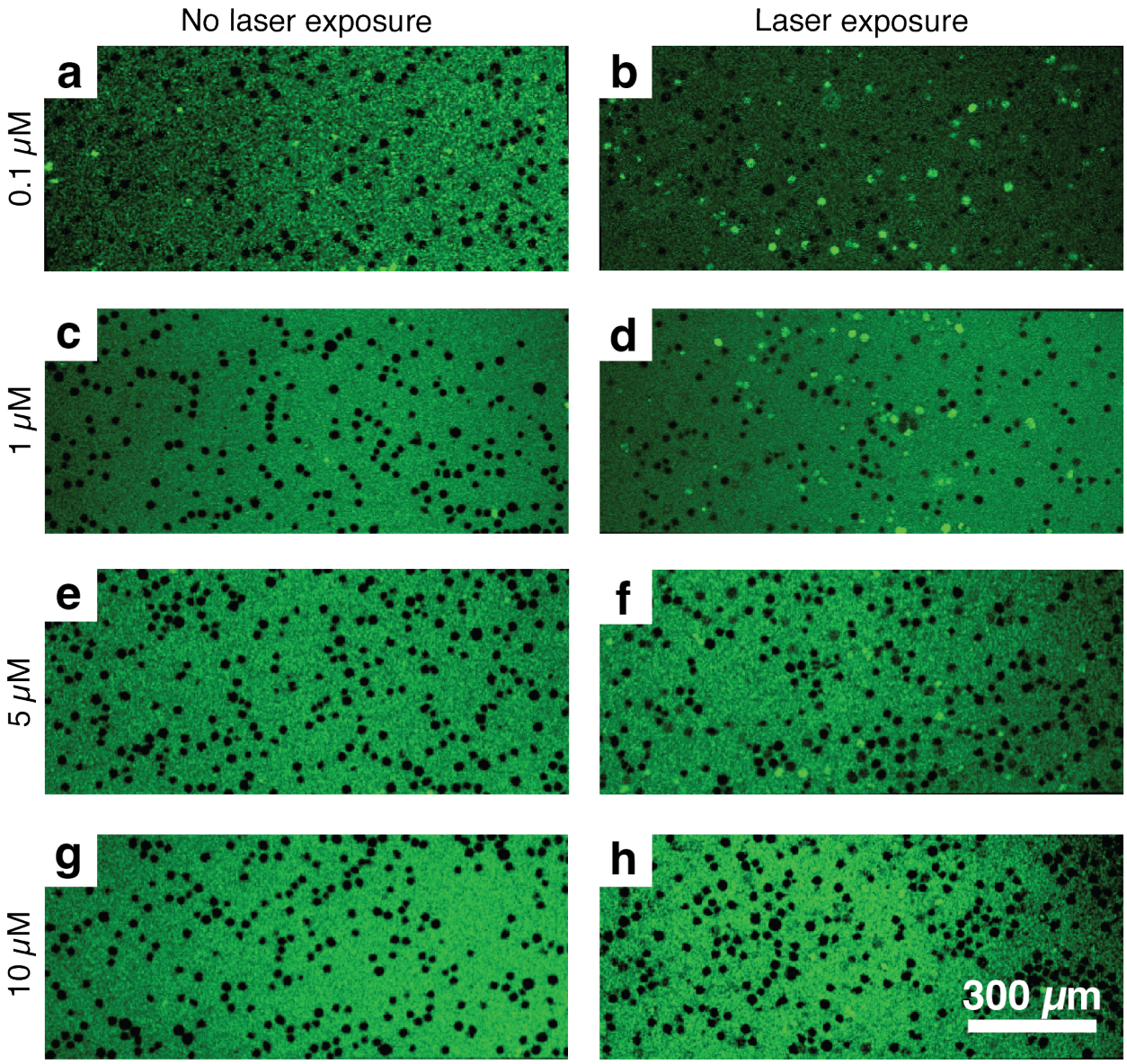

Figure 5.19: *Fluorescence images of K562 in 12 μm height chamber where cells in the left column have not been laser irradiated and the cells in the images in the right column have been laser irradiated at a fluence of 55 mJ/cm² with 8 pulses to each cell. (a) and (b) show 0.1 μM of siRNA in the medium surrounding the cells, (c) and (d) show 1 μM, (e) and (f) show 5 μM, and (g) and (h) show 10μM. The imaging software gain and confocal excitation voltage are not the same for the four sets due to the different concentrations and thus different amount of fluorescence emission that can be detected.*

5.4 Conclusions

This chapter has covered two configurations of the carbon black-PDMS composite material: as a substrate for adherent cells to grow on and as a microcuvette chamber for suspension cells. For the substrates, HeLa cells were grown, and fluorescence microscopy and image analysis were done to gain a quantitative understanding of the effects of many variables on viability and efficiency. The variables of interest that were explored were the concentration of carbon black in PDMS, patterning the carbon black-PDMS, replacing carbon black with titanium dioxide microparticles, fluence of laser irradiation, and number of laser pulses each cell experiences consecutively. There is no significant difference in viability and efficiency between pyramid-patterned carbon black-PDMS and flat carbon black-PDMS. As the concentration of carbon black is increased in the PDMS substrates, delivery efficiency did not change much but the viability went down. As the laser irradiation fluence is increased, the delivery rate goes up but then dips back down as the viability goes down with increasing laser fluence. However, this can be remedied by decreasing the laser fluence but increasing the number of pulses each cell experiences and delivery rate is increased without significant decrease in viability.

Although the post-treatment viability of the cells is lower than for the microcuvette chamber device, the carbon black-PDMS provides a feature that the chambers do not – spatial and temporal selectivity of multiple types of cargo that are delivered. The ability to create patterns in a petri dish of which cells have what kinds of cargoes at what time points can be accomplished with laser-irradiated substrate devices may be useful for cell biology applications. This feature can be used by many laser-induced delivery techniques.[142] While the viability rate of the carbon black-PDMS is relatively low compared to the metal nanostructures, the viability rate of the cells treated on TiO2-PDMS is quite high. TiO2 itself is non-absorbent at 1064 nm but may scatter laser light,

which is redistributed within the PDMS, cell membrane, or even into the cytoplasm. This non-absorbent material must be investigated further to understand the physical mechanisms that allow for cell membrane permeation if heating, or pressure waves, are not detected. An added benefit of using TiO2 microparticles in a device is also its extreme biocompatibility and it is already a prevalent material in a lot of human body interfaces, such as toothpaste and sunscreen.[143] Interestingly, if the TiO2-PDMS are used in the microcuvette chamber device, there is no delivery. This may imply that the way and configuration an adherent cell is naturally grown to the TiO2-PDMS surface has a role in the cell membrane perturbation mechanism.

The microfabrication and application of carbon black-PDMS in the microcuvette chamber form demonstrates the versatility in the composite material. It also has relative ease in fabrication compared to the metal nanostructures which would require multiple additional steps and costs in fabricating if they were to be integrated in a similar microfluidic configuration. Interestingly, when the K562 suspension cells are treated in the chamber devices, the viability shows no change compared to the control cells that have neither been loaded into a device nor laser irradiated. As the concentration of carbon black in the PDMS is increased, the delivery rate also increases without affecting viability. However, if the laser-irradiation fluence is very high, cells appear to get stuck in the chamber and cannot be ejected out. Since they cannot be retrieved, it is difficult to check the viability of them and it is also not a realistic way to proceed because the cells cannot be recovered. Thus, despite seeing cargo delivery to more cells at higher laser fluences, we operate at a fluence where we do not see bubbles in the chambers and are able to properly eject the cells out for further analysis and applications. This may be remedied with changes in chamber design and geometry so the cells may be easier to flow out of the chambers when extra media is injected in. For example, troughs could be made by the walls of the chamber so the cells that may be stuck along the walls

can have an easier time being ejected. Because so many cells are being treated at once in the microcuvette chambers and the suspension cells are easier to analyze, we depend on flow cytometry to verify viability and delivery.

For the microcuvette chambers, the effect chamber height had on delivery rate was also studied. We saw great delivery rate with chambers of 10 and 12 μm height, but huge decrease in delivery with 15 and 25 μm chambers. Since the diameter of a K562 cell is about 12.3 μm, it appears that it is necessary for the cells to be in direct contact with the carbon black-PDMS for delivery to occur. And when the cells are essentially "squeezed" while in the 10 μm chambers, either the pressure or the increased surface area of the cell membrane touching the carbon black-PDMS are contributing to the increase in delivery rate.

Like other laser-enabled delivery methods, discussed in previous chapters we see a higher rate of delivery of smaller cargo than bigger cargo due to passive diffusion. However, when we have fluorescently tagged siRNA in the medium during laser irradiation, they are delivered to more cells than when a smaller molecular weight neutrally charged cargo is in the medium. Not only is the percentage of delivered to cells out of treated cells higher, but the cells also that have siRNA in the cytoplasm seem to have a higher concentration than in the medium surrounding the cell. Based on passive diffusion and electrostatic interaction of the negatively charged genetic material (as opposed to neutrally charged polysaccharide Dextran molecules) and negatively charged cell membrane lipid bilayer, there should not be a higher rate of delivery of siRNA than Dextran 10kDa. There is perhaps another stronger force that is allowing the siRNA to be pulled in, such as the chemical potential of siRNA being lowered once they move into the cytoplasm. This is against the concentration gradient which drives passive diffusion and against the membrane charge electrostatics. Perhaps there are many siRNA-binding proteins or other interactions inside the

cytoplasm that drives the cargo-uptake. For example, environmental stress can cause a cell to react with a lot of physiological changes and create cytoplasm reorganization. The reorganization can cause stress-activated RNA-protein granules to form that may affect cargo is interacting with the cells upon cell membrane permeability due to heat or pressure change.[144] Although understanding the effect is beyond the scope of this chapter, it is worth studying in the future as cargo delivered with carbon black-PDMS is evolved from model cargo like calcein green and FITC-Dextran to functional proteins like RNA to modulate pathways inside the cells.

Chapter 6

Conclusions

6.1 Summary

In this thesis, laser-irradiated materials are explored for intracellular cargo delivery with the following features in mind: high throughput and treatment speed, high cell viability, and high efficiency in cargo delivery. Fluorescence microscopy and flow cytometry are used to quantify delivery rate and viability. The material effects of nanosecond pulsed-laser irradiation of different materials have been investigated using scanning electron microscopy and optical profilometry, and the physical effects of the irradiation in an aqueous environment are studied using hydrophone measurements. Biologically interesting cells, such as primary heart valve cells, were used and successfully delivered to. Large cargoes of up to 2000 kDa were delivered to cells, and siRNA was successfully delivered to suspension cell types using laser-irradiated microcuvette chambers.

In Chapter 3, thermoplasmonic metal structures are fabricated and used for cargo delivery to adherent cells such as HeLa and myoblast cells. An 11-nanosecond pulsed-laser excitation at 1064 nm optical set-up is described, allowing for raster scanning cells on substrates to produce high-throughput results. The pulse repetition rate is 50 Hz and based on the raster scanning speed and beam size, the pulse number each cell experiences can vary. For the thermoplasmonic substrates, each cell experiences 6 pulses.

First, the chapter covers the cleanroom nanofabrication protocol for the large-area (14 x 14 mm) thin continuous-film gold pyramid array. The protocol uses a template-stripping technique to create reproducible samples at low-cost that can be applicable for larger-scale experiments. No gold residue or fragmentation are detected, bypassing the need for nanoparticles for

thermoplasmonic laser-induced delivery. Laser irradiation is used to form hotspots at the apex of the structure 50 nm of gold. These hotspots are required for localized poration of the cell membrane when a cell is cultured direction onto the gold, which is an inert biocompatible material. The tips of the pyramids reach a high enough temperature for bubble formation to porate the cell. Cargoes ranging in size from 0.623 to 2000 kDa are delivered to HeLa cells, and the size are comparable to biologically relevant cargoes such as proteins, antibodies, and gene-editing technology (CRISPR-cas9). Flow cytometry and image analysis of fluorescent microscopy show that there is a correlation between laser fluence and cell behavior: cargo update delivery rate and cell survival viability rate. Higher laser fluences can cause the cells to die, resulting in both low cell viability and cargo delivery because the latter is dependent on cells surviving the process. However, at the optimal laser fluence of 54 mJ/cm^2, the gold pyramids are able to deliver calcein green (0.623 kDa) membrane-impermeable green fluorescent dye at a rate of 95% with a viability of 98%. FITC-Dextran 150 kDa can be delivered at a rate of 70% with the same rate of viability at the optimal laser fluence. Pore dynamics of picosecond laser irrated gold pyramids for myoblast C2C12 cells are also studied. Fluoresence microscopy and image analysis shows that cells membrane are healed by 1 minute after laser-irradiation and based on the diffusivity of the cargo intake and outflow, the pore radius is about 20 nm, which is comparable to the Stokes radius of cargo that is delivered.

Titanium nitride (TiN) micropyramids of different orientations are also fabricated and used for intracellular cargo delivery. TiN is similar to gold in that it also exhibits plasmonic behavior, but has stronger mechanical features such as a higher Mohs hardness rating and a high melting temperature that is twice as that of gold's. The robust material may be of interest for more intensive usage of laser-irradiated thermoplasmonic nanostructures. A lower range of laser fluence is used to find peak laser delivery conditions: for the inverted pyramids, the fluence is at 16.5 mJ/cm^2 and

produces a delivery efficiency rate of 83% and viability of 95%. For the upright pyramids, in the same configuration as the gold pyramids, the optimal laser fluence is at 15.5 mJ/cm^2 and the delivery rate is only 66% with a viability of 67%.

Finally, the 3rd chapter covers titanium nanocavities, or inverse opal, structures that also produces a thermoplasmonic effect when irradiated with the nanosecond NIR laser. The titanium nanocavities use a self-assembly fabrication method which negate the use of a cleanroom and lowers the fabrication costs. The titanium structure also uses an optimal fluence of 12.5 mJ/cm^2, which is almost five times lower than the fluence required for the gold pyramids. A delivery efficiency of 78% is achieved for calcein green to HeLa cells while the viability is 87%. The lower rates compared the gold pyramids may be due to irregularities in the self-assembled titanium nanocavities and higher number of features that produce localized heating underneath each cell. While the three materials and substrate types that are covered in the chapter are highly efficient and has high cell viability, all materials are two-dimensional and restricts treatment to adherent cell types. The materials are also nanostructured which requires large arrays of patterning to be incorporated in the fabrication preparation. Gold and titanium are also both thin-film metals and thus are not mechanically robust. In addition, some sensitive cell types such as embryonic stem cells and induced pluripotent stem cells would not be able to grow on the patterned metal surface and would require a coating. Thus, more biocompatible materials that is easily integrated into devices and is less expensive should be investigated. The subsequent chapter explores using polymer in place of metals for laser-irradiated cargo delivery.

In Chapter 4, proof-of-concept experiments are showed with laser-irradiated polyvinyl materials. The polyvinyl is off-the-shelf electrical tape with the sticky side down in a petri-dish for *in vitro* cargo delivery (the adhesive have no role to play in the method). The black polyvinyl tape

absorbs strongly at 1064 nm and produces pressure waves that are measured with a needle hydrophone set up. The measurements show a correlation in magnitude of impulse and the laser fluence that is irradiated. The measurements also show a correlation in the higher laser fluence range with the surface roughness change, measured and analyzed with optical profilometry. The higher laser fluence range causes the surface roughness to increase and the pressure wave impulse magnitude to decrease, implying that the material deforms and reaches around 170 to 180 °C, which is the melting temperature of polyvinyl chloride. The corresponding laser fluence these effects start taking place is around 65 mJ/cm^2, which is when there is a significant decrease in cell viability. The laser fluence needed is a lot higher, perhaps because the polyvinyl material is a bulk material and is not conductive and depends on photothermal interactions between the absorbent black polyvinyl and the nanosecond pulsed laser. A delivery rate of 40% is achieved for calcein green with a low viability of 60%. Cargo can also be delivered to primary human aortic valve interstitials cells, which grows regularly on the polyvinyl surface. Unlike the gold pyramids, where we observe pores in HeLa cells to close after 1 minute, the laser-irradiated polyvinyl appears to create pores in the cell membrane that take several minutes to heal. This may contribute to the lower viability rate. The work shown in this chapter opens the door to particle-embedded polymer material to be integrated into delivery platforms beyond 2-dimensional substrates, which is covered in the following chapter.

In Chapter 5, particle embedded PDMS is developed. Carbon black nanoparticles is light absorbent at 1064 nm and is an abundant and low-cost material. PDMS is a thermosetting polymer that is made up polymer chains that cross link, thus allowing for the material to reach high temperature without causing permanent deformation. PDMS is a common silicon-based organic polymer that is often used for soft lithography fabrication for microfluidic devices. Thus, the

particle embedded PDMS can be incorporated into microfluidic lab-on-chip experiments that can be scaled up, have controlled sterile environment, and lowers the liquid volume of experiments. The chapter covers cargo delivery with using carbon black-PDMS as a 2-dimensional substrate as in prior chapter and also expands the cargo delivery treatment to suspension cells, which is an important category of cells that blood and immune cells fall under. The laser parameter of number of pulses a cell experiences is also explored. The chapter shows that by lowering laser fluence and increasing the number of pulses, an increase in delivery rate and minimal decrease in cell viability can be observed. The 2-dimensional carbon black-PDMS substrates also show spatially and temporally selective multiple-cargo delivery, which is an inherent feature of substrate-based laser-irradiated cargo delivery. Two different laser scan patterns at different time points while different cargo are present during the respective time points show that cells in a petri dish population can be selected to have different cargo in the cytoplasm at different time points, which may be of interest for cell biology experiments. Titanium dioxide is also embedded in PDMS, showing cargo delivery similar to the white polyvinyl substrate in the prior chapter. Creating nanopyramid surface structure on the carbon black-PDMS substrate creates no change in cargo delivery or cell death. The correlation of carbon black concentration in PDMS and cell viability is explored and analyzed for both the 2-dimensional carbon black-PDMS substrates and also for the 3-dimensional microcuvette microchambers.

Finally, the 5th chapter covers high-throughput cargo delivery in the kDa-range to K562, a suspension cell line, using carbon black embedded PDMS microcuvette microchambers that are made using soft lithography techniques. The large-scale, highly reproducible photolithography procedure is covered and chambers of 10 and 12 μm heights are created to force the cell suspension into a monolayer that is in direct contact with the carbon black embedded PDMS side. The liquid

volume to treat at least 200,000 cells is decreased from hundreds of μL that is needed for substrate devices in a petri dish to only a few μL as the microchamber decrease the operating volume of cells in suspension with cargo. This technique also skips having to wait for cells to grow and adhere to substrates overnight in the cell culture protocol. Flow cytometry is used to study delivery rate and viability. Unlike the carbon black PDMS substrate devices, the cell viability for the mirocuvette chambers is nearly at 100%, matching the viability rate of cells that are in suspension without being loaded into the chamber and without any laser exposure at all. Fluorescence microscopy shows that at higher laser fluence, cargo is delivered to more cells but ejecting the cells become a problem. Thus, the highest fluence at which cells can be ejected, at 50 mJ/cm^2, is used to investigate the delivery of larger functional cargoes such as siRNA. Higher delivery rates without decrease in viability is shown with chambers of 10 μm height than 12 μm height. Chambers with 15 and 25 μm height show very little cargo delivery. The cell deformation from the chamber height is also measured and analyzed. 48% delivery of calcein green is achieved with 5% carbon black-PDMS microcuvettes of 10 μm height with nearly 100% cell viability. 25% delivery of 70 kDa FITC-Dextran is also achieved with little to no cell death. Fluorescently tagged siRNA is delivered to the K562 suspension cells and are analyzed using flow cytometry and fluorescent microscopy. The concentration of siRNA in the media during laser-irradiation is also investigated. When the cells are surrounded in a media containing siRNA at a concentration of 5 μM, 45% of the cells uptake the siRNA which is much higher than the delivery rate of 10 kDa FITC-Dextran (35%) which is of comparable size. A higher concentration of siRNA inside the cell after laser-irradiation compared to the surrounding medium is also observed through fluorescence microscopy, which suggests that more than passive diffusion is at play for the cargo delivery upon cell membrane disruption. The carbon black-PDMS material allows for the delivery of functional

proteins to suspension cells, and adherent cells when they are treated with trypsin to become suspended in media.

6.2 Future Directions

The gold nanopyramid structures can also allow for functionalized for different applications for various cell types, and due to its high delivery rates for larger cargoes without much cell death, the platform would be a viable application for *in vitro* cell biology experiments that desire spatially and temporally selective cargo delivery with high delivery and viability rates. Further fabrication and poration experiments can be investigated by varying the nanopyramid size and pitch so the effect of average number of hot spots underneath each cell can be investigated. The localized heating effect at the pyramid tips and the hypothesized cavitation bubbles can also be measured and analyzed using a pump-probe set-up. A galvanometric scanning mirror assembly and telecentric lens can also be incorporated in the nanosecond pulsed-laser set up, replacing the raster scanning stage, to increase the laser scanning procedure.

While the black polyvinyl material induced cargo delivery and has pressure waves and surface roughness changes that correlate with laser irradiation, white polyvinyl exhibit no pressure waves, no surface roughness changes that point to temperature increase, a negligible amount of absorption at 1064 nm, but still induce cargo delivery with very little cell death. The laser-material interactions between nanosecond pulsed laser and metal oxides, such as titanium dioxide, may be further explored in the future.

A light-activated polymer material's ability to deliver payloads across a cellular membrane relies on mechanical perturbations, giving such materials the potential to deliver a wide range of cargoes to various cell types. It is critical to characterize the material properties in combination with laser-activation to determine the biocompatibility and applicability of the materials for

different, sensitive cell types. Building a strong design and understanding of new biomaterials would enable the creation of materials that are triggered in a non-invasive manner using light-activation. This material would change the biological fate of cells in a patient's body with improved drug delivery processes. A nontoxic, efficient, and scalable technique would offer a novel approach to the advancement of nanomedicine and the study of laser-material-cell interaction. Carbon black can also be replaced with other highly light-absorbing particles, such as melanin, that are more biocompatible. Photoresponsive hydrogels can also be used in place of PDMS for cargo delivery. The microcuvette chambers can also be reconfigured to allow for microfluidic lab-on-chip applications.

On the front of cell viability, longer term biocompatibility and post-treatment survival and proliferation can also be explored for the carbon black-PDMS, similar to the post-24- and 48-hour proliferation verification done for the gold pyramids. Clonogentic assays can also be conducted. More biologically relevant cells other than primary heart valve cells that were investigated in this thesis, such as stem cells and neurons, can also be investigated as the substrate-based method has evolved from metal nanostructures to polymers that can promote better cell adhesion and growth in a petri dish. Most of the experiments covered in this thesis using neutrally charged calcein green and dextran molecules of varying molecular weights to model the delivery of functional proteins such as nucleic acids. The delivery of siRNA to K562 cells in this thesis also shows that there may be more than the passive diffusion initially hypothesized that drives cargo delivery, and different biological experiments can be conducted with the laser-irradiated cargo delivery because the delivery is dependent on the physical disruption of the cell membrane – leading to the platforms to potentially be applied to more diverse cell lines and versatile cargo types.

This thesis covers gold nanopyramids, titanium nitride nanopyramids, titanium nanocavities, pigmented polyvinyl, and particle embedded PDMS as materials for laser-irradiated intracellular cargo delivery techniques. The light-driven cell membrane poration experiments opens the door to further nanomedicine. The laser-matter interactions observed, or not observed in the case of the white and titanium dioxide polymers, also draws further investigation to better understand the physical effects that can drive cell membrane poration for intracellular cargo delivery.

Appendix

```
for bb = 1:1:length(filenumbers)
    figure(bb)
    filenumber = filenumbers(bb);
    plot(ds.timens{filenumber},ds.pressurempa{filenumber})
    hold on
    [maxval,maxindex] = max(ds.pressurempa{filenumber});
    maxtime = ds.timens{filenumber}(maxindex,1);
    plot(maxtime,maxval,'o')

plot(ds.timens{filenumber},ds.floor{filenumber}.*ones(length(ds.timens{filenu
mber})))
    risept = (0.1.*(maxval-ds.floor{filenumber})+ds.floor{filenumber});
    plot(ds.timens{filenumber},risept.*ones(length(ds.timens{filenumber})))

    [intersectpt,intersectindex]                                          =
min(abs(ds.pressurempa{filenumber}(maxindex-100:maxindex) - risept));
    intersectindex = intersectindex + maxindex - 100 - 1;
    intersect                                                             =
[ds.timens{filenumber}(intersectindex),ds.pressurempa{filenumber}(intersectin
dex),intersectindex];
    [intersectpt,intersectindex]                                          =
min(abs(ds.pressurempa{filenumber}(maxindex:maxindex+100) - risept));
    intersectindex = intersectindex+maxindex-1;
    intersect                                                             =
[intersect;ds.timens{filenumber}(intersectindex),ds.pressurempa{filenumber}(i
ntersectindex),intersectindex];
    plot(intersect(1,1),intersect(1,2),'rs')
    plot(intersect(2,1),intersect(2,2),'bs')
```

```
    ds.impulse{filenumber}                                                    =
trapz(ds.timens{filenumber}(intersect(1,3):intersect(2,3)),ds.pressurempa{fil
enumber}(intersect(1,3):intersect(2,3))-ds.floor{filenumber})

    ds.impulseuncertainty{filenumber}    =    (4/(6*sqrt(6)))*(intersect(2,1)-
intersect(1,1))
end
```

References

(1) Henrietta Lacks: science must right a historical wrong. Henrietta. *Nature* **2020**, *585* (7), 39–40. https://doi.org/10.1353/ccr.2021.0038.

(2) Townes, C.H., 2002. *How the laser happened: Adventures of a scientist*. Oxford University Press.

(3) Dutta Majumdar, J.; Manna, I. Laser Material Processing. *Int. Mater. Rev.* **2011**, *56* (5–6), 341–388. https://doi.org/10.1179/1743280411Y.0000000003.

(4) Peters, A.; Chung, K. Y.; Chu, S. Measurement of Gravitational Acceleration by Dropping Atoms. *Nature* **1999**, *400* (6747), 849–852. https://doi.org/10.1038/23655.

(5) Peng, Q.; Juzeniene, A.; Chen, J.; Svaasand, L. O.; Warloe, T.; Giercksky, K. E.; Moan, J. Lasers in Medicine. *Reports Prog. Phys.* **2008**, *71* (5). https://doi.org/10.1088/0034-4885/71/5/056701.

(6) Matthäus, C.; Bird, B.; Miljković, M.; Chernenko, T.; Romeo, M.; Diem, M. Infrared and Raman Microscopy in Cell Biology. *Methods Cell Biol.* **2008**, *89* (08), 275–308. https://doi.org/10.1016/S0091-679X(08)00610-9.

(7) Langer, R. New Methods of Drug Delivery. *Science* **1990**, *249* (4976), 1527–1533. https://doi.org/10.1126/science.2218494.

(8) Nicolas, J.; Mura, S.; Brambilla, D.; Mackiewicz, N.; Couvreur, P. Design, Functionalization Strategies and Biomedical Applications of Targeted Biodegradable/Biocompatible Polymer-Based Nanocarriers for Drug Delivery. *Chem. Soc. Rev.* **2013**, *42* (3), 1147–1235. https://doi.org/10.1039/c2cs35265f.

(9) Langer, R. Drug Delivery and Targeting. *Nature*. 1998, pp 5–10. https://doi.org/10.1517/14728222.2.1.145.

(10) Wagner, V.; Dullaart, A.; Bock, A.; Zweck, A. The Emerging Nanomedicine Landscape. *Nat. Biotechnol.* **2006**, *24* (10), 1211–1217.

(11) Kim, B. Y. S.; Rutka, J. T.; Chan, W. C. W. Nanomedicine. *N. Engl. J. Med.* **2010**, *363* (25), 2434–2443. https://doi.org/10.1056/NEJMra0912273.

(12) Sanhai, W. R.; Sakamoto, J. H.; Canady, R.; Ferrari, M. Seven Challenges for Nanomedicine. *Nat. Nanotechnol.* **2008**, *3* (5), 242–244. https://doi.org/10.1038/nnano.2008.114.

(13) Chauhan, V. P.; Jain, R. K. Strategies for Advancing Cancer Nanomedicine. *Nat. Mater.* **2013**, *70* (4), 646–656. https://doi.org/10.1002/ana.22528.Toll-like.

(14) Morshedi Rad, D.; Alsadat Rad, M.; Razavi Bazaz, S.; Kashaninejad, N.; Jin, D.; Ebrahimi Warkiani, M. A Comprehensive Review on Intracellular Delivery. *Adv. Mater.* **2021**, *33* (13), 1–36. https://doi.org/10.1002/adma.202005363.

(15) Al-Dosari, M. S.; Gao, X. Nonviral Gene Delivery: Principle, Limitations, and Recent Progress. *AAPS J.* **2009**, *11* (4), 671–681. https://doi.org/10.1208/s12248-009-9143-y.

(16) Phillips, a J. The Challenge of Gene Therapy and DNA Delivery. *J. Pharm. Pharmacol.* **2001**, *53* (9), 1169–1174. https://doi.org/10.1211/0022357011776603.

(17) Patil, S. D.; Rhodes, D. G.; Burgess, D. J. DNA-Based Therapeutics and DNA Delivery Systems: A Comprehensive Review. *AAPS J.* **2005**, *7* (1), E61–E77. https://doi.org/10.1208/aapsj070109.

(18) Mora-huertas, C. E.; Fessi, H.; Elaissari, A. Polymer-Based Nanocapsules for Drug Delivery. *Int. J. Pharm.* **2010**, *385*, 113–142. https://doi.org/10.1016/j.ijpharm.2009.10.018.

(19) Ganta, S.; Devalapally, H.; Shahiwala, A.; Amiji, M. A Review of Stimuli-Responsive

Nanocarriers for Drug and Gene Delivery. *J. Control. Release* **2008**, *126* (3), 187–204. https://doi.org/10.1016/j.jconrel.2007.12.017.

(20) Marti, G.; Ferguson, M.; Wang, J.; Byrnes, C.; Dieb, R.; Qaiser, R.; Bonde, P.; Duncan, M. D.; Harmon, J. W. Electroporative Transfection with KGF-1 DNA Improves Wound Healing in a Diabetic Mouse Model. *Gene Ther.* **2004**, *11* (24), 1780–1785. https://doi.org/10.1038/sj.gt.3302383.

(21) Courvoisier, S.; Saklayen, N.; Huber, M.; Chen, J.; Diebold, E. D.; Bonacina, L.; Wolf, J. P.; Mazur, E. Plasmonic Tipless Pyramid Arrays for Cell Poration. *Nano Lett* **2015**, *15* (7), 4461–4466. https://doi.org/10.1021/acs.nanolett.5b01697.

(22) Saklayen, N.; Huber, M.; Madrid, M.; Nuzzo, V.; Vulis, D. I.; Shen, W.; Nelson, J.; McClelland, A. A.; Heisterkamp, A.; Mazur, E. Intracellular Delivery Using Nanosecond-Laser Excitation of Large-Area Plasmonic Substrate. *ACS Nano* **2017**, *11* (4), 3671–3680. https://doi.org/10.1021/acsnano.6b08162.

(23) Saklayen, N.; Kalies, S.; Madrid, M.; Nuzzo, V.; Huber, M.; Shen, W.; Sinanan-Singh, J.; Heinemann, D.; Heisterkamp, A.; Mazur, E. Analysis of Poration-Induced Changes in Cells from Laser-Activated Plasmonic Substrates. *Biomed. Opt. Express* **2017**, *8* (10), 437–444. https://doi.org/10.1364/BOE.8.004756.

(24) Chen, J.; Saklayen, N.; Courvoisier, S.; Ni, X.; Mazur, E. Dynamics of Transient Microbubbles Generated by Fs-Laser Irradiation of Plasmonic Micropyramids. *Appl. Phys. Lett.* **2017**, *153102*. https://doi.org/10.1063/1.4979886.

(25) Ma, H.; Marti-Gutierrez, N.; Park, S. W.; Wu, J.; Lee, Y.; Suzuki, K.; Koski, A.; Ji, D.; Hayama, T.; Ahmed, R.; Darby, H.; Van Dyken, C.; Li, Y.; Kang, E.; Park, A. R.; Kim, D.; Kim, S. T.; Gong, J.; Gu, Y.; Xu, X.; Battaglia, D.; Krieg, S. A.; Lee, D. M.; Wu, D. H.;

Wolf, D. P.; Heitner, S. B.; Belmonte, J. C. I.; Amato, P.; Kim, J. S.; Kaul, S.; Mitalipov, S. Correction of a Pathogenic Gene Mutation in Human Embryos. *Nature* **2017**, *548* (7668), 413–419. https://doi.org/10.1038/nature23305.

(26) Stewart, M. P.; Langer, R.; Jensen, K. F. Intracellular Delivery by Membrane Disruption: Mechanisms, Strategies, and Concepts. *Chem. Rev.* **2018**, *118* (16), 7409–7531. https://doi.org/10.1021/acs.chemrev.7b00678.

(27) Lichtenberg, D.; Ahyayauch, H.; Goñi, F. M. The Mechanism of Detergent Solubilization of Lipid Bilayers. *Biophys. J.* **2013**, *105* (2), 289–299. https://doi.org/10.1016/j.bpj.2013.06.007.

(28) Shi, J.; Ma, Y.; Zhu, J.; Chen, Y.; Sun, Y.; Yao, Y.; Yang, Z.; Xie, J. A Review on Electroporation-Based Intracellular Delivery. *Molecules* **2018**, *23* (11). https://doi.org/10.3390/molecules23113044.

(29) Rems, L.; Tang, X.; Zhao, F.; Pérez-conesa, S.; Testa, I.; Delemotte, L. Identification of Electroporation Sites in the Complex Lipid Organization of the Plasma Membrane. *Elife* **2021**, 1–27.

(30) Kotnik, T.; Rems, L.; Tarek, M.; Miklavčič, D. Membrane Electroporation and Electropermeabilization: Mechanisms and Models. *Annu. Rev. Biophys.* **2019**, *48* (1), 63–91. https://doi.org/10.1146/annurev-biophys-052118-115451.

(31) Abidor, I. G.; Li, L. H.; Hui, S. W. Studies of Cell Pellets: II. Osmotic Properties, Electroporation, and Related Phenomena: Membrane Interactions. *Biophys. J.* **1994**, *67* (1), 427–435. https://doi.org/10.1016/S0006-3495(94)80498-9.

(32) Kano, F.; Nakatsu, D.; Noguchi, Y.; Yamamoto, A.; Murata, M. A Resealed-Cell System for Analyzing Pathogenic Intracellular Events: Perturbation of Endocytic Pathways under

Diabetic Conditions. *PLoS One* **2012**, *7* (8). https://doi.org/10.1371/journal.pone.0044127.

(33) Fu, A.; Tang, R.; Hardie, J.; Farkas, M. E.; Rotello, V. M. Promises and Pitfalls of Intracellular Delivery of Proteins. *Bioconjug. Chem.* **2014**, *25* (9), 1602–1608. https://doi.org/10.1021/bc500320j.

(34) Mintzer, M. A.; Simanek, E. E. Nonviral Vectors for Gene Delivery. *Chem. Rev.* **2009**, *109* (2), 259–302. https://doi.org/10.1021/cr800409e.

(35) Hapala, I. Breaking the Barrier: Methods for Reversible Permeabilization of Cellular Membranes. *Crit. Rev. Biotechnol.* **1997**, *17* (2), 105–122. https://doi.org/10.3109/07388559709146609.

(36) Stephens, D. J.; Pepperkok, R. The Many Ways to Cross the Plasma Membrane. *Proc. Natl. Acad. Sci. U. S. A.* **2001**, *98* (8), 4295–4298. https://doi.org/10.1073/pnas.081065198.

(37) Keyhani, K.; Guzmán, H. R.; Parsons, A.; Lewis, T. N.; Prausnitz, M. R. Intracellular Drug Delivery Using Low-Frequency Ultrasound: Quantification of Molecular Uptake and Cell Viability. *Pharm. Res.* **2001**, *18* (11), 1514–1520. https://doi.org/10.1023/A:1013066027759.

(38) Mitragotri, S.; A, B. Healing Sound: The Use of Ultrasound in Drug Delivery and Other Therapeutic Applications. *Nat. Rev. Drug Discov.* **2005**, *4* (March), 255–260. https://doi.org/10.1038/nrd1662.

(39) Mitragotri, S.; Blankschtein, D.; Langer, R. Ultrasound-Mediated Transdermal Protein Delivery. *Science (80-.).* **1995**, *269* (5225), 850–853.

(40) Oberli, M. A.; Schoellhammer, C. M.; Langer, R.; Blankschtein, D. Ultrasound-Enhanced Transdermal Delivery: Recent Advances and Future Challenges. *Ther. Deliv.* **2014**, *5* (7), 843–857. https://doi.org/doi:10.4155/tde.14.32.

(41) Qiu, Y.; Zhang, C.; Tu, J.; Zhang, D. Microbubble-Induced Sonoporation Involved in Ultrasound-Mediated DNA Transfection in Vitro at Low Acoustic Pressures. *J. Biomech.* **2012**, *45* (8), 1339–1345. https://doi.org/10.1016/j.jbiomech.2012.03.011.

(42) Marmottant, P.; Hilgenfeldt, S. Controlled Vesicle Deformation and Lysis by Single Oscillating Bubbles. *Nature* **2003**, *423* (6936), 151–153. https://doi.org/10.1038/nature01592.

(43) Liu, Y.; Yan, J.; Prausnitz, M. R. Can Ultrasound Enable Efficient Intracellular Uptake of Molecules? A Retrospective Literature Review and Analysis. *Ultrasound Med. Biol.* **2012**, *38* (5), 876–888. https://doi.org/10.1016/j.ultrasmedbio.2012.01.006.

(44) Juffermans, L. J. M.; Dijkmans, P. A.; Musters, R. J. P.; Visser, C. A.; Kamp, O. Transient Permeabilization of Cell Membranes by Ultrasound-Exposed Microbubbles Is Related to Formation of Hydrogen Peroxide. *Am. J. Physiol. - Hear. Circ. Physiol.* **2006**, *291* (4), 1595–1601. https://doi.org/10.1152/ajpheart.01120.2005.

(45) Kodama, T.; Hamblin, M. R.; Doukas, A. G. Cytoplasmic Molecular Delivery with Shock Waves: Importance of Impulse. *Biophys. J.* **2000**, *79* (4), 1821–1832. https://doi.org/10.1016/S0006-3495(00)76432-0.

(46) Zarnitsyn, V.; Rostad, C. A.; Prausnitz, M. R. Modeling Transmembrane Transport through Cell Membrane Wounds Created by Acoustic Cavitation. *Biophys. J.* **2008**, *95* (9), 4124–4138. https://doi.org/10.1529/biophysj.108.131664.

(47) Sharei, A.; Zoldan, J.; Adamo, A.; Sim, W. Y.; Cho, N.; Jackson, E.; Mao, S.; Schneider, S.; Han, M.-J.; Lytton-Jean, A.; Basto, P. A.; Jhunjhunwala, S.; Lee, J.; Heller, D. A.; Kang, J. W.; Hartoularos, G. C.; Kim, K.-S.; Anderson, D. G.; Langer, R.; Jensen, K. F. A Vector-Free Microfluidic Platform for Intracellular Delivery. *Proc. Natl. Acad. Sci.* **2013**, *110* (6),

2082–2087. https://doi.org/10.1073/pnas.1218705110.

(48) Sharei, A.; Cho, N.; Mao, S.; Jackson, E.; Poceviciute, R.; Adamo, A.; Zoldan, J.; Langer, R.; Jensen, K. F. Cell Squeezing as a Robust, Microfluidic Intracellular Delivery Platform. *J. Vis. Exp.* **2013**, No. 81, 1–6. https://doi.org/10.3791/50980.

(49) Versaevel, M.; Riaz, M.; Grevesse, T.; Gabriele, S. Cell Confinement: Putting the Squeeze on the Nucleus. *Soft Matter* **2013**, *9* (29), 6665–6676. https://doi.org/10.1039/c3sm00147d.

(50) Lee, J.; Sharei, A.; Sim, W. Y.; Adamo, A.; Langer, R.; Jensen, K. F.; Bawendi, M. G. Non-Endocytic Delivery of Functional Engineered Nanoparticles into the Cytoplasm of Live Cells Using a Novel, High-Throughput Microfluidic Device. *Nano Lett.* **2012**, *12* (12), 6322–6327. https://doi.org/doi:10.1021/nl303421h.

(51) Ding, X.; Stewart, M. P.; Sharei, A.; Weaver, J. C.; Langer, R. S.; Jensen, K. F. High-Throughput Nuclear Delivery and Rapid Expression of DNA via Mechanical and Electrical Cell-Membrane Disruption. *Nat. Biomed. Eng.* **2017**, *1* (3), 1–7. https://doi.org/10.1038/s41551-017-0039.

(52) Raab, M.; Gentili, M.; De Belly, H.; Thiam, H. R.; Vargas, P.; Jimenez, A. J.; Lautenschlaeger, F.; Voituriez, R.; Lennon-Duménil, A. M.; Manel, N.; Piel, M. ESCRT III Repairs Nuclear Envelope Ruptures during Cell Migration to Limit DNA Damage and Cell Death. *Science (80-.).* **2016**, *352* (6283), 359–362. https://doi.org/10.1126/science.aad7611.

(53) Doudna, J. A.; Charpentier, E. The New Frontier of Genome Engineering with CRISPR-Cas9. *Science (80-.).* **2014**, *346* (6213). https://doi.org/10.1126/science.1258096.

(54) Elnathan, R.; Delalat, B.; Brodoceanu, D.; Alhmoud, H.; Harding, F. J.; Buehler, K.; Nelson, A.; Isa, L.; Kraus, T.; Voelcker, N. H. Maximizing Transfection Efficiency of

Vertically Aligned Silicon Nanowire Arrays. *Adv. Funct. Mater.* **2015**, *25* (46), 7215–7225. https://doi.org/10.1002/adfm.201503465.

(55) Mumm, F.; Beckwith, K. M.; Bonde, S.; Martinez, K. L.; Sikorski, P. A Transparent Nanowire-Based Cell Impalement Device Suitable for Detailed Cell-Nanowire Interaction Studies. *Small* **2013**, *9* (2), 263–272. https://doi.org/10.1002/smll.201201314.

(56) Davis, A. A.; Farrar, M. J.; Nishimura, N.; Jin, M. M.; Schaffer, C. B. Optoporation and Genetic Manipulation of Cells Using Femtosecond Laser Pulses. *Biophys. J.* **2013**, *105* (4), 862–871. https://doi.org/DOI 10.1016/j.bpj.2013.07.012.

(57) Stevenson, D.; Agate, B.; Tsampoula, X.; Fischer, P.; Brown, C. T. A.; Sibbett, W.; Riches, A.; Gunn-Moore, F.; Dholakia, K. Femtosecond Optical Transfection of Cells:Viability and Efficiency. *Opt. Express* **2006**, *14* (16), 7125. https://doi.org/10.1364/oe.14.007125.

(58) Vogel, A.; Noack, J.; Hüttman, G.; Paltauf, G. Mechanisms of Femtosecond Laser Nanosurgery of Cells and Tissues. *Appl. Phys. B Lasers Opt.* **2005**, *81* (8), 1015–1047. https://doi.org/10.1007/s00340-005-2036-6.

(59) Baumgart, J.; Humbert, L.; Boulais, ??tienne; Lachaine, R.; Lebrun, J. J.; Meunier, M. Off-Resonance Plasmonic Enhanced Femtosecond Laser Optoporation and Transfection of Cancer Cells. *Biomaterials* **2012**, *33* (7), 2345–2350. https://doi.org/10.1016/j.biomaterials.2011.11.062.

(60) Sengupta, A.; Kelly, S. C.; Dwivedi, N.; Thadhani, N.; Prausnitz, M. R. Efficient Intracellular Delivery of Molecules with High Cell Viability Using Nanosecond-Pulsed Laser-Activated Carbon Nanoparticles. *ACS Nano* **2014**, *8* (3), 2889–2899. https://doi.org/10.1021/nn500100x.

(61) Jain, P. K.; Huang, X.; El-Sayed, I. H.; El-Sayed, M. A. Review of Some Interesting Surface

Plasmon Resonance-Enhanced Properties of Noble Metal Nanoparticles and Their Applications to Biosystems. *Plasmonics* **2007**, *2* (3), 107–118. https://doi.org/10.1007/s11468-007-9031-1.

(62) Boulais, E.; Lachaine, R.; Hatef, a.; Meunier, M. Plasmonics for Pulsed-Laser Cell Nanosurgery: Fundamentals and Applications. *J. Photochem. Photobiol. C Photochem. Rev.* **2013**, *17*, 26–49. https://doi.org/10.1016/j.jphotochemrev.2013.06.001.

(63) Kalies, S.; Birr, T.; Heinemann, D.; Schomaker, M.; Ripken, T.; Heisterkamp, A.; Meyer, H. Enhancement of Extracellular Molecule Uptake in Plasmonic Laser Perforation. *J. Biophotonics* **2014**, *7* (7), 474–482. https://doi.org/10.1002/jbio.201200200.

(64) Schaeublin, N. M.; Braydich-Stolle, L. K.; Schrand, A. M.; Miller, J. M.; Hutchison, J.; Schlager, J. J.; Hussain, S. M. Surface Charge of Gold Nanoparticles Mediates Mechanism of Toxicity. *Nanoscale* **2011**, *3* (2), 410–420. https://doi.org/10.1039/c0nr00478b.

(65) Alkilany, A. M.; Murphy, C. J. Toxicity and Cellular Uptake of Gold Nanoparticles: What We Have Learned so Far? *J. Nanoparticle Res.* **2010**, *12* (7), 2313–2333. https://doi.org/10.1007/s11051-010-9911-8.

(66) Wu, Y.-C.; Wu, T.-H.; Clemens, D. L.; Lee, B.-Y.; Wen, X.; Horwitz, M. A.; Teitell, M. A.; Chiou, P.-Y. Massively Parallel Delivery of Large Cargo into Mammalian Cells with Light Pulses. *Nat Meth* **2015**, *12* (5), 439–444. https://doi.org/10.1038/nmeth.3357\nhttp://www.nature.com/nmeth/journal/v12/n5/abs/nmeth.3357.html#supplementary-information.

(67) Madrid, M.; Saklayen, N.; Shen, W.; Huber, M.; Vogel, N.; Mazur, E. Laser-Activated Self-Assembled Thermoplasmonic Nanocavity Substrates for Intracellular Delivery. *ACS Appl. Bio Mater.* **2018**, *1* (6), 1793–1799. https://doi.org/10.1021/acsabm.8b00447.

(68) Raun, A.; Saklayen, N.; Zgrabik, C.; Shen, W.; Madrid, M.; Huber, M.; Hu, E.; Mazur, E. A Comparison of Inverted and Upright Laser-Activated Titanium Nitride Micropyramids for Intracellular Delivery. *Sci. Rep.* **2018**, *8* (1), 15595. https://doi.org/10.1038/s41598-018-33885-y.

(69) Huang, J. A.; Caprettini, V.; Zhao, Y.; Melle, G.; MacCaferri, N.; Deleye, L.; Zambrana-Puyalto, X.; Ardini, M.; Tantussi, F.; Dipalo, M.; De Angelis, F. On-Demand Intracellular Delivery of Single Particles in Single Cells by 3D Hollow Nanoelectrodes. *Nano Lett.* **2019**, *19* (2), 722–731. https://doi.org/10.1021/acs.nanolett.8b03764.

(70) St-Louis Lalonde, B.; Boulais, E.; Lebrun, J.-J.; Meunier, M. Visible and near Infrared Resonance Plasmonic Enhanced Nanosecond Laser Optoporation of Cancer Cells. *Biomed. Opt. Express* **2013**, *4* (4), 490–499. https://doi.org/10.1364/BOE.4.000490.

(71) Lyu, Z.; Zhou, F.; Liu, Q.; Xue, H.; Yu, Q.; Chen, H. A Universal Platform for Macromolecular Deliveryinto Cells Using Gold Nanoparticle Layers via the Photoporation Effect. *Adv. Funct. Mater.* **2016**. https://doi.org/10.1002/adfm.201602036.

(72) Zhao, C.; Man, T.; Xu, X.; Yang, Q.; Liu, W.; Jonas, S. J.; Teitell, M. A.; Chiou, P. Y.; Weiss, P. S. Photothermal Intracellular Delivery Using Gold Nanodisk Arrays. *ACS Mater. Lett.* **2020**, *2* (11), 1475–1483. https://doi.org/10.1021/acsmaterialslett.0c00428.

(73) Vogel, N.; Goerres, S.; Landfester, K.; Weiss, C. K. A Convenient Method to Produce Close- and Non-Close-Packed Monolayers Using Direct Assembly at the Air-Water Interface and Subsequent Plasma-Induced Size Reduction. *Macromol. Chem. Phys.* **2011**, *212* (16), 1719–1734. https://doi.org/10.1002/macp.201100187.

(74) Kraus, T.; Brodoceanu, D.; Pazos-Perez, N.; Fery, A. Colloidal Surface Assemblies: Nanotechnology Meets Bioinspiration. *Adv. Funct. Mater.* **2013**, *23* (36), 4529–4541.

https://doi.org/10.1002/adfm.201203885.

(75) Stein, A.; Wilson, B. E.; Rudisill, S. G. Design and Functionality of Colloidal–Crystal–Templated Materials—Chemical Applications of Inverse Opals. *Chem. Soc. Rev.* **2013**, *42* (7), 2763–2803. https://doi.org/10.1039/c2cs35317b.

(76) Phillips, K. R.; England, G. T.; Sunny, S.; Shirman, E.; Shirman, T.; Vogel, N.; Aizenberg, J. A Colloidoscope of Colloid-Based Porous Materials and Their Uses. *Chem. Soc. Rev.* **2016**, *45* (2), 281–322. https://doi.org/10.1039/c5cs00533g.

(77) Vogel, N.; Weiss, C. K.; Landfester, K. From Soft to Hard: The Generation of Functional and Complex Colloidal Monolayers for Nanolithography. *Soft Matter* **2012**, *8* (15), 4044–4061. https://doi.org/10.1039/c1sm06650a.

(78) Nemiroski, A.; Gonidec, M.; Fox, J. M.; Jean-Remy, P.; Turnage, E.; Whitesides, G. M. Engineering Shadows to Fabricate Optical Metasurfaces. *ACS Nano* **2014**, *8* (11), 11061–11070. https://doi.org/10.1021/nn504214b.

(79) Ye, X.; Qi, L. Two-Dimensionally Patterned Nanostructures Based on Monolayer Colloidal Crystals: Controllable Fabrication, Assembly, and Applications. *Nano Today* **2011**, *6* (6), 608–631. https://doi.org/10.1016/j.nantod.2011.10.002.

(80) Nagpal, P.; Lindquist, N. C.; Oh, S. H.; Norris, D. J. Ultrasmooth Patterned Metals for Plasmonics and Metamaterials. *Science (80-.).* **2009**, *325* (5940), 594–597. https://doi.org/10.1126/science.1174655.

(81) Vogel, N.; Zieleniecki, J.; Köper, I. As Flat as It Gets: Ultrasmooth Surfaces from Template-Stripping Procedures. *Nanoscale* **2012**, *4* (13), 3820–3832. https://doi.org/10.1039/c2nr30434a.

(82) Lee, J.; Hasan, W.; Stender, C. L.; Odom, T. W. Pyramids: A Platform for Designing

Multifunctional Plasmonic Particles. *Acc. Chem. Res.* **2008**, *41* (12), 1762–1771. https://doi.org/10.1021/ar800126p.

(83) Sun, C. H.; Linn, N. C.; Jiang, P. Templated Fabrication of Periodic Metallic Nanopyramid Arrays. *Chem. Mater.* **2007**, *19* (18), 4551–4556. https://doi.org/10.1021/cm0712319.

(84) Bean, K. E. Anisotropic Etching of Silicon. *IEEE Trans. Electron Devices* **1978**, *25* (10), 1185–1193. https://doi.org/10.1109/9780470545263.sect1.

(85) Krauss, P. R.; Chou, S. Y. Nano-Compact Disks with 400 Gbit/In2 Storage Density Fabricated Using Nanoimprint Lithography and Read with Proximal Probe. *Appl. Phys. Lett.* **1997**, *71* (21), 3174–3176. https://doi.org/10.1063/1.120280.

(86) Lackner, J. M.; Waldhauser, W.; Berghauser, R.; Ebner, R.; Major, B.; Schöberl, T. Structural, Mechanical and Tribological Investigations of Pulsed Laser Deposited Titanium Nitride Coatings. *Thin Solid Films* **2004**, *453–454*, 195–202. https://doi.org/10.1016/j.tsf.2003.11.106.

(87) Gordon, R. G. Criteria for Choosing Transparent Conductors. *MRS Bull.* **2000**, *25* (8), 52–57. https://doi.org/10.1557/mrs2000.151.

(88) Guler, U.; Ndukaife, J. C.; Naik, G. V.; Nnanna, A. G. A.; Kildishev, A. V.; Shalaev, V. M.; Boltasseva, A. Local Heating with Lithographically Fabricated Plasmonic Titanium Nitride Nanoparticles. *Nano Lett.* **2013**, *13* (12), 6078–6083. https://doi.org/10.1021/nl4033457.

(89) Guler, U.; Zemlyanov, D.; Kim, J.; Wang, Z.; Chandrasekar, R.; Meng, X.; Stach, E.; Kildishev, A. V.; Shalaev, V. M.; Boltasseva, A. Plasmonic Titanium Nitride Nanostructures via Nitridation of Nanopatterned Titanium Dioxide. *Adv. Opt. Mater.* **2017**, *5* (7). https://doi.org/10.1002/adom.201600717.

(90) Starosvetsky, D.; Gotman, I. Corrosion Behavior of Titanium Nitride Coated Ni-Ti Shape Memory Surgical Alloy. *Biomaterials* **2001**, *22* (13), 1853–1859. https://doi.org/10.1016/S0142-9612(00)00368-9.

(91) Zgrabik, C. M.; Hu, E. L. Optimization of Sputtered Titanium Nitride as a Tunable Metal for Plasmonic Applications. *Opt. Mater. Express* **2015**, *5* (12), 2786. https://doi.org/10.1364/OME.5.002786.

(92) Fan, Z.; Liu, H.; Mayer, M.; Deng, C. X. Spatiotemporally Controlled Single Cell Sonoporation. *Proc. Natl. Acad. Sci. U. S. A.* **2012**, *109* (41), 16486–16491. https://doi.org/10.1073/pnas.1208198109.

(93) Hobbie, R.K. and Roth, B.J., 2007. *Intermediate physics for medicine and biology* (Vol. 463). New York: Springer. 95

(94) McNeil, P. L.; Terasaki, M. Coping with the Inevitable: How Cells Repair a Torn Surface Membrane. *Nat. Cell Biol.* **2001**, *3* (5), E124–E129. https://doi.org/10.1038/35074652.

(95) Antkowiak, M.; Torres-Mapa, M. L.; Stevenson, D. J.; Dholakia, K.; Gunn-Moore, F. J. Femtosecond Optical Transfection of Individual Mammalian Cells. *Nat. Protoc.* **2013**, *8* (6), 1216–1233. https://doi.org/10.1038/nprot.2013.071.

(96) Baffou, G.; Berto, P.; Berm??dez Ure??a, E.; Quidant, R.; Monneret, S.; Polleux, J.; Rigneault, H. Photoinduced Heating of Nanoparticle Arrays. *ACS Nano* **2013**, *7* (8), 6478–6488. https://doi.org/10.1021/nn401924n.

(97) Baffou, G.; Polleux, J.; Rigneault, H.; Monneret, S. Super-Heating and Micro-Bubble Generation around Plasmonic Nanoparticles under Cw Illumination. *J. Phys. Chem. C* **2014**, *118* (9), 4890–4898. https://doi.org/10.1021/jp411519k.

(98) Messina, G. C.; Dipalo, M.; La Rocca, R.; Zilio, P.; Caprettini, V.; Proietti Zaccaria, R.;

Toma, A.; Tantussi, F.; Berdondini, L.; De Angelis, F. Spatially, Temporally, and Quantitatively Controlled Delivery of Broad Range of Molecules into Selected Cells through Plasmonic Nanotubes. *Adv. Mater.* **2015**, No. OCTOBER, n/a-n/a. https://doi.org/10.1002/adma.201503252.

(99) Wu, Y.-C.; Wu, T.-H.; Clemens, D. L.; Lee, B.-Y.; Wen, X.; Horwitz, M. A.; Teitell, M. A.; Chiou, P.-Y. Massively Parallel Delivery of Large Cargo into Mammalian Cells with Light Pulses. *Nat Meth* **2015**, *12* (5), 439–444. https://doi.org/10.1038/nmeth.3357\nhttp://www.nature.com/nmeth/journal/v12/n5/abs/nmeth.3357.html#supplementary-information.

(100) Utech, S.; Bley, K.; Aizenberg, J.; Vogel, N. Tailoring Re-Entrant Geometry in Inverse Colloidal Monolayers to Control Surface Wettability. *J. Mater. Chem. A* **2016**, *4* (18), 6853–6859. https://doi.org/10.1039/c5ta08992a.

(101) Vogel, N.; Belisle, R. A.; Hatton, B.; Wong, T. S.; Aizenberg, J. Transparency and Damage Tolerance of Patternable Omniphobic Lubricated Surfaces Based on Inverse Colloidal Monolayers. *Nat. Commun.* **2013**, *4*, 1–10. https://doi.org/10.1038/ncomms3176.

(102) O'Mahony, A. M.; Godinho, B. M. D. C.; Cryan, J. F.; O'Driscoll, C. M. Non-Viral Nanosystems for Gene and Small Interfering RNA Delivery to the Central Nervous System: Formulating the Solution. *J. Pharm. Sci.* **2013**, *102* (10), 3469–3484. https://doi.org/10.1002/jps.23672.

(103) Shen, W.; Kalies, S.; Madrid, M.; Heisterkamp, A.; Mazur, E. Intracellular Cargo Delivery Induced by Irradiating Polymer Substrates with Nanosecond-Pulsed Lasers. *ACS Biomater. Sci. Eng.* **2021**. https://doi.org/10.1021/acsbiomaterials.1c00656.

(104) Marx, V. Cell Biology : Delivering Tough Cargo into Cells. *Nat. Publ. Gr.* **2016**, *13* (1),

37–40. https://doi.org/10.1038/nmeth.3693.

(105) Shegokar, R.; Shaal, L. A. L.; Mishra, P. R. SiRNA Delivery: Challenges and Role of Carrier Systems. *Pharmazie* **2011**, *66* (5), 313–318. https://doi.org/10.1691/ph.2011.0301.

(106) Wang, X.; Huang, X.; Fang, X.; Zhang, Y.; Wang, W. CRISPR-Cas9 System as a Versatile Tool for Genome Engineering in Human Cells. *Mol. Ther. - Nucleic Acids* **2016**, *5* (September), e388. https://doi.org/10.1038/mtna.2016.95.

(107) Somia, N.; Verma, I. M. Gene Therapy: Trials and Tribulations. *Nat. Rev. Genet.* **2000**, *1* (November).

(108) Steinberger, P.; Andris-Widhopf, J.; Bühler, B.; Torbett, B. E.; Barbas, C. F. Functional Deletion of the CCR5 Receptor by Intracellular Immunization Produces Cells That Are Refractory to CCR5-Dependent HIV-1 Infection and Cell Fusion. *Proc. Natl. Acad. Sci. U. S. A.* **2000**, *97* (2), 805–810. https://doi.org/10.1073/pnas.97.2.805.

(109) Xu, L.; Yang, H.; Gao, Y.; Chen, Z.; Xie, L.; Liu, Y.; Liu, Y.; Wang, X.; Li, H.; Lai, W.; He, Y.; Yao, A.; Ma, L.; Shao, Y.; Zhang, B.; Wang, C.; Chen, H.; Deng, H. CRISPR/Cas9-Mediated CCR5 Ablation in Human Hematopoietic Stem/Progenitor Cells Confers HIV-1 Resistance In Vivo. *Mol. Ther.* **2017**, *25* (8), 1782–1789. https://doi.org/10.1016/j.ymthe.2017.04.027.

(110) Tirlapur, U. K.; König, K. Cell Biology: Targeted Transfection by Femtosecond Laser. *Nature* **2002**, *418* (6895), 290–291. https://doi.org/10.1038/418290a.

(111) Soman, P.; Zhang, W.; Umeda, A.; Zhang, Z. J.; Chen, S. Femtosecond Laser-Assisted Optoporation for Drug and Gene Delivery into Single Mammalian Cells. *J. Biomed. Nanotechnol.* **2011**, *7* (3), 334–341. https://doi.org/10.1166/jbn.2011.1295.

(112) Cottle, R. N.; Lee, C. M.; Archer, D.; Bao, G. Controlled Delivery of β -Globin- Targeting

TALENs and CRISPR / Cas9 into Mammalian Cells for Genome Editing Using Microinjection. *Nat. Publ. Gr.* **2015**, No. October, 1–13. https://doi.org/10.1038/srep16031.

(113) Kim, J.; Hwang, I.; Britain, D.; Chung, T. D.; Sun, Y.; Kim, D.-H. Microfluidic Approaches for Gene Delivery and Gene Therapy. *Lab Chip* **2011**, *11* (23), 3941. https://doi.org/10.1039/c1lc20766k.

(114) Remi Lachaine, Etienne Boulais, M. M. From Thermo- to Plasma-Mediated Ultrafast Laser-Induced Plasmonic Nanobubbles. *ACS Photonics* **2013**, *1* (4), 331–336. https://doi.org/https://doi.org/10.1021/ph400018s.

(115) Madrid, M.; Saklayen, N.; Shen, W.; Huber, M.; Vogel, N.; Mazur, E. Supporting Information Laser-Activated Self-Assembled Thermoplasmonic Nanocavity Substrates for Intracellular Delivery. *ACS Appl. Bio Mater.* **2018**, acsabm.8b00447. https://doi.org/10.1021/acsabm.8b00447.

(116) Pustovalov, V. K.; Smetannikov, A. S.; Zharov, V. P. Photothermal and Accompanied Phenomena of Selective Nanophotothermolysis with Gold Nanoparticles and Laser Pulses. *Laser Phys. Lett.* **2008**, *5* (11), 775–792. https://doi.org/10.1002/lapl.200810072.

(117) Harizaj, A.; Wels, M.; Raes, L.; Stremersch, S.; Goetgeluk, G.; Brans, T.; Vandekerckhove, B.; Sauvage, F.; De Smedt, S. C.; Lentacker, I.; Braeckmans, K. Photoporation with Biodegradable Polydopamine Nanosensitizers Enables Safe and Efficient Delivery of MRNA in Human T Cells. *Adv. Funct. Mater.* **2021**, *2102472*, 18–21. https://doi.org/10.1002/adfm.202102472.

(118) Strangman, G.; Boas, D. A.; Sutton, J. P. Non-Invasive Neuroimaging Using near-Infrared Light. *Biol. Psychiatry* **2002**, *52* (7), 679–693. https://doi.org/10.1016/S0006-3223(02)01550-0.

(119) Pritchard, G. *Plastics Additives: An A-Z Reference*; Springer Netherlands, 1998; Vol. 53.

(120) Wu, J.; Zheng, Y.; Jiang, S.; Qu, Y.; Wei, T.; Zhan, W.; Wang, L.; Yu, Q.; Chen, H. Two-in-One Platform for High-Efficiency Intracellular Delivery and Cell Harvest: When a Photothermal Agent Meets a Thermoresponsive Polymer. *ACS Appl. Mater. Interfaces* **2019**, *11* (13), 12357–12366. https://doi.org/10.1021/acsami.9b01586.

(121) Wang, J.; Ren, K. F.; Gao, Y. F.; Zhang, H.; Huang, W. P.; Qian, H. L.; Xu, Z. K.; Ji, J. Photothermal Spongy Film for Enhanced Surface-Mediated Transfection to Primary Cells. *ACS Appl. Bio Mater.* **2019**, *2* (6), 2676–2684. https://doi.org/10.1021/acsabm.9b00358.

(122) Patrick, S. *Practical Guide to Polyvinyl Chloride*; iSmithers Rapra Publishing, 2005.

(123) Mendes, R. G.; Bachmatiuk, A.; Buechner, B.; Cuniberti, G.; Rümmeli, M. Carbon Nanostructures as Multi-Functional Drug Delivery Platforms. *J. Mater. Chem. B* **2013**, 401–428. https://doi.org/10.1039/c2tb00085g.

(124) Hou, Y.; Kim, J. S.; Ashkenazi, S.; O'Donnell, M.; Guo, L. J. Optical Generation of High Frequency Ultrasound Using Two-Dimensional Gold Nanostructure. *Appl. Phys. Lett.* **2006**, *89* (9). https://doi.org/10.1063/1.2344929.

(125) Galla, L.; Greif, D.; Regtmeier, J.; Anselmetti, D. Microfluidic Carbon-Blackened Polydimethylsiloxane Device with Reduced Ultra Violet Background Fluorescence for Simultaneous Two-Color Ultra Violet / Visible-Laser Induced Fluorescence Detection in Single Cell Analysis. **2012**, *014104*, 1–10. https://doi.org/10.1063/1.3675608.

(126) Park, S.; Choi, S. O.; Paik, S. joon; Choi, S.; Allen, M.; Prausnitz, M. Intracellular Delivery of Molecules Using Microfabricated Nanoneedle Arrays. *Biomed. Microdevices* **2016**, *18* (1), 10. https://doi.org/10.1007/s10544-016-0038-2.

(127) Wolf, M. P.; Salieb-Beugelaar, G. B.; Hunziker, P. PDMS with Designer Functionalities—

Properties, Modifications Strategies, and Applications. *Prog. Polym. Sci.* **2018**, *83* (August), 97–134. https://doi.org/10.1016/j.progpolymsci.2018.06.001.

(128) Adamo, A.; Sharei, A.; Adamo, L.; Lee, B.; Mao, S.; Jensen, K. F. Microfluidics-Based Assessment of Cell Deformability. *Anal. Chem.* **2012**, *84* (15), 6438–6443. https://doi.org/10.1021/ac300264v.

(129) Saung, M. T.; Sharei, A.; Adalsteinsson, V. A.; Nahyun, C.; Tushar, K.; Camilo, R.; Kirkpatrick, J.; Patel, N.; Mino-Kenudson, M.; Thayer, S. P.; Langer, R.; Jensen, K. F.; Liss, A. S.; Love, J. C. A Size-Selective Intracellular Delivery Platform. *Small* **2016**, *12* (42), 5873–5881. https://doi.org/10.1002/smll.201601155.A.

(130) Szeto, G. L.; Van Egeren, D.; Worku, H.; Sharei, A.; Alejandro, B.; Park, C.; Frew, K.; Brefo, M.; Mao, S.; Heimann, M.; Langer, R.; Jensen, K.; Irvine, D. J. Microfluidic Squeezing for Intracellular Antigen Loading in Polyclonal B-Cells as Cellular Vaccines. *Sci. Rep.* **2015**, *5* (April), 1–13. https://doi.org/10.1038/srep10276.

(131) Qin, D.; Xia, Y.; Whitesides, G. M. Soft Lithography for Micro- and Nanoscale Patterning. *Nat. Protoc.* **2010**, *5* (3), 491–502. https://doi.org/10.1038/nprot.2009.234.

(132) Abate, A. R.; Lee, D.; Do, T.; Holtze, C.; Weitz, D. A. Glass Coating for PDMS Microfluidic Channels by Sol-Gel Methods. *Lab Chip* **2008**, *8* (4), 516–518. https://doi.org/10.1039/b800001h.

(133) Villa-Diaz, L. G.; Nandivada, H.; Ding, J.; Nogueira-De-Souza, N. C.; Krebsbach, P. H.; O'Shea, K. S.; Lahann, J.; Smith, G. D. Synthetic Polymer Coatings for Long-Term Growth of Human Embryonic Stem Cells. *Nat. Biotechnol.* **2010**, *28* (6), 581–583. https://doi.org/10.1038/nbt.1631.

(134) Brennen, C.E., 2014. *Cavitation and bubble dynamics*. Cambridge university press.

(135) Arrio-Dupont, M.; Cribier, S.; Foucault, G.; Devaux, P. F.; D'Albis, A. Diffusion of Fluorescently Labeled Macromolecules in Cultured Muscle Cells. *Biophys. J.* **1996**, *70* (5), 2327–2332. https://doi.org/10.1016/S0006-3495(96)79798-9.

(136) Kumar, S.; Li, A.; Thadhani, N. N.; Prausnitz, M. R. Optimization of Intracellular Macromolecule Delivery by Nanoparticle-Mediated Photoporation. *Nanomedicine Nanotechnology, Biol. Med.* **2021**, *37*, 102431. https://doi.org/10.1016/j.nano.2021.102431.

(137) Devi, G. R. SiRNA-Based Approaches in Cancer Therapy. *Cancer Gene Ther.* **2006**, *13* (9), 819–829. https://doi.org/10.1038/sj.cgt.7700931.

(138) Hu, B.; Zhong, L.; Weng, Y.; Peng, L.; Huang, Y.; Zhao, Y.; Liang, X. J. Therapeutic SiRNA: State of the Art. *Signal Transduct. Target. Ther.* **2020**, *5* (1). https://doi.org/10.1038/s41392-020-0207-x.

(139) Dana, H.; Chalbatani, G. M.; Mahmoodzadeh, H.; Karimloo, R.; Rezaiean, O.; Moradzadeh, A.; Mehmandoost, N.; Moazzen, F.; Mazraeh, A.; Marmari, V.; Ebrahimi, M.; Rashno, M. M.; Abadi, S. J.; Gharagouzlo, E. Molecular Mechanisms and Biological Functions of SiRNA. *Int. J. Biomed. Sci.* **2017**, *13* (2), 48–57.

(140) Pei, Y.; Hancock, P. J.; Zhang, H.; Bartz, R.; Cherrin, C.; Innocent, N.; Pomerantz, C. J.; Seitzer, J.; Koser, M. L.; Abrams, M. T.; Xu, Y.; Kuklin, N. A.; Burke, P. A.; Sachs, A. B.; Sepp-Lorenzino, L.; Barnett, S. F. Quantitative Evaluation of SiRNA Delivery in Vivo. *Rna* **2010**, *16* (12), 2553–2563. https://doi.org/10.1261/rna.2255810.

(141) Xu, C. fei; Wang, J. Delivery Systems for SiRNA Drug Development in Cancer Therapy. *Asian J. Pharm. Sci.* **2015**, *10* (1), 1–12. https://doi.org/10.1016/j.ajps.2014.08.011.

(142) Di, J.; Kim, J.; Hu, Q.; Jiang, X.; Gu, Z. Spatiotemporal Drug Delivery Using Laser-Generated-Focused Ultrasound System. *J. Control Release* **2015**, *220* (Pt B), 592–599.

https://doi.org/doi:10.1016/j.jconrel.2015.08.033.

(143) Han, W.; Wang, Y.; Zheng, Y. In Vivo Biocompatibility Studies of Nano TiO2materials. *Adv. Mater. Res.* **2009**, *79–82*, 389–392. https://doi.org/10.4028/www.scientific.net/AMR79-82.389.

(144) Escalante, L. E.; Gasch, A. P. The Role of Stress-Activated RNA-Protein Granules in Surviving Adversity. *Rna* **2021**, *27* (7), 753–762. https://doi.org/10.1261/rna.078738.121.